On the effect of the Sun's gravity around the Earth-Moon L_1 and L_2 libration points

José J. Rosales de Cáceres

UNIVERSITAT DE BARCELONA

On the effect of the Sun's gravity around the Earth-Moon L_1 and L_2 libration points

José J. Rosales de Cáceres

Ph.D. Advisor: Àngel Jorba Monte

Universitat de Barcelona
Programa de Doctorat en Matemàtiques i Informàtica

ON THE EFFECT OF THE SUN'S GRAVITY AROUND THE EARTH-MOON L_1 AND L_2 LIBRATION POINTS

Tesi presentada per en José J. Rosales de Cáceres per optar al grau de
Doctor en Matemàtiques i Informàtica

Director: Àngel Jorba Monte
Departament de Matemàtiques i Informàtica
Facultat de Matemàtiques i Informàtica
Juny de 2020

Certifico que la següent tesi
ha estat realitzada per en
José J. Rosales de Cáceres
sota la meva direcció.

Barcelona, juny de 2020

Àngel Jorba Monte

Contents

List of Figures

List of Tables

Acknowledgments

Fer un doctorat a distància i com a estudiant a temps parcial pot no ser una tasca fàcil. Deixant de banda les dificultat estrictament tècniques, hi ha unes dificultats d'un àmbit més personal. Són les dificultats que se'n deriven de la sensació d'estar sol corrent una carrera de fons. No tenir contacte diari i espontani amb altres estudiants i professors, xerrades de passadís per intercanviar idees, o atendre a seminaris fa que l'experiència pugui ser una mica solitària. En qualsevol cas, he estat molt afortunat de tenir gent al meu costat que m'ha acompanyat durant aquest camí. A aquestes persones van dedicades aquestes línies.

Primer de tot vull agrair a l'Àngel haver-me acceptat com a estudiant, tot i les dificultats d'estar lluny i en una altra franja horària. Ha estat un privilegi poder aprendre d'ell. Les teleconferències a les 6:30am (hora meva) per discutir, intercanviar idees, i parlar dels resultats eren una forma fantàstica de començar el dia, i de les coses que més he disfrutat. Moltes gràcies Àngel per tot el que m'has ensenyat.

En Marc Jorba-Cuscó també mereix unes línes destacades. Marc és el més proper que he tingut a un company de doctorat durant aquests anys. Ell ha estat gairebé des del principi, quan els dos ens estàvem barallant amb les formes normals. Marc, no només et dec el codi de l'aritmètica de Fourier utilizat en aquest tesi, sinó també idees i bones conversacions. Moltes gràcies per tot!

També una menció a l'Ari, que ha estat de les poques persones amb les que podia parlar de mates cara a cara. Gràcies pels dinars la cafeteria de l'edifici 21 al GSFC.

En l'ambit estrictament acadèmic vull donar les gràcies també a en Josep Masdemont. Va ser ell qui fa més de quinze anys va introduir-me a l'Astrodinàmica i la seva aproximació des del punt vista dels sistemes dinàmics. Va ser una col·laboració curta, però que em va influenciar molt. Aquesta tesi n'és un testimoni.

También quiero dar las gracias a mi madre y a mi padre. A ellos les debo el interés por aprender y la curiosidad. Siempre me animaron a hacer el doctorardo, y su ejemplo ha sido siempre una referencia para mí.

Finalmente, muchas gracias a Majo. Ella es la persona con la que comparto mi vida y la que realmente ha vivido, sufrido y disfrutado el día a día de todo lo que este trabajo representa. Sin ella este camino habría sido mucho más largo, incómodo y desapacible. Muchas gracias por tu apoyo y paciencia. Majo, esta tesis también es tuya.

Washington, DC, 2020

A Majo y a nuestro hijo Yago.

Chapter 1

Introduction

1.1 Statement of the problem

The Restricted Three Body Problem (RTBP) is a model that describes the dynamics of a massless particle under the influence of two massive bodies called the primaries. It is assumed that the two primaries orbit in circular motion around their common barycenter following the Newton's Law, and that the third body does not influence the motion of the other two bodies.

To study this model, it is convenient to chose a rotating frame, with an angular rate equal to the orbital angular rate of the primaries, and scale the time such that one period equals to 2π. This way, the two primaries lay on the x-axis and are fixed points. Also, it is convenient to chose the unit of distance equal to the constant distance between the two primaries. Finally, the unit of mass is chosen such that the sum of the masses of the two primaries is equal to one. With this scaling in the units of distance and mass, the (fixed) position of a primary is μ (resp. $\mu - 1$) and its mass $1 - \mu$ (resp. μ). Hence, the model is fully characterized by the parameter μ. Some approximate typical parameters for different systems are listed in Table 1.1[1]. In this dissertation we are interested in the Earth-Moon system, and this will be the focus of our attention from now on.

Table 1.1: Some μ parameters from different systems

System	μ value
Sun-Earth	`3.04042339E-6`
Sun-Jupiter	`9.54791915E-4`
Earth-Moon	`1.21505816E-2`

Note that this reference frame, often referred to as a *synodic* reference frame, is not inertial. Details on the construction of the model can be found in [Szebehely, 1967].

---

[1] Note that these value may vary slightly depending on the source used to get the masses of the primaries.

In the synodic frame, the RTBP equations of motion are:

$$\begin{cases} \ddot{X} = 2\dot{Y} + X - \dfrac{1-\mu}{R_{PE}^3}(X-\mu) - \dfrac{\mu}{R_{PM}^3}(X-\mu+1) \\ \\ \ddot{Y} = -2\dot{X} + Y - \dfrac{1-\mu}{R_{PE}^3}Y - \dfrac{\mu}{R_{PM}^3}Y \\ \\ \ddot{Z} = -\dfrac{1-\mu}{R_{PE}^3}Z - \dfrac{\mu}{R_{PM}^3}Z \end{cases} \tag{1.1}$$

where:

- $R_{PE}^2 = (X-\mu)^2 + Y^2 + Z^2$ is the distance of the massless particle P to the Earth
- $R_{PM}^2 = (X-\mu+1)^2 + Y^2 + Z^2$ is the distance of P to the Moon

Defining the momenta $P_X = \dot{X} - Y$, $P_Y = \dot{Y} + X$ and $P_Z = \dot{Z}$, the dynamics of the RTBP can be expressed in the Hamiltonian formalism as follow:

$$H_{RTBP} = \frac{1}{2}(P_X^2 + P_Y^2 + P_Z^2) + YP_X - XP_Y - \frac{1-\mu}{R_{PE}} - \frac{\mu}{R_{PM}} \tag{1.2}$$

In the synodic reference frame, it is well know that the RTBP has five equilibrium points (three collinear and two forming an equilateral triangle, known as triangular or equilateral, with respect to the primaries) referred as Lagrange points or libration points. These are labeled $L_i, i = 1, \dots, 5$ in the scientific literature, where L_1, L_2 and L_3 are the collinear points, and L_4 and L_5 the equilateral ones.

It is around these points where the dynamic is interesting, and where most of the literature focuses its attention. The three collinear points are known to be unstable for all values of $\mu \leq 0.5$, with stability type saddle × center × center. On the other hand, the triangular points are stable for values of $\mu < \frac{1}{2}(1 - \sqrt{\frac{23}{27}}) \approx 0.0385$ (know as the critical Routh mass). In particular, the systems of interest for space missions have a value of μ below the critical Routh mass (See Table 1.1).

Around the collinear points it is also known that two one-parametric families of periodic orbits emerge from the centers: one family is planar, meaning that the orbits lay on the plane defined by the motion of the primaries; and the second family has a vertical component. These families are known as the planar and vertical Lyapunov families respectively, and can be parametrized by the energy of the system (this is, by setting $H_{RTBP} = h_0$). When varying the energy, there is a point where the family of the planar Lyapunov undergoes a pitchfork bifurcation that gives rise to the well-known family of Halo periodic orbits. Around these Halo orbits there are families of quasi-periodic orbits, know as quasi-Halos. On the other hand, around the vertical Lyapunov there are also families of quasi-periodic orbits, known as Lissajous orbits.

The qualitative behavior around the collinear libration points described in the previous paragraph has been studied in the scientific literature. In [Jorba and Masdemont, 1999], the authors study the dynamics around the collinear Lagrange points in the RTBP. One of the results of this reference is a qualitative description of the bounded motions around the Earth-Moon L_2 Lagrange point, and the Sun-Earth L_1 point. These results were expanded in [Gómez and Mondelo, 2001], and it provides a comprehensive description of the dynamics around all the collinear points in the Earth-Moon system. In this line, the reference [Gómez et al., 2003] provides a good summary of both papers along with additional results.

Note that, in the context of the Earth-Moon system, the previous results did not account for other effects such as the eccentricity of the Moon or the gravitational influence of the Sun. None of these effects are negligible. In particular, the mass of the Sun is approximately 329,000 times the mass of the Earth and the Moon combined. Hence, the gravitational effect that the Sun has on a particle orbiting in the Earth-Moon system is expected to have some impact on its dynamics. The study of the Sun's gravitational effect on the dynamics around the Earth-Moon L_1 and L_2 libration points is the fundamental question we are addressing in the present work. The selection of these two points is not arbitrary: they are candidates to host space assets for scientific missions. As an example, the most illustrative use case at the time of writing this work is the Lunar Gateway, a permanent station orbiting in a Near Rectilinear Halo Orbit (NRHO) (see [Zimovan et al., 2017]).

The first step to address this problem is to model the gravitational effect of the Sun. From a mathematical point of view, we are interested in studying models that describe the dynamics of a massless point under the gravitational influence of three point masses orbiting around each other. We refer to this configuration as a Restricted Four Body Problem (RFBP). In our case, each one of these masses represent the Sun, the Earth, and the Moon, but other scenarios considering other celestial bodies have also been studied. For example, in [Gabern, 2003] several restricted four body problems using the Sun, Jupiter and Saturn as point masses are used to study the dynamics of the Trojan asteroids.

We focus our attention on two RFBP models that approximate the dynamics of the Sun, the Earth, the Moon, and a massless body: the Bicircular Problem (BCP), and the Quasi-Bicircular Problem (QBCP). These two models are not new, and early references can be found in [Huang, 1960] and [Andreu, 1998] respectively. These two models can be expressed mathematically as periodic time-dependent perturbations of the RTBP, depending on one frequency. This is relevant because the RTBP gives us a solid reference we can use as starting point for our studies. Finally, a remarkable fact is that these two models can be formulated as a periodic time-dependent Hamiltonian. Note that there are other models that describe the motion of a massless particle in the Sun-Earth-Moon system. For example, the Hill Restricted Four Body Problem, introduced by [Scheeres, 1998].

The BCP and the QBCP both model the same system, and there is only one fundamental difference between them: how the motion of the three primaries is modeled. In the BCP, the Earth and the Moon follow a circular orbit around their barycenter and, in the same fashion, the Sun and the Earth-Moon barycenter also are in a circular orbit. All three bodies are coplanar. Note that this model is not coherent in the sense that it does not comply with Newton's Laws. On the other hand, in the QBCP the three primaries are also coplanar, but their motion is a periodic orbit solution of a three-body problem.

In the these two models, the libration points $L_i, i = 1, ..., 5$ we find in the RTBP are not equilibrium points anymore due to their non-autonomous character. However, as a direct application of the Implicit Function Theorem, it is known that if an autonomous differential equation with equilibrium points is perturbed with a small periodic time-dependent perturbation, then under generic non-resonant conditions the equilibrium points become periodic orbits around the point (now defined only geometrically) with the same period of the perturbation. Hence, in our scenario, both in the BCP and in the QBCP there are periodic orbits around the (geometrically defined) libration points with the same period of the Sun.

It is at this point where it is relevant to answer a natural question: why do we choose two models, the BCP and the QBCP, to study the dynamics of the Sun-Earth-Moon system? The main reason is that, although they both model the same system, they behave very differently around the L_2 libration point. The differences are documented in [Andreu, 1998, Jorba-Cuscó et al., 2018]. Hence, it is interesting to study both models around L_2 to try to understand their fundamental differences.

The second step to tackle our problem is to establish a framework to study these models. In this work, the problem is formulated in the framework of dynamical systems. This is, we are interested in describing the phase space around the Earth-Moon L_1 and L_2 regions. There is a good understanding in the scientific literature of the phase space around these two points in the RTBP, and we use this model as a reference. Hence, we attempt to understand how the phase space around the Earth-Moon L_1 and L_2 points is affected by the Sun's gravity. This effort includes identifying what type of invariants objects exist in a neighborhood of the Earth-Moon L_1 and L_2 points, as well as their stability and, if they exist, their associated invariant manifolds. These objects shape the *skeleton* of the phase space, in the sense that they organize the dynamics in the region of interest. The relevance of finding these objects goes beyond the academic realm, and there are potential practical applications. For example, for mission analysis to libration points the reference model is the RTBP. Hence, to chose candidate orbits for missions we are limited to the objects that exist there (Halos, quasi-halos, Lissajous, etc...). When considering a Sun-Earth-Moon RFBP, we are adding an extra effect (the gravity of the Sun), and it is possible that new object suitable for scientific mission appear. Moreover, not only new objects may appear, but also new connections between, for example, the Earth and candidates orbits to host space assets.

The third step is to define the tools to study these models, and specifically the regions of interest defined by a neighborhood of the L_1 and L_2 points. In this research we use numerical methods that can help us to extract information about the models, and visualize it. This data is then interpreted to generate an understanding of what type of motions exists around the collinear points L_1 and L_2. We use essentially three families of methods: reduction to the center manifold, computation of invariant tori and their stability, and the computation of invariant manifolds. Chapter 2 is devoted to the description of these methods, but for completeness a high-level overview is provide here.

The reduction to the center manifold is a normal form that decouples the unstable components of system from the central ones. The result of this reduction is a Hamiltonian H_{CM} that captures the bounded motion, and it is expressed as a a trucated series $H_{CM} = H_2 + H_3 + ... + H_N$, where $H_k, k = 1, ..., N$ are homogeneous polynomials of degree k. Hence, the results are only valid on a the domain of convergence of the series. This technique has been extensively used to qualitatively describe the dynamics around equilibrium points. In the RTBP case, [Jorba and Masdemont, 1999] use this method to illustrate the type of objects around the L_1 and L_2 points in Sun-Earth system, and in Earth-Moon system. For a non-autonomous systems like the QBCP, [Andreu, 1998] is a representative example of how the reduction to the center manifold around an invariant object helps to understand the qualitative behavior of the dynamics.

The continuation of invariant tori allows to get an insight on how these objects are organized in the phase space, and to explore connections among them. Examples of previous successful implementations of this approach can be found in [Castellà, 2003], where the dynamics around the L_5 in the BCP by continuation of families of invariant tori is characterized. In addition to computing these objects, we are also interested computing in their stability ([Jorba, 2001]), and unstable and stable manifolds ([Simó, 1990]). These two elements are essential to understand the phase space, but also are good criteria to establish their usefulness for practical applications. For example, the stable manifold can be used to transfer and control a spacecraft from a parking orbit around the Earth to a libration point orbit (see [Gómez et al., 1985]). Again, these techniques for transfer and control have been mainly studied in the context of the RTBP. In this work, we are interested in exploring the effect that the Sun's gravity has on these invariant manifolds for the transfer problem.

1.2 Mathematical models and state of the art

In this sections we present the mathematical models used in this dissertation: the BCP, and the QBCP. Both models are presented in the Hamiltonian formalism, and a summary of known results related to the qualitative behavior of the dynamics around the five libration points is presented.

1.2.1 The Bicircular Problem

The Earth-Moon BCP is a RFBP that describes the motion of a massless particle (P) under the influence of the Earth (E), the Moon (M), and the Sun (S). The Earth and the Moon are defined as the primaries. The dynamics of the Earth, Moon and Sun are simplified considering that the three bodies orbit in the same plane. Also, it is considered that the Earth and the Moon follow a circular orbit around their barycenter (B), and that B is orbiting around the S-E/M barycenter. Note that this model is not coherent, in the sense that the motion of the three massive bodies is not described by the Newton's equations.

Using synodic coordinates with respect to the Earth-Moon center, with the origin centered

Table 1.2: Parameters of the BCP.

$\mu = 0.012150581623433$	$m_s = 328900.5499999991$
$\omega_s = 0.925195985518289$	$a_s = 388.8111430233511$

at their respective center of mass, the equations of motion of the BCP are

$$\begin{cases} \ddot{X} = 2\dot{Y} + X - \dfrac{1-\mu}{R_{PE}^3}(X-\mu) - \dfrac{\mu}{R_{PM}^3}(X-\mu+1) - \dfrac{m_S}{R_{PS}^3}(X - X_S) - \dfrac{m_S}{a_S^2}\cos\vartheta \\ \\ \ddot{Y} = -2\dot{X} + Y - \dfrac{1-\mu}{R_{PE}^3}Y - \dfrac{\mu}{R_{PM}^3}Y - \dfrac{m_S}{R_{PS}^3}(Y - Y_S) + \dfrac{m_S}{a_S^2}\sin\vartheta \\ \\ \ddot{Z} = -\dfrac{1-\mu}{R_{PE}^3}Z - \dfrac{\mu}{R_{PM}^3}Z - \dfrac{m_S}{R_{PS}^3}Z \end{cases} \tag{1.3}$$

with units of mass, length and time such that the sum of masses the primaries (Earth and Moon), the gravitational constant, and the period of motion of the primaries are 1, 1 and 2π respectively, and:

- The parameter μ (resp. $1-\mu$) is the normalized mass of the Moon (resp. Earth) and it is located at $(\mu-1, 0, 0)$ (resp. $(\mu, 0, 0)$)
- The parameters m_S and a_S are the mass of the Sun and its distance to the Earth-Moon barycenter respectively
- The frequency of the Sun around the Earth-Moon barycenter is ω_S and $\vartheta = \omega_S t$
- $X_S = a_S \cos\vartheta$ is the first component of the Sun position vector
- $Y_S = -a_S \sin\vartheta$ is the second component of the Sun position vector
- $R_{PE}^2 = (X-\mu)^2 + Y^2 + Z^2$ is the distance of the massless particle P to the Earth
- $R_{PM}^2 = (X-\mu+1)^2 + Y^2 + Z^2$ is the distance of P to the Moon
- $R_{PS}^2 = (X-X_S)^2 + (Y-Y_S)^2 + Z^2$ is the distance of P to the Sun

For this thesis, we have the values captured in Table 1.2.

Note that in this reference system the Sun moves around the origin in a circular motion (see Figure 1.1). A derivation of these equations of motion can be found in [Gómez et al., 1993a]. Earlier formulations of the BCP can be found in [Huang, 1960, Cronin et al., 1964].

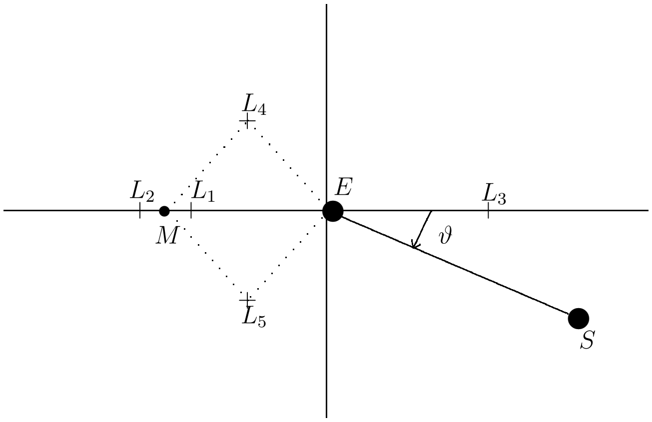

Figure 1.1: Sketch of the Bicircular problem. The points $L_i, i = 1, ..., 5$ are the Lagrangian points of the Earth-Moon RTBP.

Defining the momenta $P_X = \dot{X} - Y$, $P_Y = \dot{Y} + X$ and $P_Z = \dot{Z}$, the dynamics of the BCP can be expressed in the Hamiltonian formalism as follow:

$$\begin{aligned} H_{BCP} = \frac{1}{2}(P_X^2 + P_Y^2 + P_Z^2) + YP_X - XP_Y - \frac{1-\mu}{R_{PE}} - \frac{\mu}{R_{PM}} \\ -\frac{m_S}{R_{PS}} - \frac{m_S}{a_S^2}(Y \sin\vartheta - X\cos\vartheta) \end{aligned} \tag{1.4}$$

The Hamiltonian (1.4) can be expressed as a time-dependent perturbation of the RTBP:

$$H_{BCP} = H_{RTBP} + H_S \tag{1.5}$$

where:

$$H_{RTBP} = \frac{1}{2}(P_X^2 + P_Y^2 + P_Z^2) + YP_X - XP_Y - \frac{1-\mu}{R_{PE}} - \frac{\mu}{R_{PM}} \tag{1.6}$$

is the Hamiltonian of the RTBP, and

$$H_S = -\frac{m_S}{R_{PS}} - \frac{m_S}{a_S^2}(Y \sin\vartheta - X\cos\vartheta) \tag{1.7}$$

is the perturbation due to the Sun.

Let us define

$$H^\varepsilon = H_{RTBP} + \varepsilon H_S \tag{1.8}$$

Note that for $\varepsilon = 0$, $H^0 = H_{RTBP}$, and for $\varepsilon = 1$, $H^1 = H_{BCP}$. Considering $\varepsilon = 0$, the Lagrange points ($L_i, i = 1, ..., 5$) are equilibrium points of the system (1.8). When $\varepsilon > 0$ and small enough, the equilibrium point becomes a periodic orbit around the point (now defined only geometrically) with the same period of the perturbation (in this case, $T_S = 2\pi/\omega_S$).

As mentioned before, the BCP is not a new model, and has been studied both form a theoretical point of view, as well as a model for mission design analyses. The following paragraphs focus on known results that contribute to the understanding of the dynamic around the five equilibrium points of the RTBP in the Earth-Moon BCP.

Starting with the triangular points, in [Gómez et al., 1987] the authors show that in the BCP each triangular point is substituted by three periodic orbits. Two of these orbits have large amplitude and are linearly stable, and the third one is small and mildly unstable. These three periodic orbits are obtained by continuation with the respect to the mass of the Sun, and they have a period equal to the period of the perturbation (this is, the period of the Sun, T_S). The relevance of this result is that is shows that, contrary to the Earth-Moon RTBP, there are regions of instability due to the presence of this unstable periodic orbit.

Expanding on these results, in [Simó et al., 1995] the authors study the stability properties near the L_4 and L_5 equilateral points. In that work, the goal is to understand the kind of motions that appear in the neighborhood of the (geometrically defined) triangular points. By means of integrating a grid of initial conditions near the L_5 point for a long period of time (10000 lunar periods), the authors identified stability zones. These stability zones are outside the plane of motion of the three primaries. In order to further understand the transition from unstable to stable motion found in the numerical simulations, the authors study a normal form around the small and unstable orbit around L_5, and also compute 2D and 3D vertical tori using the Lindstedt-Poincaré method. This method, due its local character did not allow to continue the families of vertical tori in an extended neighborhood of the periodic orbits.

In the same context, [Castellà, 2003] in his Ph.D. dissertation expanded the results obtained in [Simó et al., 1995] and continued families of invariant tori, both vertical and horizontal. By continuing the vertical families, the author showed that two of these families, the one born from the unstable orbit, and one of the stable orbits are connected. These results helped to explain the stability transition observed in [Simó et al., 1995] and to provide a more complete picture of the dynamics around the equilateral points. These results can also be found in [Castellà and Jorba, 2000].

For the L_3 points, there are known results for the planar BCP. These are documented in [Jorba and Nicolás, 2020], and focus on the role L_3 plays in organizing the transport of particles going from Earth to the Moon (and vice-versa), and entering or leaving the Earth-Moon system. By means of computing the family of horizontal 2D invariant tori around L_3 and their associated invariant manifolds, the authors show connections between the Earth and the Moon. The relevance of this work is that these connections do not exist in the RTBP, and that it is due to the effect of the Sun as modeled in the BCP what creates them. In Chapter 5 of the present thesis, a similar analysis has been done to study transfers from a parking orbit around the Earth to a Halo orbit around L_2.

For L_2 very little is known in the BCP, and the main result is that there is no natural dynamical substitute of the L_2 point (see [Andreu, 2002]). Chapter 3 of the present dissertation focuses its attention to the L_2 region in the BCP, and provides an insight on some of the elements that shape the phase state.

Finally, for L_1 the main result is documented in [Jorba et al., 2020]. By means of a reduction to the center manifold computed as described in Section 2.1, the authors show the dynamics of the BCP in an extended neighborhood of L_1. The results show that the vertical and horizontal (quasi-periodic) Lyapunov families undergo a (quasi-periodic) pitchfork bifurcation that gives rise to the well-known Halo family (now quasi-periodic). In this sense the qualitatively behavior is similar the RTBP, as described in [Jorba and Masdemont, 1999, Gómez and Mondelo, 2001].

1.2.2 The Quasi-Bicircular Problem

The Quasi-Bicircular Problem (QBCP) is time-periodic perturbation of the RTBP that accounts for the effect of the Sun's gravity. The only difference with the BCP is how the motion of the primaries is modeled. Contrary to the case of the BCP, in the QBCP the motion of the primaries is coherent; this is, the motion follows Newton's equations, and it is a solution of the general Three Body Problem for the Sun-Earth-Moon system. Of course, there are some simplifications: for example, the motion of the three massive bodies is coplanar.

This model was first introduced in [Andreu, 1998], and the reader is referred there for the details on the construction of the model. In this section we provide an overview of the basic steps to construct the model. The first step is to compute a quasi-bicircular solution that models the motion of the Sun, the Earth, and the Moon under each other's gravitational influence. This is accomplished by expressing the general Three Body Problem in the Jacobi formulation. Then, an approximation to the Jacobi decomposition of the general Three Body Problem is obtained as Fourier series, solving for the coefficients. The details are in [Andreu, 1998].

With this solution, the origin of the (inertial) reference frame is translated from the center of masses of the Sun, Earth, and Moon to the Earth-Moon barycenter. Then, the reference frame is rotated such that the x-axis contains both the Earth and the Moon. A third change is a time-dependent transformation that keeps the Earth and the Moon fixed on the x-axis. This defines a pulsating reference frame with period equal to one revolution of the Earth and the Moon around their common barycenter.

Also, the unit of distance is scaled such that the distance between the Earth and the Moon is equal to one, the time is scaled such that one revolution of the pulsating reference frame is equal to 2π, and the unit of mass is scaled such that $m_E + m_M = 1$, where m_E (resp. m_M) is the mass of the Earth (resp. Moon). With these transformations, the Earth is located at $(\mu, 0, 0)$ and the Moon at $(1-\mu, 0, 0)$. These are the same scalings and transformations done in the RTBP and the BCP.

With this, the Hamiltonian of the system is:

$$\begin{aligned} H_{QBCP} = \frac{1}{2}\alpha_1(P_X^2 + P_Y^2 + P_Z X^2) + \alpha_2(P_X X + P_Y Y + P_Z Z) + \alpha_3(P_X Y - P_Y X) \\ + \alpha_4 x + \alpha_5 y - \alpha_6\left(\frac{1-\mu}{R_{PE}} - \frac{\mu}{R_{PM}} - \frac{m_S}{R_{PS}}\right) \end{aligned} \tag{1.9}$$

where:

- $R_{PE}^2 = (X-\mu)^2 + Y^2 + Z^2$ is the distance of the massless particle P to the Earth
- $R_{PM}^2 = (X-\mu+1)^2 + Y^2 + Z^2$ is the distance of P to the Moon
- $R_{PS}^2 = (X-\alpha_7)^2 + (Y-\alpha_8)^2 + Z^2$ is the distance of P to the Sun

The coefficients $\alpha_i, i = 1, ..., 8$ are 2π-periodic real functions of the form:

$$\alpha_i(\vartheta) = a_0^i + \sum_{k\geq 0} a_k^i \cos(k\vartheta) + \sum_{k\geq 0} b_k^i \sin(k\vartheta) \tag{1.10}$$

The values for the coefficients a_k^i, b_k^i can be found in [Andreu, 1998]. A property of the coefficients $\alpha_i, i = 1, ..., 8$ that they are odd functions for $i = 1, 3, 4, 7$, and even for the rest. These properties imply that the following symmetry holds:

$$H_{QBCP}(\vartheta, X, Y, Z, P_X, P_Y, P_Z) = H_{QBCP}(-\vartheta, X, -Y, Z, -P_X, P_Y, -P_Z)$$

Also, the physical interpretation of these coefficients is:

- $\alpha_1(\vartheta)$, $\alpha_2(\vartheta)$, $\alpha_3(\vartheta)$, and $\alpha_6(\vartheta)$ capture instantaneous distance between the Earth and the Moon
- $\alpha_4(\vartheta)$ and $\alpha_5(\vartheta)$ are the instantaneous Coriolis effect due to the rotating reference frame
- $\alpha_7(\vartheta)$ and $\alpha_8(\vartheta)$ capture the instantaneous position of the Sun the plane of motion

For this thesis, values used are in Table 1.3

Table 1.3: Parameters of the QBCP.

$\mu =$ `0.012150581600000`	$m_s =$ `328900.5423094043`
$\omega_s =$ `0.925195985520347`	$a_s =$ `388.8111430233511`

The reference [Andreu, 1998] contains a catalog of several periodic orbits resonant with the frequency of the Sun. These orbits were computed by means of continuation from the RTBP. In addition to periodic orbits, by means of the Lindstedt-Poincaré method, they found analytical approximations of quasi-periodic orbits around L_1 and L_2 and also estimates of their stability. The results show that there are planar quasi-periodic Lyapunov orbits that undergo a bifurcation where a new family of quasi-periodic orbits with a non-zero vertical component is born.

Also in [Andreu, 1998], by means of a reduction to the center manifold, a description of the dynamics around L_2 is presented. Understanding the dynamics of the L_2 in Earth-Moon under the effect of the Sun is one of the main motivation of the QBCP. Although the expression of the center manifold obtained only works for low levels of energy, a good description of several types of orbits in a neighborhood around L_2 is obtained. These results are also captured in [Andreu, 2002]. Finally, another know result form [Andreu, 1998] is that some of the Halo orbits computed survive in a full ephemeris model.

In [Le Bihan et al., 2017a] the authors studied the dynamics around the Earth-Moon L_1 and L_2 collinear points by means of reduction to the center manifold in the context of the QBCP. The approach to compute reduction to the center manifold is not the same as the one used in this thesis, or in [Andreu, 2002]. The approach is by means of the parametrization method. The parametrization method provided high-order periodic semi-analytical approximations of the center manifolds around the libration points. The results showed that for low energy levels, the phase state around the dynamical equivalents of the libration points L_1 and L_2 is foliated by invariant tori around a fixed point. As the energy level increases, a bifurcation occurs, giving rise to a new family of orbits with out-of-plane component. In the synodic frame, these fixed points correspond to 2D invariant tori, and the invariant tori around them to 3D invariant tori. This is similar to what is observed in a vicinity of the L_1 point in the BCP (see [Jorba et al., 2020]).

In the work presented in [Le Bihan et al., 2017a] the authors consider the QBCP as presented here; this is, with the Earth and the Moon fixed in a pulsating rotating frame and the Sun following its orbit. However, an additional perspective is offered where the Sun and the Earth-Moon barycenter are fixed in a suitable pulsating rotating frame. The latter formulation is a periodic time-dependent perturbation of the Sun-Earth/Moon RTBP. Hence, the Sun-Earth/Moon libration points become periodic orbits with the same period of the perturbation. As result, the authors have effectively ten regions of the phase space with invariant objects around them. Following this viewpoint of the QBCP, in [Le Bihan et al., 2017b] the authors study natural connections between libration points in the Earth-Moon System, and libration points in the Sun-Earth/Moon.

Finally, in [Jorba-Cuscó et al., 2020], the authors expanded the QBCP to include the effect of the Solar Radiation Pressure (SRP). Then, this augmented QBCP model is applied to a solar sail and its effects on the dynamic is studied. The main result is that the SRP has a stabilizing effect on some resonant Halo orbits.

1.3 Structure of this dissertation

In this last section of the Introduction we elaborate on the structure of this dissertation and its contents.

In Chapter 2, we describe the numerical methods used in this work. As already mentioned, the fundamentals of these methods are well-known and documented. Due to the fact that these methods are fairly complex in nature, and that they have been modified to overcome the highly unstable nature of the L_1 and L_2 regions, we think they deserve their own chapter.

In Chapter 3 we focus our attention on the L_2 region of the BCP model. The first attempt to qualitatively get an insight on the dynamics around the L_2 is by a reduction to the center manifold. It shown that the domain of convergence is too small to provide any relevant information. Hence, we move on to the computation of families of invariant tori. A total of six families are obtained. Two of them are planar 2D tori contained in the plane of motion of the two primaries. When analyzing the stability properties of these families, three bifurcations are found: two in one of the families, and one in the other one. From these bifurcations, three new families of invariant 2D are born, all of them with out-of-plane components. In addition to these five families, the RTBP Halos are continued from the RTBP to the BCP, showing that some Halo orbits persist under the perturbation of the Sun. Finally, the stability of a selected subset of these families and their suitability for space mission is discussed.

In Chapter 4 we study some aspects of the dynamics around the L_1 and L_2 points in the QBCP. In this case, the reduction to the center manifold has big enough domain of convergence to provide good information about the phase space in a neighborhood of L_1 and L_2. The results are qualitatively consistent with other references in the literature that study the phase space around L_1 and L_2 using different approaches to compute the center manifold (see [Le Bihan et al., 2017a]). For both L_1 and L_2, the main result of this analysis is that the horizontal quasi-periodic orbits counterparts of the RTBP Lyapunov families in the QBCP, undergo a (quasi-periodic) pitchfork bifurcation that gives rise to a new family of quasi-periodic orbits with out-of-plane component. In addition to center manifold, the families of invariant tori are computed around the L_1 and L_2 regions. The first families continued are the quasi-periodic planar and vertical Lyapunov, and their stability discussed. In the quasi-periodic planar Lyapunov, for both cases the bifurcation observed in the center manifold is identified and continued. From this bifurcation there is one family of 2D tori with out-of-plane component that corresponds to the family identified in the center manifold. In addition to these families, the RTBP Halo orbits around the L_1 and L_2 points are continued from the RTBP to the QBCP. These numerical experiments show that some Halo orbits from the RTBP survive the effect of the Sun's gravity, and that in the QBCP they seem not to be connected to the bifurcation of the quasi-periodic planar Lyapunov. For the L_2 case, we provide some numerical evidence that supports that a conjecture presented in [Andreu, 1998] is true. This conjecture stated that the family of Halo orbits that survive in the QBCP is connected to another family of 2D tori resonant with the frequency of the Sun.

Finally, in Chapter 5 we study the transfer from a parking orbit around the Earth to different Halo-like objects around L_2. By means of computing the unstable invariant manifolds of these objects, we show that there are one-maneuver transfers from the Earth to a vicinity of the Moon. Also, in terms of cost (ΔV) and time of transfer, the results are consistent with the literature. We successfully show this for both the BCP and QBCP. The relevance of these results show up when comparing how the invariant manifolds behave in the Earth-Moon RTBP. In the Earth-Moon RTBP, the invariant manifolds associated to the Halo orbits around L_2 do not pass close to parking orbit around the Earth (see [Bernelli Zazzera et al., 2004]). However, in the BCP and QBCP they do, opening the door to one-maneuver transfers to Halo orbits around L_2.

The last part of this thesis are the conclusion and the appendixes. The conclusions outline the major contributions of this work and future work. The appendixes capture some details that are relevant, but were taken apart from the main text to make the reading more pleasant.

Chapter 2

Numerical Methods

To study the phase space of a dynamical system, a typical approach is to look for invariant objects and analyze their stability. Typically, the analysis starts looking for equilibrium points, then periodic orbits, 2D tori, and so on. These objects, their stability, and their associated invariant manifolds provide information about how the dynamic is organized in the phase state. From a numerical point of view, computing equilibrium points, or periodic orbits (and families, if they exist) is relatively easy. In some cases this is enough (for example, two dimensional systems), but usually this gives limited information on the dynamics. Because for astrodynamical applications we are typically interested in systems with at least 2 degrees of freedom, we need to rely on techniques that allows us to get a more in depth view of the phase space. This chapter describes the techniques employed in this thesis to study the dynamics around the L_1 and L_2 points in the BCP and the QBCP. These are well-known techniques and can be found in the literature, and here we explain the modifications we made to adapt them to the specific needs of our scenarios.

One approach to get the full picture of the dynamics around an invariant object is to do a reduction to the center manifold. This approach consists in a series of changes of variable to decouple the saddles from the centers; this is, the hyperbolic (or unstable) motion from the neutral one. This decoupling allows to reduce the dimension of the system, and to focus only on the invariant objects that live in the center manifold. This technique has been proven very successful to characterize the dynamics around the collinear points in the RTBP for different mass parameters (see [Jorba and Masdemont, 1999]); around the L_1 point the BCP (see [Jorba et al., 2020]) and L_2 in the QBCP (see [Andreu, 2002], [Le Bihan et al., 2017a]); or around the L_1 and L_2 points in the Sun-Earth RTBP for solar sails (see [Farrés and Jorba, 2010]). Note that the systems that can be studied with this technique are very broad: the reference [Jorba and Masdemont, 1999] deals with autonomous Hamiltonians, the references [Jorba et al., 2020], [Andreu, 2002], and [Le Bihan et al., 2017a] with Hamiltonians that depend periodically on the time, and the reference [Farrés and Jorba, 2010] with general Ordinary Differential Equations. The interested reader is referred to [Carr, 1981, Sijbrand, 1985, Vanderbauwhede, 1989] for a more general treatise on the center manifold and its applications. The main advantage of this method is that it provides a comprehensive picture of orbits staying in a neighborhood of an invariant object and its bifurcations. The disadvantages are that, due to the construction of the center manifold, the neighborhood where it is valid may be very small, for instance due to the presence of small divisors. An overview of this method framed in context of periodic time-dependent Hamiltonian systems is explained in Section 2.1.

An alternative to the center manifold is to directly compute the families of invariant objects that shape the phase space of the dynamical system (equilibrium points, periodic orbits, 2D tori and so on). A key advantage of this approach is that it is not limited by radius of convergence of a series expansion, and usually it can provide information on a large neighborhood of the region of the phase space under study. Also, in some cases (equilibrium points, periodic orbits, and 2D tori) there are techniques to compute the stability of each member of the family. The main limitation of this approach is that the continuation of families of tori of dimension higher than two is more expensive computationally (see [Jorba and Olmedo, 2009]) and, sometimes, cumbersome. In the context of the BCP, the complexity involved in computing invariant tori with more than two basic frequencies is illustrated in [Castellà, 2003], where the authors computed families of 3D tori around the triangular points for the BCP, and in [Jorba and Olmedo, 2009], where the authors computed 3D, 4D, and 5D tori in the Sun-Jupiter system perturbed by the motion of Saturn, Uranus, Neptune, and the Earth.

In addition to that, the continuation of these objects involves some level of trial and error, and once the continuation process starts, a lot of fine tuning due to the presence of resonances is needed. Finally, and as opposed to the center manifold approach, this method provides an incomplete picture unless all relevant invariant objects are computed. An overview of the computation of 2D invariant tori families to study a neighborhood of the collinear points of the BCP and the QBCP is described in Section 2.2.

At this point it is important to note that the latter approach assumes the existence of families of invariant objects. The assumption deserves some explanation. For the sake of clarity, we fame the discussion in the context of the BCP. In the BCP, the existence of invariant tori is inherited from the RTBP. It is well know that around the collinear equilibrium points of the RTBP there are families of periodic orbits (planar and vertical Lyapunov, and Halo orbits) and quasi-periodic orbits (quasi-halos and Lissajous). See [Jorba and Masdemont, 1999] and [Gómez and Mondelo, 2001] for details. Under generic conditions of non-resonance and non-degeneracy, adding a small enough periodic (or quasi-periodic) time-dependent perturbation to RTBP, causes the existing invariant objects to inherit the frequencies of the perturbation. It is important to mention that the families of invariant objects become Cantorian because only those frequencies satisfying a suitable non-resonance condition survive. As a consequence, the families of objects are Cantorian, not continuous. The details on the proofs that back these statements can be found in [Jorba and Villanueva, 1997]. Finally, an example of this phenomena in the context of the RTBP and the BCP can be found in [Jorba et al., 2020].

In addition to the computation of invariant objects, we are also interested in computing their stability. For equilibrium points this is accomplished analyzing the spectra of the

Jacobian of the vector field evaluated at the equilibrium point. For periodic orbits, the spectra of the monodromy matrix (this is, the matrix obtained by integrating the variational equations over one period with initial condition equal to the identity) provides us the linear stability of the periodic orbit. For the next level, this is, 2D invariant tori, it is also possible to study their stability. The method used in this thesis is a modification of [Jorba, 2001] for highly unstable tori, and it is explained in Section 2.3.

Finally, associated to the invariant objects that have a hyperbolic direction there are stable and unstable manifolds. These manifolds are also important because they connect the invariant object with different parts of the phase space. In the context of this thesis this is specially relevant because these connections may provide transfers from a region of interest in the phase space (for example, a neighborhood of the Earth) to an invariant object (for example, a 2D torus around the L_2 region in the BCP). The method to compute these invariant manifold follows the ideas described in [Simó, 1990], and this is explained in Section 2.4.

2.1 Normal forms and reduction to the center manifold

Let us start with a real, analytical, periodically time-dependent n-degrees of freedom Hamiltonian $H \in \mathcal{C}^\omega(\mathbb{T}^1 \times \mathbb{R}^n \times \mathbb{R}^n)$ of the form:

$$H(\theta, X, Y) = \sum_{k\geq 2} H_k(\theta, X, Y) \tag{2.1}$$

that is 2π-periodic on $\theta = \omega_S t$, $X = (x_1, ..., x_n)$ are the positions, and $Y = (y_1, ..., y_n)$ the conjugated momenta. Also, each $H_k, k \geq 2$ is a homogeneous polynomial on X, Y of degree k with 2π-periodic coefficients on θ, $a_K(\theta) \in \mathcal{C}^\omega\big(\mathbb{T}^1\big)$. This is,

$$H_k(\theta, X, Y) = \sum_{|K|=k} a_K(\theta) X^{K^0} Y^{K^1}, \quad a_K(\theta) = \sum_{j\geq 0} a_K^j e^{i\theta j}, \tag{2.2}$$

where $K = (K^0, K^1)$, $K^0 = (k_1, ..., k_n)$, $K^1 = (k_{n+1}, ..., k_{2n})$, $k_i \in \mathbb{N}$, and

$$X^{K^0} Y^{K^1} = x_1^{k_1} \cdot ... \cdot x_n^{k_n} y_1^{k_{n+1}} \cdot ... \cdot y_n^{k_{2n}}, \quad |K| = \sum_{l=0}^{1} |K^l|, \quad |K^j| = \sum_{i=1}^{n} k_{j\cdot n+i}, \quad j = 0, 1. \tag{2.3}$$

Finally, note that due to the fact that there are no linear terms in the Hamiltonian (2.1), the origin is an equilibrium point. We assume also that the origin has exactly one hyperbolic direction. We acknowledge the fact that the Hamiltonians we defined in Section 1.2.1 and Section 1.2.2 are not of this form, and this will be addressed that later in this section.

We note that the non-autonomous Hamiltonian can be transformed to an autonomous one if an extra variable Y_θ is added to act as the conjugated momentum of the angle θ. With that, the Hamiltonian (2.1) looks like:

$$H(\theta, Y_\theta, X, Y) = \omega_S Y_\theta + \sum_{k\geq 2} H_k(\theta, X, Y). \tag{2.4}$$

The transformation to a normal form is a technique that consists in applying a set of (canonical) changes of variables on H to study a vicinity of an equilibrium point. Hence, normal forms provide *local* information. This local analysis requires the resulting Hamiltonian $K(\theta, Q, P) = \sum_{k\geq 2} K_k(\theta, Q, P)$ to be *simpler* than the original one. What "simpler" means depends of the context and the information we are trying to obtain. This last statement is illustrated with an example from Linear Algebra: given an n-dimensional linear space E and an endomorphism $A : E \to E$, we want to study the properties of the matrix A. If we are interested only in, for example, finding out if A is similar to another matrix B, it may be enough to compute the Frobenius normal form for both A and B and compare them. On the other hand, if we are interested in studying the invariant subspaces of A, we may want to compute the Jordan normal form. Both transformations serve different purposes, and both are normal forms. The same reasoning applies to Hamiltonian systems, with the understanding that the normal forms in Linear Algebra are global, as opposed to the ones presented here.

In the context of this thesis we are interested in a normal form of the periodic time-dependent Hamiltonian (2.1) around the origin in order to:

1. Decouple (up to certain order) the hyperbolic part from the central one
2. Remove (up to certain order) the explicit time dependency

We call this normal form the *reduction to the center manifold* of H. After this process, we obtain a Hamiltonian that, up certain order, is autonomous and has a first integral I_1 associated to the hyperbolic direction. Hence, if we set $I_1 = 0$, the system is reduced in one degree of freedom; this is, to a $(n-1)$-degrees of freedom Hamiltonian. We note that there construction of a center manifold is not unique (see [Andreu, 2002], and the discussion in Chapter 4).

For a Hamiltonian like the one described in Equation (2.1), the reduction to the center manifold is a two-step process:

1. Apply a symplectic Floquet transformation (+ complexification) to put the quadratic terms of the Hamiltonian in diagonal form
2. By means of the Lie transform method, put the final Hamiltonian in the desired form

Before moving forward, let us note that the Hamiltonians we are considering in this work (see Section 1.2.1 and Section 1.2.2) are not in the form of (2.1). First, due to their non-autonomous nature, there are no equilibrium points. There are, however, periodic orbits (see Section 3.1, and Section 4.1). Second, the Hamiltonians of BCP and QBCP are not expressed as a series of homogeneous polynomials. Hence, two extra steps need are required. The first step is to translate and scale[2] the periodic orbit around which want to do the normal form to the origin by means of a time-dependent change of variables. This way,

---

[2] Scaling is not a canonical transformation. The idea is to do the scaling in the vector field, and then derive the Hamiltonian.

the origin is an equilibrium point and the constant and linear terms are removed from the Hamiltonian. The scaling is trivial, and its purpose is to redefine the unit of distance. This is optional, but it is useful to set the radius of convergence of the resulting series equal to one. An example in the context of the RTBP can be found in [Jorba and Masdemont, 1999], where authors compute the center manifold around the collinear point L_1 and L_2, scale the variable by a factor equal to distance from the equilibrium point and the closet primary. The details on how to do the translation of periodic orbits to the origin is in Appendix A.

The second step is the expansion of the non-linear terms (i.e., the potentials of the Sun, Earth, and Moon) as homogeneous polynomials. The details of this expansion can be found in Appendix B. By performing these two steps, we have a the Hamiltonian of our system in the form of Equation (2.1). Examples of this for the RTBP can be found in [Jorba and Masdemont, 1999, Gómez and Mondelo, 2001], and for the BCP in [Gómez et al., 1993a, Jorba et al., 2020].

The rest of the section is structured as follows: subsection 2.1.1 explains the Floquet transformation for Hamiltonians. As mentioned before, this transformation puts the Hamiltonian in a convenient expression. With that, the next step is to apply the Lie transform to obtain the desired normal form. Subsection 2.1.2 elaborates on the Lie transform to obtain the center manifold. Finally, subsection 2.1.3 explains numerical tests to verify the correct implementation of the reduction to the center manifold, and analysis of the radius of convergence of the transformation.

2.1.1 Symplectic Floquet transformation

Given a linear ordinary differential equation (not necessarily Hamiltonian) with coefficients that depend periodically on time, it is well know that there exists a (non-unique, and maybe complex) time-dependent change of variables that reduces the equation to a linear differential equation with constant coefficients. This result is the Floquet Theorem for ordinary differential equations (see, for example, [Arrowsmith and Place, 1990] for an exposition on the context of time-dependent normal forms). In this section we present, without a proof, the symplectic version of the Floquet Theorem. Details on the proof can be found in [Gómez et al., 1993b].

Theorem 1 (Symplectic Floquet Theorem). *Let*

$$H(\theta, X, Y) = X^T A(\theta) X + X^T B(\theta) Y + Y^T C(\theta) Y \tag{2.5}$$

be an n-degrees of freedom Hamiltonian, where $A(\theta), B(\theta), C(\theta) \in \mathcal{C}^0(\mathbb{T}^1, M_n\mathbb{C})$, and $A(\theta)$, $C(\theta)$ are symmetric for all θ. Then, there exist a symplectic, linear and periodic time-dependent change of variables that transforms the Hamiltonian (2.5) into a new autonomous Hamiltonian H_F on variables (x, y):

$$H_F(x, y) = x^T \hat{A} x + x^T \hat{B} y + y^T \hat{C} y$$

and with $\hat{A}, \hat{B}, \hat{C} \in M_n\mathbb{C}$, and $\hat{A}, \hat{C}$ symmetric matrices.

If we look at the vector field associated to H_F, it is a linear differential equation with constant coefficients. However, as the Floquet transformation is not unique, these coefficients are also not unique either. The following paragraphs provide some details on the implementation of the Symplectic Floquet Theorem, and discuss the non-uniqueness aspects of the transformation.

The starting point is the vector field defined by the Hamiltonian (2.4). This is:

$$\begin{cases} \dot{Z} & = & \Xi(\theta)Z \\ \dot{\theta} & = & \omega \end{cases} \tag{2.6}$$

where $Z^T = (X^T, Y^T) \in \mathbb{R}^{2n}$, $\theta \in \mathbb{T}^1$, and

$$\Xi(\theta) = \left[\begin{array}{c|c} B(\theta)^T & 2C(\theta) \\ \hline -2A(\theta) & -B(\theta) \end{array}\right] \in \mathbb{R}^{2n \times 2n}. \tag{2.7}$$

Our goal is to find a symplectic time-periodic change of variables $z = P(\theta)Z$, where $z^T = (x^T, y^T) \in \mathbb{R}^n \times \mathbb{R}^n$ such that the resulting linear Hamiltonian vector field has constant coefficients. This is:

$$\dot{z} = \Upsilon z, \quad \Upsilon \in \mathbb{R}^{2n \times 2n} \tag{2.8}$$

The construction of this change involves several steps. The first one is the computation of the monodromy matrix M of Equation (2.6). This is accomplished by integrating Equation (2.6) over one period of time, $T = 2\pi/\omega$, with initial condition $M(0) = I$. We assume that all eigenvalues have multiplicity one. Hence, the matrix M can be transformed into a diagonal matrix D_M by means of a linear transformation S. This is, $D_M = S^{-1}BS$, where $D_M = \text{diag}(\lambda_j)$, $\lambda_j \in \text{Spec}(M), j = 1, ..., 2n$ is a diagonal matrix. Let us assume that D_M is of the form:

$$D_M = \begin{bmatrix} \mathcal{U} & 0 & 0 \\ 0 & \mathcal{S} & 0 \\ 0 & 0 & \mathcal{C} \end{bmatrix} \in \mathbb{R}^{2n \times 2n}$$

such that $\mathcal{U}, \mathcal{S} \in M_d(\mathbb{R})$ are d-dimensional diagonal real matrices, and $\mathcal{C} \in M_{2r}(\mathbb{C})$ is a $2r$-dimensional diagonal complex matrix. (Note that $d + r = n$.) These matrices are constructed such that they organize the spectrum of M the following way: $\text{Spec}(\mathcal{U}) = \{\lambda \in \text{Spec}(M), \lambda \in \mathbb{R} || \lambda| > 1\}$, $\mathcal{S} = \mathcal{U}^{-1}$, and $\text{Spec}(\mathcal{C}) = \{\lambda \in \text{Spec}(M), \lambda \in \mathbb{C} || \lambda| = 1\} \in \mathbb{S}^1$. In other words, the submatrices $\mathcal{U}, \mathcal{S}$ correspond to the hyperbolic part of Equation (2.6), and the submatrix $\mathcal{C}$ to the elliptic part. Note that the relationship $\mathcal{S} = \mathcal{U}^{-1}$ holds due to the Hamiltonian structure of Equation (2.4). Also, another consequence is that if $\lambda \in \text{Spec}(C)$, then $\bar{\lambda} \in \text{Spec}(C)$.

Once we have the monodromy matrix M and its transformation into D_M by S, the next step is to take the logarithm of the matrix M; this is, to find a matrix $B \in M_{2n}(\mathbb{R})$ such that

$$M = e^{BT}.$$

The first step to construct the matrix B is to take the logarithm of the matrix D_M. We compute the following values:

- $\alpha_i \in \mathbb{R}$ such that $\lambda_i = e^{\alpha_i T}, \lambda_j \in \operatorname{Spec}(\mathcal{U}), j = 1, ..., d$
- $\omega_i \in \mathbb{R}$ such that $\lambda_i = e^{i\omega_i T}, \lambda_j \in \operatorname{Spec}(\mathcal{C}), j = 1, ..., r$ and, for $j > 1$, $\lambda_j \neq \bar{\lambda}_l$, $l = 1, ..., j-1$

Hence, defining:

$$D_B = \frac{1}{T}\log(D_M) = \operatorname{diag}(\alpha_1, ..., \alpha_d, -\alpha_1, ..., -\alpha_d, i\omega_1, ..., i\omega_r, -i\omega_1, ..., -i\omega_r)$$

and by applying the transformation S we obtain $B = S^{-1}D_B S$.

An important remark is that the values $\omega_j, j = 1, ..., r$ are not uniquely defined. Note that these are computed by taking the complex logarithms of the complex eigenvalues. Hence, the values $\pm(\omega_i + \frac{2\pi k}{T}), k \in \mathbb{Z}$ are also acceptable. An example is discussed in Section 4.2.2.

Finally, we compute the transformation R that puts matrix B into its real Jordan form J_B. This is:

$$J_B = RBR^{-1} = \left[\begin{array}{c|c} A & \Omega \\ \hline -\Omega & -A \end{array}\right] \in M_{2n}(\mathbb{R}),$$

where:

$$A = \begin{bmatrix} \alpha_1 & \dots & 0 & 0 & \dots & 0 \\ \vdots & \ddots & \vdots & \vdots & \ddots & \vdots \\ 0 & \dots & \alpha_d & 0 & \dots & 0 \\ 0 & \dots & 0 & 0 & \dots & 0 \\ \vdots & \ddots & \vdots & \vdots & \ddots & \vdots \\ 0 & \dots & 0 & 0 & \dots & 0 \end{bmatrix} \in M_n(\mathbb{R})$$

$$\Omega = \begin{bmatrix} 0 & \dots & 0 & 0 & \dots & 0 \\ \vdots & \ddots & \vdots & \vdots & \ddots & \vdots \\ 0 & \dots & 0 & 0 & \dots & 0 \\ 0 & \dots & 0 & \omega_1 & \dots & 0 \\ \vdots & \ddots & \vdots & \vdots & \ddots & \vdots \\ 0 & \dots & 0 & 0 & \dots & \omega_r \end{bmatrix} \in M_n(\mathbb{R})$$

The matrix $R \in M_{2n}(\mathbb{R})$ is constructed with the eigenvectors associated to the eigenvalues of M. The first n columns are the real part of the eigenvectors, and the last n columns the imaginary part.

The last step is to compute the transformation $P(\theta)$ that casts Equation (2.6) into Equation (2.8). This is accomplished by solving the following initial value problem:

$$\left\{ \begin{array}{rcl} \dot{P}(\theta) & = & \Xi(\theta)P(\theta) - P(\theta)B, \quad P(0) = R \\ \\ \dot{\theta} & = & \omega \end{array} \right. \tag{2.9}$$

Finally, defining the change of variables $\bar{z} = P(\theta)Z$, where $\bar{z}^T = (\bar{x}^T, \bar{y}^T) \in \mathbb{R}^n \times \mathbb{R}^n$, Equation (2.5) becomes:

$$\bar{H}_F(\bar{x}, \bar{y}) = \sum_{j=1}^{d} \alpha_j \bar{x}_j \bar{y}_j + \frac{1}{2} \sum_{j=1}^{r} \omega_j (\bar{x}_{j+d}^2 + \bar{y}_{j+d}^2). \tag{2.10}$$

(Recall that $d + r = n$.) Note that (2.10) is autonomous and with real coefficients. A final step, not mandatory but recommended for computational purposes, is to *complexify* the Hamiltonian defined by (2.10) using the following (complex) change of variables:

$$\bar{x}_j = \frac{x_j + iy_j}{\sqrt{2}}, \quad \bar{y}_j = \frac{ix_j + y_j}{\sqrt{2}}, \quad j = 1, ..., n. \tag{2.11}$$

By applying the change of variable defined by (2.11), the Hamiltonian defined by Equation (2.10) becomes:

$$H_F(x, y) = \sum_{j=1}^{d} \alpha_j x_j y_j + \sum_{j=1}^{r} i\omega_j x_{j+d} y_{j+d}, \tag{2.12}$$

and it is fully characterized by the vector:

$$\bar{\omega} = (\alpha_1, ..., \alpha_d, i\omega_1, ..., i\omega_r) \tag{2.13}$$

2.1.2 Lie transform

The starting point of this section is the Hamiltonian (2.4) with the terms of degree two in the Floquet normal form:

$$H(\theta, y_\theta, x, y) = \omega_S y_\theta + H_F(x, y) + \sum_{k \geq 3} H_k(\theta, x, y), \tag{2.14}$$

where $x, y \in \mathbb{R}^n$, $x = (x_1, ..., x_n)^T, y = (y_1, ..., y_n)^T$; $H_F(x, y)$ contains the term of degree 2, and it is in the same form as Equation (2.12) with $d = 1$; and $H_k, k \geq 3$ is as defined in Equation (2.2) and Equation (2.3):

$$H_k(\theta, x, y) = \sum_{|K|=k} a_K(\theta) x^{K^0} y^{K^1}. \tag{2.15}$$

For the sake of simplicity we kept the same name H after applying the Floquet transformation. We recall that the Hamiltonian (2.14) is autonomous because it was expanded adding the conjugated momentum y_θ of the angle θ.

The goal of this section is to show that, by means of the Lie transform, it is possible to cancel some terms $a_K(\theta), |K| > 2$ and to remove the dependency on the angle θ. Let us start with an overview of the Lie transform.

We begin defining $E_k^{\mathbb{F}} := E_k^{\mathbb{F}}(x, y)$ as the space of homogeneous polynomials of degree k with coefficients in the field $\mathbb{F} = \{\mathbb{R}, \mathbb{C}\}$, and $(x, y) \in \mathbb{F}^{2n}$. If $f \in E_r^{\mathbb{F}}$ and $g \in E_s^{\mathbb{F}}$, the Poisson bracket of f and g is defined as follows:

$$\{f, g\} = \sum_{j=1}^{n} \frac{\partial f}{\partial x_j}\frac{\partial g}{\partial y_j} - \frac{\partial g}{\partial x_j}\frac{\partial f}{\partial y_j}$$

and $\{f, g\} \in E_{s+r-2}^{\mathbb{F}}$. Note that the Poisson bracket is defined for any pair of smooth enough functions, not necessarily homogeneous polynomials.

Now, to introduce the Lie transform, let us first state without proof a theorem for Hamiltonian flows (see [Meyer et al., 2008] for a proof):

Theorem 2. *Let $\bar{K} \in \mathcal{C}^{\omega}(\mathbb{R}^{2n})$ be a smooth autonomous Hamiltonian function. Let us consider the initial value problem:*

$$\begin{aligned} \frac{d}{dt}x &= +\frac{\partial \bar{K}}{\partial y} \\ \frac{d}{dt}y &= -\frac{\partial \bar{K}}{\partial x} \end{aligned} \tag{2.16}$$

with initial condition $(x(0), y(0)) = (x_0, y_0)$.

If $\phi_t(x, y)$ is the Hamiltonian flow solution of the initial value problem (2.16), then it is symplectic at time t.

Hence, as a consequence of this result $(q, p) = \phi_t(x, y)$ defines a canonical transformation for all t. In the same fashion, another relevant property of Hamiltonian flows and Poisson brackets is the captured in the following proposition:

Proposition 1. *Given a smooth Hamiltonian function $\bar{K}(x, y) \in \mathcal{C}^{\omega}(\mathbb{R}^{2n})$, a smooth function $f \in \mathcal{C}^k(\mathbb{R}^{2n}), k > 0$, and a solution $(x_0(t), y_0(t))$ of the initial value problem (2.16), then:*

$$\frac{d}{dt}f(x_0(t), y_0(t)) = \{f, \bar{K}\}(x_0(t), y_0(t)). \tag{2.17}$$

Proof.

$$\begin{aligned} \frac{d}{dt}f(x_0(t), y_0(t)) &= \frac{\partial f}{\partial x_0}\frac{d}{dt}x_0(t) + \frac{\partial f}{\partial y_0}\frac{d}{dt}y_0(t) \\ &= \frac{\partial f}{\partial x_0}\frac{\partial \bar{K}}{\partial y_0} - \frac{\partial f}{\partial y_0}\frac{\partial \bar{K}}{\partial x_0} \\ &= \{f, \bar{K}\}(x_0(t), y_0(t)) \end{aligned}$$

□

With these two results, we are now in a position to define a canonical change of variables as follows:

Let $\bar{K}(x,y) \in \mathcal{C}^\omega(\mathbb{R}^{2n})$ be the original Hamiltonian function in coordinates $(x,y) \in \mathbb{R}^{2n}$ and $G(x,y) \in \mathcal{C}^\omega(\mathbb{R}^{2n})$ another Hamiltonian function. The function G is called the *generating* function, and has associated to it a Hamiltonian flow $\phi_t^G(x,y)$ solving an initial value problem like (2.16). As per Theorem 2, $(q,p) = \phi_t^G(x,y)$ defines a canonical transformation.

Note that $(q,p) = (x,y)$ for $t = 0$. Hence, let us consider next the transformed Hamiltonian $\bar{K}^* = \bar{K}(\phi_t^G(x,y)) = \bar{K}(q,p)$, and expand it using the Taylor formula around $t = 0$:

$$\begin{aligned}
\bar{K}^*(q,p) &= \bar{K}(x,y) + \frac{d}{dt}\bar{K}(q,p) + \mathcal{O}(|t|^2) \\
&= \bar{K}(x,y) + \frac{\partial \bar{K}}{\partial q}\frac{\partial q}{\partial t} + \frac{\partial \bar{K}}{\partial p}\frac{\partial p}{\partial t} + \mathcal{O}(|t|^2) \\
&= \bar{K}(x,y) + \{\bar{K}, G\}(x,t)t + \mathcal{O}(|t|^2).
\end{aligned}$$

The last equality is done applying Proposition 1. At this point, it is not difficult to see that the formal expansion to higher orders is:

$$\bar{K}^* = \bar{K} + t\{\bar{K},G\} + \frac{t^2}{2!}\{\{\bar{K},G\},G\} + \frac{t^3}{3!}\{\{\{\bar{K},G\},G\},G\} + \cdots \tag{2.18}$$

Hence, we then define the Lie transform of $\bar{K}$ by means of the generating function G as the time 1 flow of the Hamiltonian G. This is Equation (2.18) evaluated at $t = 1$:

$$\bar{K}^* = \bar{K} + \{\bar{K},G\} + \frac{1}{2!}\{\{\bar{K},G\},G\} + \frac{1}{3!}\{\{\{\bar{K},G\},G\},G\} + \cdots$$

and it is valid on the domain of convergence of the series. See [Giorgilli et al., 1989] and references therein for more details.

Now that we have defined the Lie transform, we want to apply it to compute the reduction to the center manifold of the Hamiltonian (2.14); this is, to decouple (up to certain order) the hyperbolic part from the elliptic one, and to remove (up to certain order) the time dependency. Note that we chose $d = 1$ (this is, only one saddle) strictly for convenience and to simplify the exposition, but the method is applicable to any number of saddles. Note also that by construction the pair (x_1, y_1) corresponds to the saddle.

In this paragraph we are going to detail how to remove the time dependency for the terms of degree equal to three. The same reasoning applies for the subsequent degrees. Let us start with an generating function $G_3 \in E_3^{\mathbb{C}}$ of the form:

$$G_3 = \sum_{|K|=k} g_K(\theta) x^{K^0} y^{K^1}, \quad g_K(\theta) = \sum_{j \geq 0} g_K^j e^{i\theta j},$$

with unknown coefficients g_K^j. Note that these unknown coefficients of G_3 depend periodically on the time. The objective is to compute these coefficients such that the time dependency is removed.

Computing the Poisson bracket of the Hamiltonian H from Equation (2.14) and G_3 we obtain the following expression:

$$\{H, G_3\} = \{\omega y_\theta, G_3\} + \{H_F, G_3\} + \{H_3, G_3\} + \sum_{k>3} \{H_k, G_3\}. \tag{2.19}$$

We note that:

$$\{\omega_S y_\theta, G_3\} = -\omega_S \frac{\partial G_3}{\partial \theta} \in E_3^{\mathbb{C}},$$

$$\{H_F, G_3\} = \sum_{|K|=3} \langle \bar{\omega}, K^1 - K^0 \rangle g_K(\theta) x^{K^0} y^{K^1} \in E_3^{\mathbb{C}},$$

$$\{H_k, G_3\} \in E_{k+1}^{\mathbb{C}}, k \geq 3,$$

where $\bar{\omega}$ is as in (2.13) and $\langle \cdot, \cdot \rangle$ denotes the scalar product:

$$\langle \bar{\omega}, K^1 - K^0 \rangle = \alpha_1 (k_{n+1} - k_1) + i \sum_{l=2}^{n} \omega_{l-1} (k_{n+l} - k_l).$$

Then, we have that the homogeneous polynomial of degree three of the transformed Hamiltonian is

$$H_3^* = H_3 - \omega_S \frac{\partial G_3}{\partial \theta} + \sum_{|K|=3} \langle \bar{\omega}, K^1 - K^0 \rangle g_K(\theta) x^{K^0} y^{K^1}. \tag{2.20}$$

Now, imposing $H_3^* = \sum_{|K|=3} h_K(\theta) x^{K^0} y^{K^1}$ and grouping all the terms with the same K in Equation (2.20), we obtain the following set of linear differential equations where g_K^j are the unknowns:

$$\omega_s \frac{d g_K^j}{d\theta} - \langle \bar{\omega}, K^1 - K^0 \rangle g_K^j = a_K^j - h_K^j, \quad j \geq 0. \tag{2.21}$$

The set of solutions that solve for the unknown g_K^j in Equation (2.21) is:

$$g_K^j(\theta) = \sum_{j \notin J_3} \frac{a_K^j - h_K^j}{i\omega_s j - \langle \bar{\omega}, K^1 - K^0 \rangle} e^{i\theta j}, \quad j \geq 0, \tag{2.22}$$

where $J_k = \{j \in \mathbb{Z} \quad | \quad |K| = k, \quad i\omega_s j - \langle \bar{\omega}, K^1 - K^0 \rangle = 0\}$; this is, J_k is the set of resonant terms. Note that if $j \in J_k$, we have to impose $a^j_K = h^j_K$, but for $j \notin J_k$ we have freedom to chose the values for h^j_K.

At this point, it is clear that if we want to remove the time dependency for H_3, we need to chose the values $h^j_K = 0, j > 0$ with the understanding that $j \notin J_k$. Fortunately, this is usually the case in the models used in this dissertation.

Note that if in addition to setting $h^j_K = 0, j > 0$ we also chose $h^0_K = 0$, not only we remove the dependency on the time but also the monomial associated to the coefficients a^j_K. We refer to this operations as to *kill* a monomial. We now explain how this result has been applied in the present work to compute the reduction to center manifold.

Recall that the coordinates (x_1, y_1) are the ones associated to the hyperbolic part of the system, and their exponents in K are k_1 and k_{n+1} respectively. Now, if we kill all the monomials that have $k_1 \neq k_{n+1}$ and the time up to order N, we end up with a Hamiltonian that looks like:

$$H^*(x, y) = H^N(x_1 y_1, x_2, ..., x_n, y_2, ..., y_n) + \mathcal{R}(x, y, \theta), \tag{2.23}$$

where R_N is the remainder and only contains homogeneous polynomials of degree $k > N$. Note that H^* depends on $x_1 y_1$, and not x_1 and y_1 individually. Hence, defining the change of variables $I_1 = x_1 y_1$ and its associated conjugated momentum ψ_1 to ensure it is canonical, the Hamiltonian system (2.23) becomes:

$$H^*(x, y) = H^N(I_1, x_2, ..., x_n, y_2, ..., y_n) + \mathcal{R}(I_1, \psi_1, x_2, ..., x_n, y_2, ..., y_n, \theta). \tag{2.24}$$

Note that if the remainder is neglected, the Hamiltonian $H^N(I_1, x_2, ..., x_n, y_2, ..., y_n)$ does not depend on ψ_1. Hence I_1 is a first integral of the system. If we set $I_1 = 0$, then the system defined by the Equation (2.24) is an N^{th}-order approximation of the center manifold. With this, we define the reduction to the center manifold as $(n-1)$-degrees-of-freedom Hamiltonian:

$$\bar{H}_{CM}(\bar{q}, \bar{p}) = H^N(0, q, p), \tag{2.25}$$

where $\bar{q} = (x_2, ..., x_n)^T, \bar{p} = (y_2, ..., y_n)^T \in \mathbb{C}^{(n-1)}$.

Note that by construction the coordinates $(\bar{q}, \bar{p})$ are complex. Hence, in order to get the real representation of the center manifold, we just need to revert the change defined in Equation (2.11) to get real variables $(q, p) \in \mathbb{R}^{(n-1)} \times \mathbb{R}^{(n-1)}$ and the $(n-1)$-degrees-of-freedom real Hamiltonian $H_{CM}(q, p)$ that captures the dynamics in the center manifold. See [Jorba, 1999] for further details.

As a final comment, let us remind that the center manifold is not unique. Hence, there are multiple way this can be constructed. This construction is essentially characterized by which monomials survive, and which ones don't. See for example [Andreu, 2002] for the case of the center manifold around L_2 in the QBCP.

2.1.3 Details on the implementation and tests

Both the Floquet transformation and the Lie transform are techniques than can be coded in a computer program. The Floquet transformation has been implemented following the proof of the symplectic Floquet theorem in [Gómez et al., 1993a]. The proof in that reference is constructive in nature and contains all the steps necessary for the codification into a software program. Section 2.1.1 contains a high level outline of the steps involved in this algorithms. The references [Andreu, 1998, Andreu, 2002, Gabern, 2003, Le Bihan et al., 2017a, Jorba-Cuscó, 2018] also contain details on the implementation for different models.

The implementation of the Lie transform is a little more involved. Note that the objects we are manipulating are homogeneous polynomials whose coefficients are Fourier series. Hence, two main software libraries are required to manipulate these objects: a Fourier series arithmetic to perform basic operations, and an algebraic manipulator for homogeneous polynomials.

The Fourier series arithmetic used in this dissertation was developed by Marc Jorba-Cuscó, and details on the implementation be found in [Jorba et al., 2020]. The algebraic manipulator to handle homogeneous polynomials used in this dissertation is based on the work presented in [Jorba, 1999]. The software documented in that reference is open source.[3] It is, however, designed to handle homogeneous polynomials with numerical coefficients. Hence, it was modified by the author of this dissertation to accommodate Fourier series as coefficients.

The implementation of the software to generate the reduction to the center manifold was a three step process. The first step was to compute a periodic orbit. The second was to compute the Floquet transformation, and the last one the expansion of the Hamiltonians, complexification and realification steps, and the Lie transform algorithm. The output of the first program is the input for the second one, and the output of the second one is the input for the third one. The output of the third one contains the coefficients of the center manifold. In Appendix C there is sample of the input file used to compute the Floquet transformation, and in Appendix D the output of this process which is also the input for the next step, the Lie transform that leads reduction of the center manifold.

Once the reduction to the center manifold is computed, we need to ensure that the algorithm was properly coded. To test the software, we follow the same approach described in [Jorba, 1999]. The idea is the following: we chose a point in the center manifold with coordinates u_0 close to the origin (we recall it is also an equilibrium point), and integrate it from $t = 0$ to $t = t_f$. We call this point u_1. Then, we send u_0 and u_1 to the original coordinates by reverting all the transformations from Section 2.1.1 and Section 2.1.2. We call the points corresponding to u_0 and u_1 in the original coordinates v_0 and v_1 respectively. Now, we integrate u_0 in the original system from $t = 0$ to $t = t_f$ and we call this value v_0^1. If the change were exact, then we would have that $v_1 = v_0^1$. However, this not the case, and the value $e_1 = \|v_1 - v_0^1\|$ is an indicator of the error. Ideally, this error is a combination of numerical errors due to the floating point representation and the numerical integration,

---

[3] Available at `http://www.maia.ub.es/~angel/mac-jun2008.tgz` as of June 2020.

and of the truncation order of the center manifold approximation. The expectation is that points close to the origin have errors smaller that the those further away. Hence, the error should behave like $c\lambda_0^N$ where $\lambda_0 = \|u_0\|$ is the distance form the origin, and N is the order of the center manifold approximation.

Hence, if we repeat the process outlined in the previous paragraph for several initial conditions $u_i, i = 0, ..., m$ at increasing distances from the origin $\lambda_0^{(0)} < ... < \lambda_0^{(m)}$ then the order of the error can be approximated as:

$$N \approx \frac{\ln(\frac{e_j}{e_{j+1}})}{\ln(\frac{\lambda_0^{(j)}}{\lambda_0^{(j+1)}})}, \quad j = 1, ..., m-1. \tag{2.26}$$

The formula (2.26) establishes the criterion to decide whether or not the implementation has been properly implemented. Examples of this test are illustrated in this dissertation in Section 4.2.1 and Section 4.2.2 for the reduction to the center manifold around L_1 and L_2 points in the QBCP, respectively.

2.2 Computation of highly unstable invariant tori

The method used to compute invariant tori is based on [Castellà and Jorba, 2000]. Let us start with a differential equation

$$\dot{x} = f(x, t) \tag{2.27}$$

where $f(x, t) = f(x, t + T)$ is a T-periodic, $f \in \mathcal{C}^\omega(\mathbb{R}^n)$, and $T = 2\pi/\omega_f$.

We assume there exists a quasi-periodic orbit $x(t)$ for the Equation (2.27) with two basic frequencies $\omega_1, \omega_2 \in \mathbb{R}$ such that $\omega_1/\omega_2 \in \mathbb{R}\backslash\mathbb{Q}$. This means that there exists a map $X : \mathbb{T}^2 \to \mathbb{R}^n$ (the parametrization of the torus) such that $x(t) = X(\omega_1 t, \omega_2 t)$.

Note that one of the frequencies is known, and it is inherited from the vector field. This frequency is equal to ω_f. Hence, from now on we will assume that $\omega_2 = \omega_f$. Now, let us define the stroboscopic map F as the flow ϕ associated to the Equation (2.27) at time $T = 2\pi/\omega_f$. Note that now the closed curve $\theta \in \mathbb{T} \mapsto X(\theta, 0) \in \mathbb{R}^n$ is invariant by F,

$$F(X(\theta, 0)) = X(\theta + \omega_1 T, \omega_f T) = X(\theta + 2\pi\frac{\omega_1}{\omega_f}, 2\pi) = X(\theta + 2\pi\frac{\omega_1}{\omega_f}, 0).$$

Setting $\rho = 2\pi\frac{\omega_1}{\omega_f}$ and denoting $X(\theta, 0) \equiv X(\theta)$ the previous invariance equation reads,

$$X(\theta + \rho) = F(X(\theta)). \tag{2.28}$$

Thus, knowing that one of the fundamental frequencies of the motion is ω_f, the problem of computing a torus is reduced to finding a function $\hat{X} : \mathbb{T}^1 \to \mathbb{R}^n$ that satisfies Equation (2.28) for a given ρ (note that to know ρ is equivalent to know ω_1). Such function $\hat{X}$ is called an *invariant curve* with *rotation number* ρ. Obviously, if $\hat{X}$ is an invariant curve with rotation number ρ, it satisfies that

$$G(\hat{X}(\theta)) = F(\hat{X}(\theta)) - \hat{X}(\theta + \rho) \equiv 0. \tag{2.29}$$

From a practical point of view, the approach is to find a zero of G. A convenient way to approximate an invariant curve is to use its (truncated) Fourier series,

$$X(\theta) = a_0 + \sum_{k=1}^{N} a_k \cos(k\theta) + b_k \sin(k\theta) \quad a_i, b_i \in \mathbb{R}^n. \tag{2.30}$$

Hence, the goal is to compute the Fourier coefficients $a_i, b_i, i = 0, ..., N$ such that they define a periodic function X which is a zero of (2.29). This leads to $(2N+1)n$ unknowns. Hence, at least the same number of equations is required to solve for all $a_i, b_i, i = 0, ..., N$. To this end, (2.29) is discretized by using an equispaced grid of values of θ such that

$$\theta_j = \frac{2\pi j}{2N+1}, \quad j = 0, ..., 2N. \tag{2.31}$$

This provides the number of equations needed to solve for the Fourier coefficients $a_i, b_i, i = 0, ..., N$. Finally, an extra equation specifying a value for the Fourier coefficients at $\theta = 0$ is required to resolve the ambiguity in the Fourier coefficients due to the fact that the map F is autonomous (see [Castellà and Jorba, 2000] for further details). This system of equations is solved by means of a standard Newton's method using least squares to account for the fact that we have more equations than unknowns.

In the models used in this thesis, we often encounter highly unstable dynamics. In this scenarios the use of multiple shooting is required to mitigate the error growth due to the instability of the region of interest (see [Duarte, 2020] for a discussion for the Sun-Jupiter $L_{1,2}$). The following paragraphs illustrate how this is approached. Let us start with the following definition.

Definition 1. *Let $g_1, \ldots, g_r$ diffeomorphisms of some subset of $\mathbb{R}^n$ into itself, let x be the parametric representation of a closed curve of $\mathbb{R}^n$, $\theta \in \mathbb{T}$ and let $\rho \in \mathbb{T}$. Then, x is called an* ***r-invariant*** *curve for $g_1, \ldots, g_r$ with rotation number ρ if*

$$(g_r \circ \overset{r}{\cdots} \circ g_1)(x(\theta)) = x(\theta + \rho) \quad \forall \theta \in \mathbb{T}$$

Remark 1. *It is easy to check that if x is an r-invariant curve then, for any $\alpha \in \mathbb{R}$, $x(\theta + \alpha)$ is also a r-invariant curve. This means that there are different sets of Fourier coefficients representing the same r-invariant curve.*

Given a r-invariant curve x_0 approximated by a truncated Fourier series (2.30), the goal is to compute its $(2N+1)n$ coefficients $a_i, b_i, i = 0, ..., N$. The invariance condition for a r-invariant curve reads

$$\begin{aligned} x_1(\theta) &= g_1(x_0(\theta)), \\ &\vdots \\ x_{r-1}(\theta) &= g_{r-1}(x_{r-2}(\theta)), \\ x_0(\theta + \rho) &= g_r(x_{r-1}(\theta)). \end{aligned} \tag{2.32}$$

As a result, to find x_0, it is also required to solve for $x_i, i = 1, ..., r-1$. This is, there are a total of $(2N+1)nr$ unknowns corresponding to all the r-invariant curves. Now, we use the grid (2.31) to discretized each of the equations in (2.32), and the following set of equations is obtained,

$$G_r(x_0(\theta), ..., x_{r-1}(\theta)) = \begin{bmatrix} g_1(x_0(\theta_0)) - x_1(\theta_0) \\ \cdots \\ g_1(x_0(\theta_{2N})) - x_1(\theta_{2N}) \\ \vdots \\ g_r(x_{r-1}(\theta_0)) - x_0(\theta_0 + \rho) \\ \cdots \\ g_r(x_{r-1}(\theta_{2N})) - x_0(\theta_{2N} + \rho) \end{bmatrix} = 0. \tag{2.33}$$

An extra equation specifying, for instance, a value of a coordinate at $\theta = 0$ is required to resolve the ambiguity in the Fourier coefficients (see Remark 1). The system of equations (2.33) is solved by means of a standard iterative Newton's method using least squares to account for the extra equation. The iteration process is stopped when the norm of the function becomes smaller than a prescribed tolerance (typically, a value of the order of 10^{-6} is good enough for plots, but for the computation of the stability we have used 10^{-10}). Note that this method ends up computing r curves.

This parallel shooting approach is useful to compute invariant curves for very unstable systems. (This is, for example, the L_2 region in the BCP or the QBCP). The maps g_j, $j = 1, \ldots, r$ are defined as follows: if p denotes a point in the phase space, then

$$g_j(p) = \phi\left(p;\ (j-1)\frac{T}{r},\ j\frac{T}{r}\right), \quad j = 1, \ldots, r,$$

where $\phi(p; t_1, t_2)$ denotes the flow from time t_1 to time t_2, and we recall that T is the period defined in Equation 2.27. In this thesis, we used $r = 4$.

Note that the convergence of the Newton's method does not guarantee that the solution is a good representation of the torus. Remember that we have computed the torus based upon a truncated Fourier series (2.30). To estimate the error of the actual representation, the invariance condition is checked on a finer mesh. If the error in the verification of this condition is larger than a prescribed threshold, then more Fourier coefficients are added in the representation (2.30), and the process starts again from the last computed solution.

2.2.1 Initial condition and continuation of invariant tori

As mentioned at the beginning of this section, obtaining a first invariant curve is one of the main challenges. We will use as starting point for a family of invariant tori a periodic orbit which in the Poincaré map is a fixed point of center×saddle type. In our case, we are interested in the family born from the elliptical direction of the Poincaré map's fixed point. Hence, we can use as first approximation the linearization of the Poincaré section around this fixed point. The initial frequency of this invariant curve is set to be $\rho = \omega_L + \Delta\rho$, where ω_L is the frequency of one the elliptic directions of the periodic orbit and $\Delta\rho$ is a small increment. The sign of $\Delta\rho$ is positive or negative depending on whether the frequency increases or decreases when moving away from the periodic orbit along the selected elliptic direction. Then, with this initial approximation, the Newton method is applied as described in the previous section.

Hence, for now on, let us assume that a torus as expressed in (2.30) is known. The strategy employed here to continue a family of tori is to parametrize the family with respect to the rotation number. To find a new torus of the family the rotation number is slightly increased (or decreased, depending on which direction the family wants to be continued) as it was done to find the first torus, and then the Newton method is applied to solve for the new torus as described in the previous section. In this sense, by modifying the rotation number we are using the current torus a seed for the Newton process. This is done until three tori are computed. After the third torus, the initial condition for the next tori of the family and the rotation number are obtained by interpolating the coefficients and the rotation numbers of the previous three tori, and extrapolating them to the new one by an increment ds. This provides a good enough initial guess to find the torus in a few iterations of the Newton method.

This particular implementation of the method does not consider the rotation number as a variable, and as such it is not estimated during the Newton process. This was implemented, and no significant benefit was identified. In order to keep the number of iterations low, the extrapolation step ds needs to be adjustable. The strategy followed is to double the extrapolation step if the number of iterations is less than 6, and divide it by two if it is greater.

2.3 Computation of the linear stability for invariant tori

The stability of an invariant object is as important as the invariant object itself. The methods in this section are based on the results in [Jorba, 2001], that here we have adapted to a multiple shooting scheme. The following paragraphs provide an overview of the method to compute the stability of invariant curves, and the modification to work with unstable systems.

Let us assume that x is an invariant curve satisfying condition (2.28). To study the dynamical behavior close to the curve, we consider a small displacement $h \in \mathbb{R}^n$ with respect to x. Then,

$$F(x(\theta) + h) = F(x(\theta)) + D_x F(x(\theta))h + \mathcal{O}(\|h\|^2).$$

Hence, using that $F(x(\theta)) = x(\theta + \rho)$ and discarding the second order term, we have that the following dynamical system describes the linear normal behavior around the invariant curve,

$$\begin{aligned} \bar{h} &= A(\theta)h, \\ \bar{\theta} &= \theta + \rho, \end{aligned} \tag{2.34}$$

where $A(\theta) = D_x F(x(\theta))$ and $h \in \mathbb{R}^n$. Let $C(\mathbb{T}^1, \mathbb{C}^n)$ be the set of continuous functions between $\mathbb{T}^1$ and $\mathbb{C}^n$. If $\psi \in C(\mathbb{T}^1, \mathbb{R}^n)$, we define the operator $T_\rho : C(\mathbb{T}^1, \mathbb{C}^n) \to C(\mathbb{T}^1, \mathbb{C}^n)$ as $T_\rho(\psi(\theta)) = \psi(\theta + \rho)$, $\theta \in [0, 2\pi)$. In [Jorba, 2001] it is shown that:

- The stability analysis of an invariant curve of (2.28) is reduced to the following generalized eigenvalue problem,

$$A(\theta)\psi(\theta) = \lambda T_\rho(\psi(\theta)), \quad \lambda \in \mathbb{C}. \tag{2.35}$$

- If the Poincaré map is autonomous, then 1 is an eigenvalue of (2.35) with eigenfunction x', where x denotes the invariant curve and $'$ the differentiation with respect to θ.
- Eigenvalues with norm 1 correspond to elliptic directions, an eigenvalues with norm different from 1 correspond to hyperbolic directions.

From a practical point of view, the goal is to solve a discrete version of (2.35). Details about how to deal with this problem numerically can be found in [Jorba, 2001], and will not be repeated here. In the following paragraphs we focus on how to adapt these methods to a multiple shooting scheme.

Let us assume that we have computed a r-invariant curve using a multiple shooting scheme with r sections, and that we want to know its stability. Using the same argument as before to construct the linearized dynamical system (2.34) and the generalized eigenvalue problem (2.35), the stability of the r-invariant curves is reduced to the analysis of the following generalized eigenvalue problem:

$$\underbrace{\begin{bmatrix} Dg_1 & 0 & \cdots & 0 & 0 \\ 0 & Dg_2 & \cdots & 0 & 0 \\ \vdots & \vdots & \ddots & \vdots & \vdots \\ 0 & 0 & \cdots & Dg_{r-1} & 0 \\ 0 & 0 & \cdots & 0 & Dg_r \end{bmatrix}}_{\mathcal{A}} \underbrace{\begin{bmatrix} \psi_1(\theta) \\ \psi_2(\theta) \\ \vdots \\ \psi_{r-1}(\theta) \\ \psi_r(\theta) \end{bmatrix}}_{\Psi(\theta)} = \lambda \underbrace{\begin{bmatrix} 0 & I & 0 & \cdots & 0 & 0 \\ 0 & 0 & I & \cdots & 0 & 0 \\ \vdots & \vdots & & \ddots & \vdots & \\ 0 & 0 & 0 & \cdots & 0 & I \\ T_\rho & 0 & 0 & \cdots & 0 & 0 \end{bmatrix}}_{\mathcal{B}} \underbrace{\begin{bmatrix} \psi_1(\theta) \\ \psi_2(\theta) \\ \vdots \\ \psi_{r-1}(\theta) \\ \psi_r(\theta) \end{bmatrix}}_{\Psi(\theta)}$$

where $g_k = g(x_k(\theta)), k = 1, ..., r$, Dg_k is the differential evaluated on $x(\theta)$ and T_ρ denotes the operator $T_\rho : \psi(\theta) \mapsto \psi(\theta + \rho)$. In a more compact way, this eigenvalue problem can be expressed as

$$\mathcal{A}\Psi(\theta) = \lambda \mathcal{B}\Psi(\theta). \tag{2.36}$$

This generalized eigenvalue problem is solved identically as the case $r = 1$. The comments in [Jorba, 2001] apply also this formulation of the problem.

Note that in a simple shooting technique we compute the invariant curve for the map $g_r \circ \cdots \circ g_1$. In the same way, the stability for a single shooting invariant curve is given by the eigenvalue problem

$$(Dg_r \circ \cdots \circ Dg_1)\psi(\theta) = \lambda \psi(\theta + \rho). \tag{2.37}$$

The relation between the eigenvalues obtained when using single shooting with the ones obtained with parallel shooting is given by the next proposition.

Proposition 2. *If* λ *and* $\Psi = (\psi_1, \ldots, \psi_r)$ *are an eigenvalue and its associated eigenfunction of (2.36), then* λ^r *and* ψ_1 *are an eigenvalue and its associated eigenfunction of (2.37).*

Proof.

$$\begin{aligned}(Dg_r \circ \cdots \circ Dg_1)(\psi_1(\theta)) &= (Dg_r \circ \cdots \circ Dg_2)(\lambda_1 \psi_2(\theta)) = (Dg_r \circ \cdots \circ Dg_3)(\lambda_1^2 \psi_3(\theta)) \\ &= \cdots = Dg_r(\lambda_1^{r-1}\psi_{r-1}(\theta)) = \lambda_1^r T_\rho(\psi_1(\theta)) = \lambda_1^r \psi_1(\theta + \rho).\end{aligned}$$

□

2.4 Computation of invariant manifolds

In the context of this section we are interested in the invariant manifolds associated to the hyperbolic part of an invariant torus. For each saddle part of an invariant torus there are two invariant manifolds: the stable manifold, and the unstable manifold. The goal is to obtain numerical approximations of these invariant manifolds. In order to compute these approximations we need two ingredients: the eigenvalues of a hyperbolic component (λ_u, λ_s) and its associated eigenfunctions $(\psi_u(\theta), \psi_s(\theta))$. The subscripts denote the unstable (u) and stable (s) component. (Note that in the case of a Hamiltonian system, $\lambda_u = \lambda_s^{-1}$.) The reader is referred to Section 2.3 for the details on how to compute the eigenvalues and their associated eigenfunctions.

Let us assume that x is an invariant curve satisfying the condition given by Equation (2.28). Let us also assume that there is an eigenvalue λ_u (resp. λ_s) associated to the unstable (resp. stable) components of the hyperbolic part of an invariant curve $x(\theta)$ parametrized by an angle $\theta \in [0, 2\pi)$. Next, we pick a $h_0 \in \mathbb{R}$, and construct a linear approximation of the invariant manifold as follows:

$$p_*(\theta, h_0) = x(\theta) + h_0 \psi_*(\theta), \quad * = u, s. \tag{2.38}$$

In order for (2.38) to be a good enough approximation of the invariant manifold, h_0 is chosen such that

$$\|F(p_*(\theta, h)) - p_*(\theta + \rho, h) - h\lambda_* \psi_*(\theta + \rho)\| < \delta, \quad * = u, s \tag{2.39}$$

where F is the diffeomorphism from Equation (2.28), ρ is the rotation number of the invariant curve, and $\delta > 0$ is small (typically of the order of 10^{-6}). Let us also assume that Equation(2.39) holds for $\forall \theta \in [0, 2\pi)$.

Now, following the ideas of [Simó, 1990], and focusing on the unstable manifold to simplify the notation, we choose $(\theta, h) \in [0, 2\pi) \times [h_0, h_0\lambda_u]$ and construct the linear approximation of the invariant manifold $(\theta, h) \to p(\theta, h) = x(\theta) + h\psi_u(\theta)$. The set $[0, 2\pi) \times [h_0, h_0\lambda_u]$ defines the so-called *fundamental cylinder.* At this point, we iterate the linear approximations $p(\theta, h)$ by the diffeomorphism F to obtain a big part of the unstable manifold. Note that when constructing the linear approximation of the invariant manifold, we could have chosen to do

$(\theta, h) \to p(\theta, h) = x(\theta) - h\psi_u(\theta)$ and repeat the process. Changing this sign is how we get both "sides" of the manifold.

From a practical point of view, we proceed as follows: we set a tolerance $\delta > 0$, and a create a grid of N points in the interval $[0, 2\pi)$ such that $\theta_i = 2\pi i/N, i = 0, ..., N-1$. Then, we pick a value h_0 that meets Equation (2.39) for all $\theta_i, i = 0, ..., N-1$. With this value h_0, we construct the interval $[h_0, h_0\lambda_u]$ and create a grid of M points $h_j \in [h_0, h_0\lambda_u], j = 0, ..., M-1$. Hence, we have total of $N \times M$ points in the fundamental cylinder $[0, 2\pi) \times [h_0, h_0\lambda_u]$ that we use to generate linear approximations $(\theta_i, h_j) \to p(\theta_i, h_j) = x(\theta_i) \pm h_j\psi_u(\theta_i)$ of the invariant manifold (the sign depends on which "side" of the manifold we want to generate). Then, each on of these points $p(\theta_i, h_j)$ are iterated by the diffeomorphism F. Finally, note that the process can be implemented also in a parallel shooting scheme (see [Duarte, 2020] for details).

Chapter 3

Contributions to the Bicircular Problem

This chapter provides some insight on the dynamics in a vicinity of the L_2 point in the BCP. This is accomplished by computing families of 2D invariant tori. The analysis focuses on tori that are Halo-like, as they are potentially interesting for space missions. This chapter is structured as follows: Section 3.1 studies the transition of the L_2 point in the RTBP to the BCP. Section 3.2 explains unsuccessful attempts to study the vicinity of the L_2 region using normal forms. Next, Section 3.3 computes several families of 2D invariant tori in an attempt to explain how these objects are organized, their stability, and their connection to the RTBP. As mentioned, the focus is on the Halo-like families of invariant tori, and these are studied in Section 3.4. Finally, Section 3.5 explains some of the practical applications these orbits may have for potential space missions.

3.1 From RTBP to BCP: the L_2 point case

It is well known that L_2 is an equilibrium point of the RTBP. However, as opposed to the RTBP, the BCP is not an autonomous system, and it depends periodically on time. Thus, the L_2 point is not an equilibrium point anymore. In a general setting (not necessarily Hamiltonian), if a periodic perturbation is applied to a differential equation then, under generic conditions of non-degeneracy, an equilibrium point becomes a periodic orbit with the same period of the perturbation. Applying this principle, in this section we explain what are the dynamical consequences that the time-periodic perturbation has on the L_2 point in the context of the BCP.

The approach taken to study the transition of the L_2 point from the RTBP to the BCP is by continuation with respect to the mass of the Sun. To that effect, we define the following family of Hamiltonians,

$$H^{\varepsilon} = H_{RTBP} + \varepsilon H_S, \tag{3.1}$$

with $\varepsilon \in [0, 1]$. Note that for $\varepsilon = 0$, $H^0 = H_{RTBP}$, and for $\varepsilon = 1$, $H^1 = H_{BCP}$. Considering

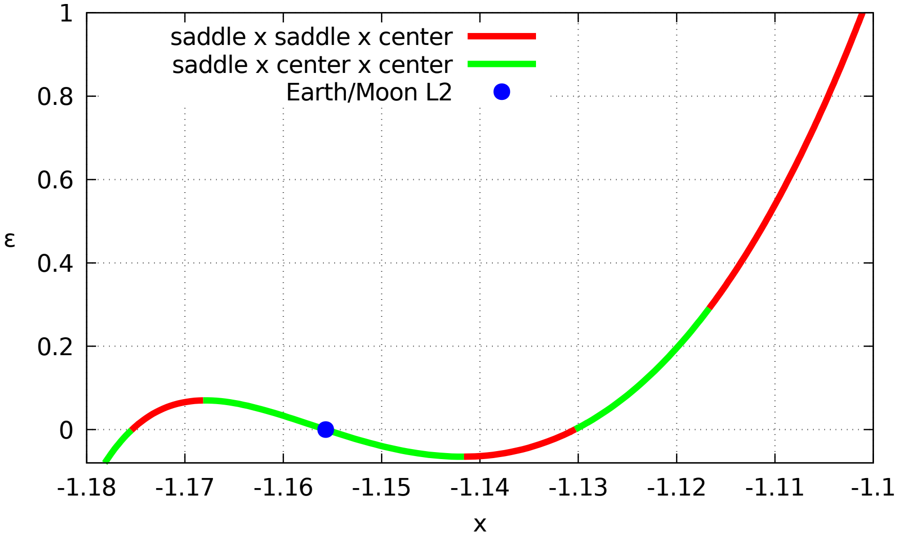

Figure 3.1: Stability type of the periodic orbits as a function of ε starting at E/M L_2

$\varepsilon = 0$, the five Lagrange points ($L_i, i = 1, ..., 5$) are equilibrium points of the system (3.1). When $|\varepsilon|$ is small enough, the equilibrium points become periodic orbits around the point L_i (now defined only geometrically since they are no longer equilibrium points) with the same period of the perturbation. In our case, the period is equal to the period of the Sun, $T_S = 2\pi/\omega_S$. However, the perturbation that defines the BCP cannot be considered small. For example, around the triangular points L_4 and L_5 there is a loss of uniqueness of the periodic orbit, and three periodic orbits appear (see [Gómez et al., 1987, Simó et al., 1995]). The size of the perturbation also affects the L_2 point.

Besides showing the existence of these periodic orbits, computing their stability is essential to have the full picture. By means of analyzing the spectra of the monodromy matrix, we also can see how the linear stability of these new periodic orbits evolves with respect to the continuation parameter ε. It is important to note that due to the highly unstable nature of the L_2 region, the algorithm to compute periodic orbits had to be implemented using a multiple shooting scheme. This is a pretty standard procedure (see [Stoer and Bulirsch, 2002, Seydel, 2009]) and the details can be found, for instance, in [Gómez and Mondelo, 2001] for the RTBP. For the present work, the total number of sections used was four.

The results of continuing the L_2 point with respect to the mass of the Sun are shown in Figure 3.1. The horizontal axis is the x component of the periodic orbit at $\theta = 0$, and the vertical axis is the continuation parameter ε applied to the mass of the Sun. Starting form L_2, and moving to the left the parameter increases until it hits a local maximum, and then decreases to cross the horizontal line and become negative. The point on the horizontal axis corresponds to a 1:2 resonant planar Lyapunov orbit (the frequency of the orbit is twice the frequency of the Sun). Moving from L_2 to the right, the continuation parameter becomes negative, decreasing until it hits a local minimum, and then increases to cross the horizontal line and reach the BCP ($\varepsilon = 1$). Again, in this case the continuation also crosses the horizontal axis. This corresponds to the same 1:2 resonant planar Lyapunov orbit. The main takeaway is that there is no natural dynamical substitute of the L_2 point in the BCP because there is no direct connection between it and a periodic orbit in the BCP. The periodic orbit around L_2 in the BCP is pictured in Figure 3.2. The L_2 point and the Moon are added for reference.

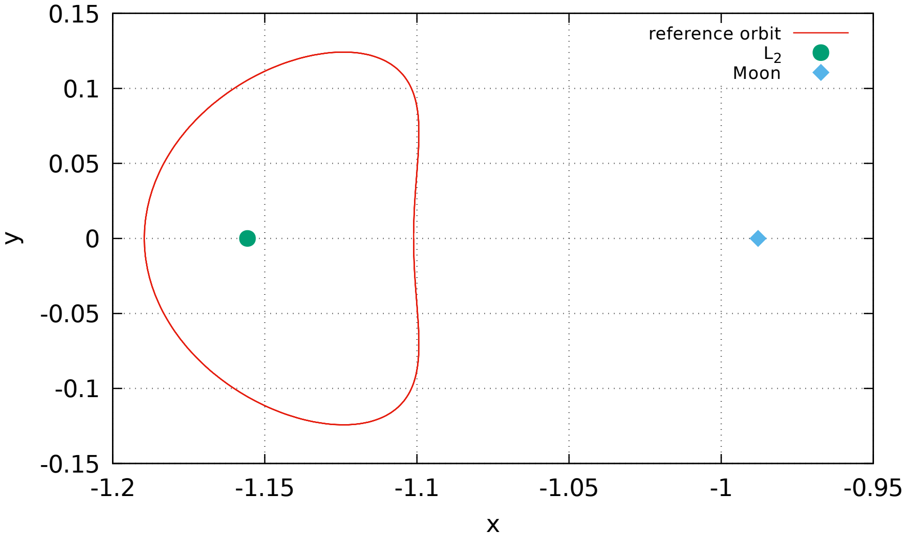

Figure 3.2: Periodic orbit near L_2 in the BCP. (Note: In the figure is not perceived, but the periodic orbit revolves around the L_2 twice in one period.)

Figure 3.1 also contains the details on the linear stability of the periodic orbits computed. As a technical remark, for the computation of the eigenvalues of the monodromy matrix, the approach described in [Gonzalez and Mireles James, 2016] was used to account for the fact that multiple section were used. It is observed that the periodic orbits alternate between the types saddle × center × center (green regions) and saddle × saddle × center (red regions). Starting from L_2, the linear stability is of the type saddle×center×center. Moving to the left, ε increases and the periodic orbits keep this linear stability type until they hit the local maximum. In this turning point, the linear stability becomes of the type saddle × saddle × center until another bifurcation point at resonant 1:2 planar Lyapunov ($\varepsilon = 0$). At this point, ε becomes negative, and the resulting periodic orbits are of the type saddle × center × center. A similar pattern but with different sign for ε is observed when moving to the right of the L_2 point. In this scenario, ε decreases and maintains the same linear stability type as L_2 until they hit a local minimum. As before, in this turning point, the linear stability becomes of the type saddle × saddle × center until $\varepsilon = 0$, where there is yet another bifurcation. At this bifurcation, the linear stability becomes of the type saddle × center × center. Finally, this resonant planar Lyapunov orbit is continued until the last bifurcation point. This is a pitchfork bifurcation, and it is where the 1:2 resonant (with the Sun) Halo orbit in the RTBP ends (see [Andreu, 1998] for the details). The implication is that the 1:2 resonant Halo orbit in the RTBP does not reach the BCP. As we will see in Section 3.3, this is not the case for all Halo orbits, and there is a dense set of Halo orbits that survive the perturbation of the Sun as modeled in the BCP.

After this point, the stability of the periodic orbits is of the type saddle × saddle × center until $\varepsilon = 1$. The eigenvalues $\lambda_i, i = 1, \dots 6$ of the monodromy matrix associated to the periodic orbit in the BCP are captured in Table 3.1.

As final remark, it is important to note that the nature of the perturbation shapes the dynamics around an equilibrium point. The comparison between the BCP and QBCP illustrates this phenomena. In the QBCP the L_2 is replaced by a periodic orbit that is small in the sense that its maximal distance to L_2 is of the order of 10^{-6}, and it has the same stability type of the L_2 point. See Section 4.1 and references therein for the details.

Table 3.1: Eigenvalues of the monodromy matrix related to the periodic orbit displayed in Figure 3.2. Due to the Hamiltonian nature of the system, the other three eigenvalues are $\lambda_i^{-1}, i = 1, 2, 3$. Also, note that due to the non-autonomous character of the BCP Hamiltonian, there is no double eigenvalue 1.

	$\mathrm{Re}(\lambda_i)$	$\mathrm{Im}(\lambda_i)$
λ_1	`776607.10464907716`	`0.0000000000000000`
λ_2	`1.6602116402354583`	`0.0000000000000000`
λ_3	`0.8656940044785918`	`-0.5005735616368709`

3.2 Normal Forms around L_2 in the BCP

This section explanis our attempts to described the dynamic around the L_2 point using normal forms. This analysis is done by using a reference orbit around the L_2 described in Section 3.1. In this section, this orbit will be referred as BCP-L2.

The orbit BCP-L2 we use to analyze the dynamics has linear stability type of saddle × saddle × center. Also, the hyberbolic component in the X-Y plane is very unstable (the associated eigenvalue of the monodromy matrix of the order of 10^6 – see Table 3.1), while the vertical hyberbolic component is pretty mild. Hence, following the approach described in Section 2.1, the first step is to try to decouple the strong hyperbolic component from the mild one and the center. This is not strictly speaking a center manifold, because we are not fully decoupling the two saddles from the center. As a result of this process, an autonomous (up to certain order) series was obtained. The coefficients of the resulting Hamiltonian are shown in Table 3.2 up to order $N = 6$.

Table 3.2: Hamiltonian reduced to the central manifold up to order 6 around BCP-L2

k_1	k_2	k_3	k_4	$a_{(k_1,k_2,k_3,k_4)}$
1	1	0	0	7.4647418100552E-02
0	0	2	0	8.8659738237613E-01
0	0	0	2	8.8659738237602E-01
2	0	1	0	3.7760143086280E-01
1	1	1	0	1.6630597289072E-01
0	2	1	0	3.7760143086632E-01
0	0	3	0	-9.2456560308013E-02
2	0	0	1	-1.1191304494214E-01
0	2	0	1	1.1191304495102E-01
0	0	1	2	1.5457260750600E+00
4	0	0	0	6.7268110205505E-02
3	1	0	0	5.2689849266893E-02
2	2	0	0	1.3985654700817E-01
1	3	0	0	5.2689849172341E-02
0	4	0	0	6.7268110138079E-02
2	0	2	0	7.2390447379639E-02
1	1	2	0	-5.2729200897090E-01
0	2	2	0	7.2390447565832E-02
0	0	4	0	-2.2057631439721E-01
2	0	1	1	-9.1299556433045E-02
0	2	1	1	9.1299555440115E-02
0	0	3	1	2.3010162022048E-09
2	0	0	2	-1.4139053378602E-01
1	1	0	2	1.7092476151574E-01
0	2	0	2	-1.4139053420734E-01
0	0	2	2	3.8538005054066E+00
0	0	1	3	-3.9207365458088E-09
0	0	0	4	-4.4842459413210E-01
4	0	1	0	-8.3313326259760E-01
3	1	1	0	-3.7039263971258E-01
2	2	1	0	-1.1393123092448E+00
1	3	1	0	-3.7039263867706E-01
0	4	1	0	-8.3313326257174E-01
2	0	3	0	2.4740052484236E+00
1	1	3	0	-2.5458719006032E+00
0	2	3	0	2.4740052504929E+00
0	0	5	0	7.8082896244400E-01
4	0	0	1	5.7987801958790E-01
3	1	0	1	8.7047242680063E-01
1	3	0	1	-8.7047242941981E-01
1	1	0	3	-1.0208227319951E-08
0	2	0	3	-5.3154727601681E-01
0	0	2	3	1.7649985647984E-08
0	0	1	4	-5.0172604761653E+00
0	0	0	5	-5.2370765273109E-09
6	0	0	0	-2.7632067449907E-01
5	1	0	0	-1.7143411932578E-01
4	2	0	0	-4.0173177263249E-01
3	3	0	0	-9.8399044861280E-02
2	4	0	0	-4.0173177200605E-01
1	5	0	0	-1.7143411955834E-01
0	6	0	0	-2.7632067471742E-01
4	0	2	0	7.3894959155844E-01
3	1	2	0	1.1988480671341E+00
2	2	2	0	-9.2206439987799E-01
1	3	2	0	1.1988480762100E+00
0	4	2	0	7.3894959247106E-01
2	0	4	0	3.8292422156576E+00
1	1	4	0	-6.1363067329483E+00
0	2	4	0	3.8292422302999E+00
0	0	6	0	7.7240180500023E-01
4	0	1	1	-1.6739340186639E+00
3	1	1	1	-6.5608259032711E+00
2	2	1	1	2.2598431062275E-08
1	3	1	1	6.5608259406755E+00
0	4	1	1	1.6739340042116E+00
2	0	3	1	-1.5470776699781E+01
1	1	3	1	3.6422127462014E-08
0	2	3	1	1.5470776690794E+01
0	0	5	1	-1.2202643407845E-08
4	0	0	2	1.6193239277588E+00
3	1	0	2	2.0711362077528E+00
2	2	0	2	4.5277177310975E+00
1	3	0	2	2.0711361911695E+00
0	4	0	2	1.6193239256633E+00
2	0	2	2	-2.8747664252123E+01
1	1	2	2	3.8811158641306E+01
0	2	2	2	-2.8747664340941E+01
0	0	4	2	1.2590853986058E+01
2	0	1	3	4.9663565708623E+00

Table 3.2: (continued)

k_1	k_2	k_3	k_4	$a_{(k_1,k_2,k_3,k_4)}$	k_1	k_2	k_3	k_4	$a_{(k_1,k_2,k_3,k_4)}$
0	4	0	1	-5.7987801993719E-01	1	1	1	3	-4.0294070260698E-08
2	0	2	1	-7.8067227932717E+00	0	2	1	3	-4.9663567492903E+00
1	1	2	1	2.3525734105848E-08	0	0	3	3	1.4480437410670E-07
0	2	2	1	7.8067228088272E+00	2	0	0	4	3.9581351977473E+00
0	0	4	1	5.4809338844654E-09	1	1	0	4	-1.0144661201979E+00
2	0	1	2	-1.9517005417548E+00	0	2	0	4	3.9581352153835E+00
1	1	1	2	1.3506860244147E+01	0	0	2	4	-1.1846002221812E+01
0	2	1	2	-1.9517005536764E+00	0	0	1	5	-3.7798275171632E-07
0	0	3	2	7.7636310656921E+00	0	0	0	6	-1.3119759994992E+00
2	0	0	3	5.3154726989535E-01					

The hope was to obtain a normal form with a large enough radius of convergence to cover a large neighborhood of the periodic orbit. Unfortunately, the estimation of the radius of convergence showed that it decays very fast and is, even for low orders, small. The radius of convergence for some values of N are shown in Table 3.3. The implication of a small radius of convergence is that we could only describe the dynamics for very low levels of energy, not being able to explore the dynamics in a relevant neighborhood of the L_2 region. Hence, as summary, the technique used to describe the dynamics around L_1 (see [Jorba et al., 2020]) does not work for the L_2 region.

Table 3.3: Radius of convergence for some values of N for reduced Hamiltonian for BCP-L2

N	r_N	N	r_N
6	0.4065713311	12	0.2744176857
8	0.3527706430	14	0.2523151174
10	0.2996546480	16	0.2377118429

An alternative to overcome this issue was to use a non-autonomous normal form, and to decouple the two hyberbolic components from the center. Following the argument made in Section 2.1.2, only monomials meeting the following criteria were killed:

- The denominators $|i\omega_s j - \langle \bar{\omega}, K^1 - K^0 \rangle| > \delta_0$ for some $\delta_0 > 0$
- The exponent associated to the hyperbolic part meet the condition $k^1 = k^4$, and $k^2 = k^5$

The result of this process generated a 1.5–degrees-of-freedom Hamiltonian with a more benign radius of convergence. As mentioned before, the resulting Hamiltonian of this process was not autonomous. Thus, the estimation of the radius of convergence depended on the angle. In order to estimate the radius of convergence, this was evaluated at different angles in a fine grid between 0 and 2π, and the smallest value was picked. This gave a conservative estimation of the radius of convergence. The values obtained are summarized in Table 3.4. This this case, the threshold $\delta_0 = 0.2$ was used. Other tolerances were tested, but the presented one provided the best radius of convergence.

Table 3.4: Radius of convergence for some values of n for the non-autonomous normal form around BCP-L2

N	r_N	N	r_N
6	1.14364266	12	0.78954080
8	1.04426885	14	0.72269531
10	0.92512843	16	0.71070730

With this 1.5–degrees-of-freedom Hamiltonian, its associated vector field was integrated to generate a 2D stroboscopic map at time T_S (the period of the Sun). The results are presented in Figure 3.3.

In Figure 3.3, the origin corresponds to the periodic orbit BCP-L2 integrating a truncated expansion of $N = 6$. Surrounding the orbit BCP-L2 there is a family of 2D tori sharing one fundamental frequency with BCP-L2 (the period T_S of the perturbation) and foliating the space as the second fundamental frequency changes. The pattern observed surrounding the origin corresponds to a change in the rotation direction of the tori. No more fixed points were found, meaning that based on results presented, there are no periodic orbits of period T_S (or resonant periodic orbits) in a small vicinity of BCP-L2. This approach does not help to explain the dynamics around BCP-L2. The next section presents some results about how the dynamics are organized by computing families of 2D invariant tori.

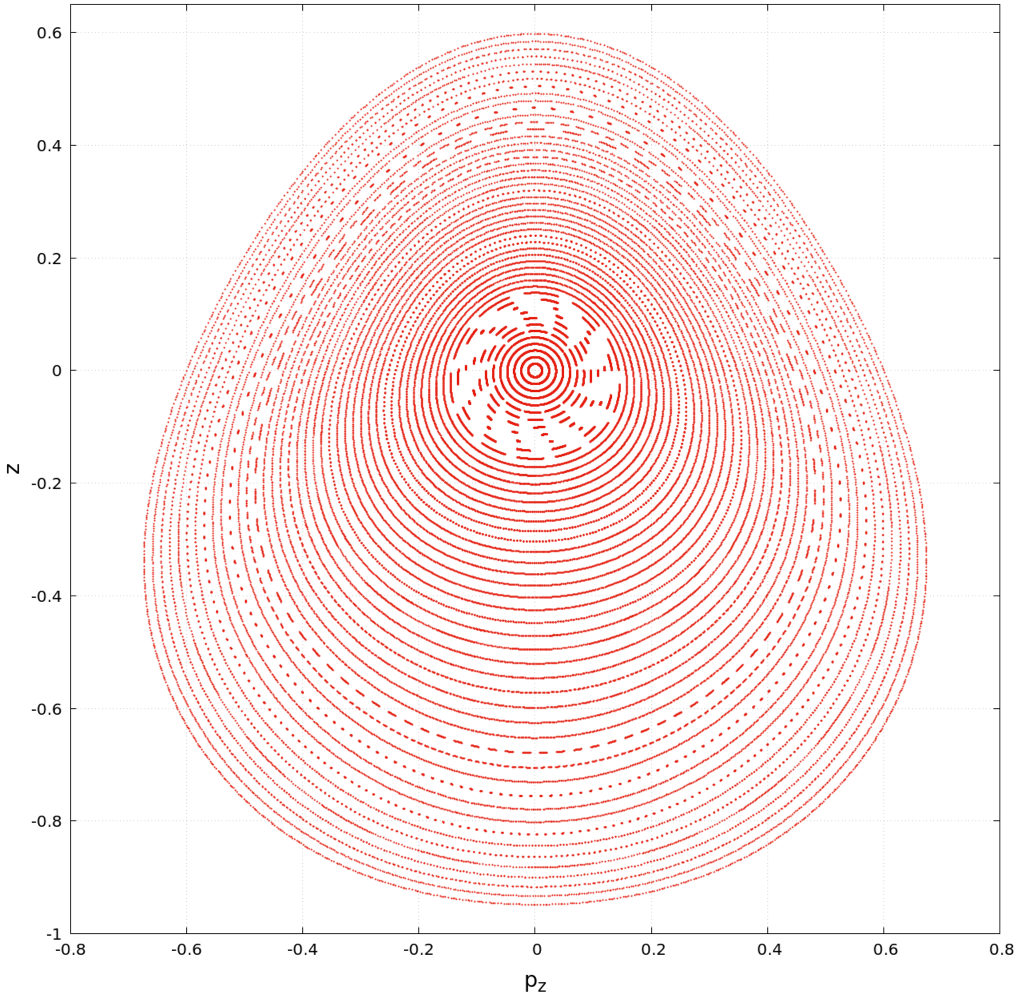

Figure 3.3: BCP-L2 orbit: stroboscopic map of the non-autonomous normal form

3.3 Families of 2D invariant tori

This section used the numerical methods to continue tori described in Section 2.2. The process of continuing tori is not absent of challenges in the BCP. Hence, we consider relevant to address the main issue found during the continuation: the sensitivity to resonances. As mentioned at the beginning of Chapter 2, the family is Cantorian. This means that it has empty interior and positive Lebesge measure ([Jorba and Villanueva, 1997]). The gaps in this family are due to resonances and, typically, they are small. Hence, the continuation process jumps over them. However, there are some instances where these gaps are too big and the continuation process has difficulties to continue. In this scenario, in order to restart the process, a new initial guess for the Newton method is required. Two strategies were employed to deal with this issue. The first strategy was to increase the stepsize of the continuation parameter and check if the process jumped over the gap. This involved some trial and error, but worked in instances were the gap was small enough. The second strategy was to stop close enough to a resonance, and then transition from the BCP to the RBTP by decreasing the mass of the Sun. Once in the RTBP, the torus is a periodic orbit that can be easily continued until it crosses the resonance, and then go back to the BCP by increasing the mass of the Sun. Sometimes it is not necessary to reach the RTBP when decreasing the mass of the Sun, it is enough to lower its mass (this reduces the size of the gap) to continue the torus through the resonance and then to increase the mass to be again in the BCP.

The result of computing and continuing families of 2D invariant tori is shown in Figure 3.4. The horizontal axis represents the x component of the corresponding invariant curve of the Poincaré map when $\theta = 0$. The vertical axis is the rotation number. Several resonances have been identified in Figure 3.4 to illustrate the argument made in Section 2.2.1 about the gaps in the family. A total of six families were found. Two of these families are planar Lypaunov-type quasi-periodic orbits (families H1 and H2 in Figure 3.4), and four have a vertical component. Out of these four, two are Halo-like quasi-periodic orbits (for the moment being, we refer to them as Halo families of Type I and Type II, see Figure 3.4) and the other two fall behind the Moon (families V1 and V2 in Figure 3.4). The next paragraphs explain how these families were found and constructed, and provide details on the two Halo-like quasi-periodic families.

The continuation process requires an initial torus. This initial torus usually is computed from a periodic orbit. In the context of the BCP two initial periodic orbits were used to find and continue families of invariant tori. The first periodic orbit is a Halo orbit in the RTBP. The approach is to pick one Halo orbit in RTBP, and then continue it with respect to the mass of the Sun until it reaches the BCP. This process had to be repeated multiple times with different Halo orbits due to the presence of gaps in the family of quasi-periodic Halo orbits. Figure 3.5 shows an example in different projections of how a Halo orbit in the RTBP becomes a quasi-periodic orbit in the BCP with two frequencies: the intrinsic one corresponding to the Halo orbit, and the one acquired due to the Sun's perturbation. The other periodic orbit used was the one found by continuing the L_2 point from the RTBP to the BCP. This orbit, described in Section 3.1, generates a family of planar quasi-periodic

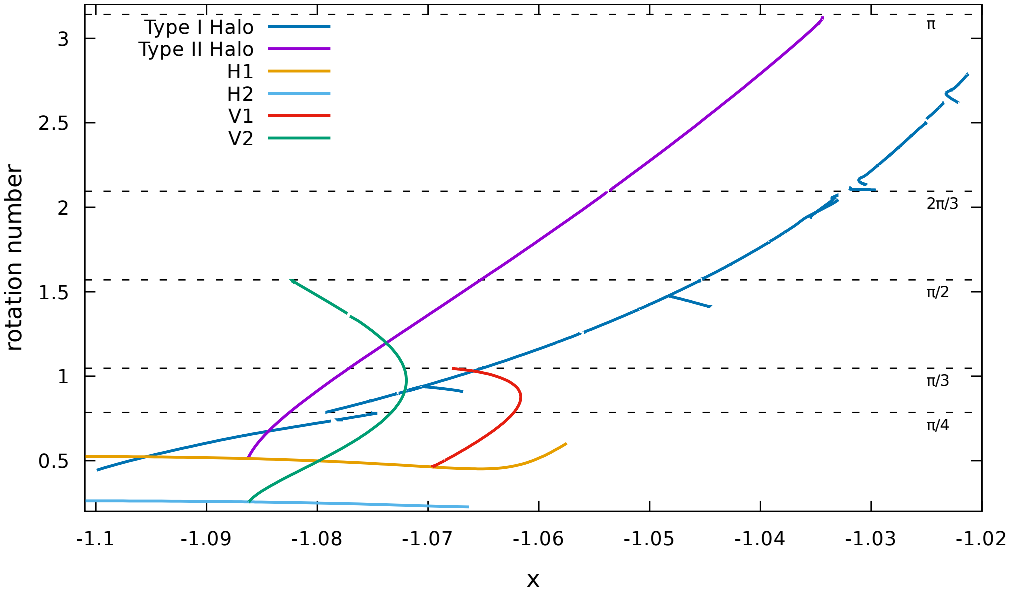

Figure 3.4: Families of invariant 2D tori in the BCP around L_2. See text for details.

orbits. This family can be considered the quasi-periodic planar Lyapunov family counterpart of the periodic ones in the RTBP (family H1 in Figure 3.4). The stability of this family was analyzed, and most of the tori are hyperbolic. There is always an eigenvalue equal to 1 with multiplicity two, plus one real eigenvalue of the order of 10^6 (and its inverse), and another pair that evolves in a way that the family undergoes two bifurcations. This is illustrated in Figure 3.6, where the last pair of eigenvalues are plotted. The horizontal axis corresponds to the x component of the invariant curve, and the vertical axis the absolute value of the eigenvalue. Figure 3.6 shows that there are two bifurcations where the absolute value of the eigenvalues is equal to one. In these cases, there are two small intervals that contain partially elliptic tori; this is, that the eigenvalues are complex with norm equal to one. These small intervals are zoomed in Figure 3.7. The top row of Figure 3.7 shows the absolute value of the eigenvalues, and the bottom row the arguments. Note that a similar phenomena appears in the RTBP, where the planar Lyapunov family undergoes a bifurcation that gives rise to the well-know family of Halo orbits. The same happens in the BCP for these two bifurcations. Each one of this families can be continued along a vertical component.

During the continuation of the V1 family, it was found that some small resonances needed to be avoided. The strategy of going back to the RTBP by decreasing the mass of the Sun, continuing the resulting object there until the resonance is passed, and going back to the BCP was employed. After returning to the BCP, it was noticed that the resulting torus did not belong to the V1 family, but to a new one labeled as V2. This torus was continued, both increasing and decreasing the rotation number. Eventually, the V2 branch met a planar

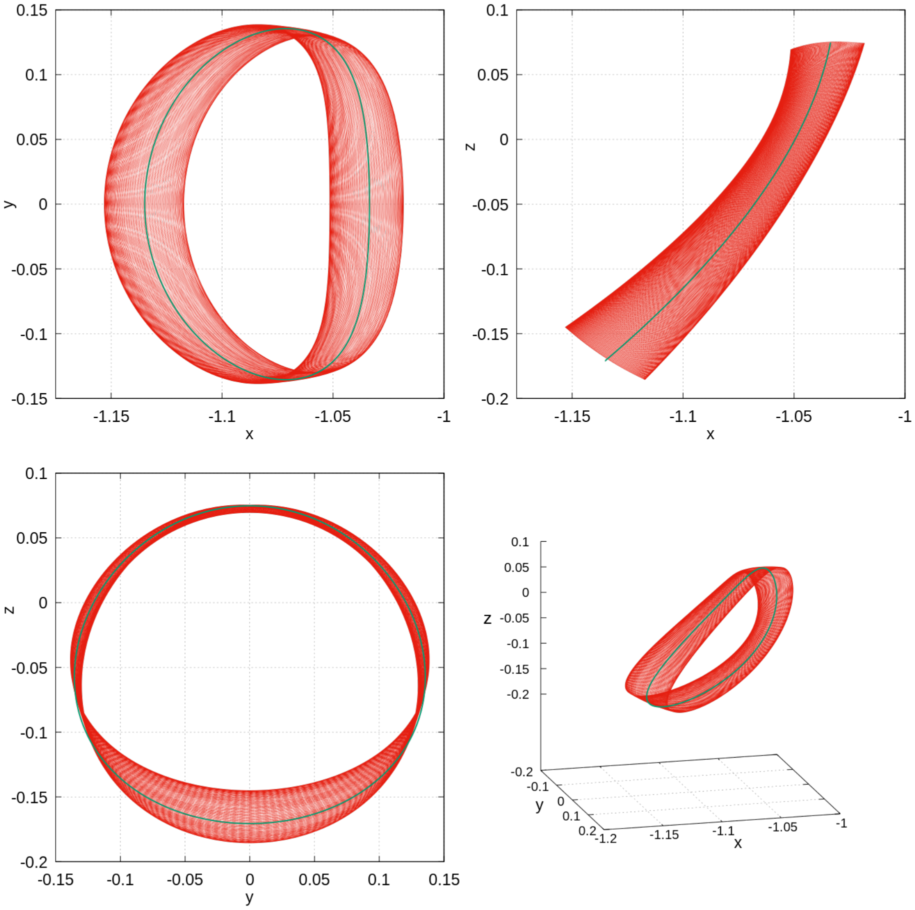

Figure 3.5: Transition from Halo orbit in the RTBP (green) to a torus in the BCP (red).

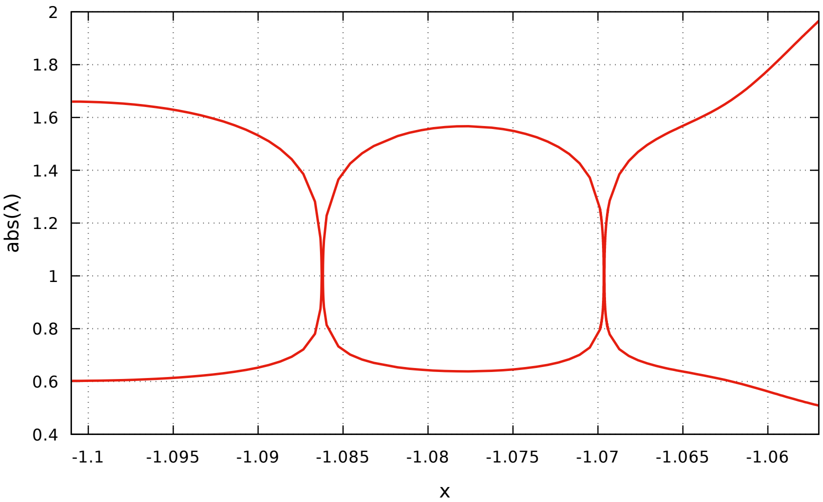

Figure 3.6: Stability of the planar quasi-periodic Lyapunov H1 family in the BCP

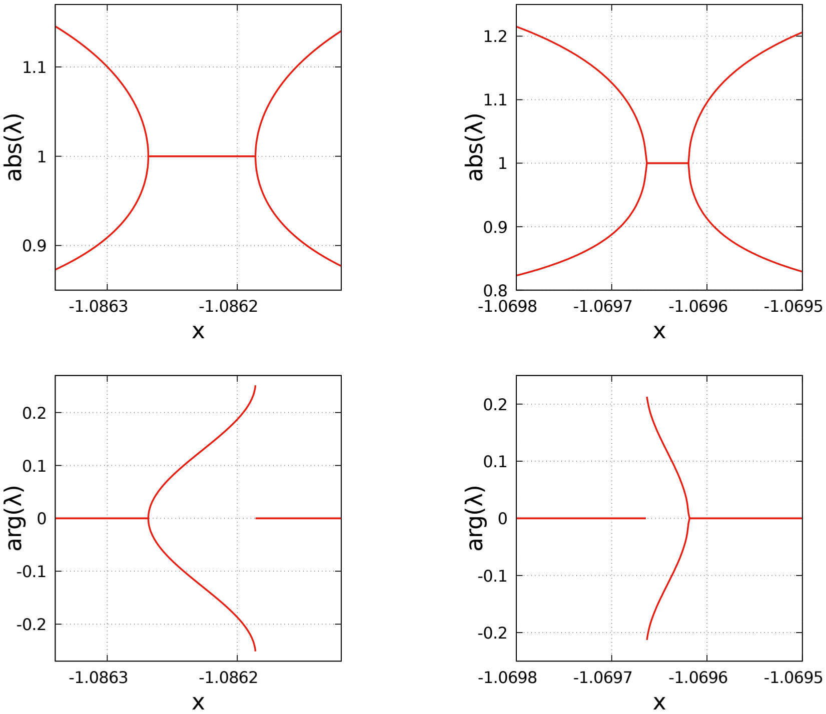

Figure 3.7: Zoom of the bifurcations in quasi-periodic Lyapunov family in the BCP

quasi-periodic Lyapunov orbit of a new family, called H2. Again, this family was continued, hence completing the picture represented in Figure 3.4. A complete study of the H and V families is left for another work, although some examples are provided in the Appendix. The next subsection elaborates on the Type I and Type II Halo-like families, the focus of this chapter.

3.4 The Type I and Type II Halo-like families

Let us begin showing some representative examples of the members of these two families. The first example of Type I Halo family is shown in Figure 3.5. The rotation number of this torus is $\rho = \texttt{1.3800185497627542}$. Another example is shown in Figure 3.8. In this case, the rotation number is $\rho = \texttt{2.6752268478193670}$. This torus is close to the resonance value of $\rho = 6\pi/7 \approx \texttt{2.6927937...}$. The effect of being close to a resonance is illustrated in Figure 3.9, a torus with rotation number $\rho = \texttt{2.6924643478193717}$. Figure 3.10 shows a torus of the Type II family. This particular example has rotation number $\rho = \texttt{3.1161371680267869}$. The projection on the $x - z$ plane shows that the orbit is a Halo-like in the sense that when observed from the Earth, the orbit circles around the L_2 point, leaving the Moon inside and hence allowing for a continuous line-of-sight between the Earth and the orbit.

Similarly to the case in the Type I Halo family, near a resonance we observe the same phenomena, and the orbit becomes more dense around the periodic orbit corresponding to that resonance. Figure 3.11 provides and example with rotation number equal to $\rho = \texttt{3.1303578715783535}$, close the resonance $\rho = \pi$.

As it has been mentioned before, the Type I family of Halo-like orbits appears when adding the Sun effect to the family of Halo orbits of the RTBP: the (non-resonant) Halo orbits add the frequency of the Sun to its own frequency and become a quasi-periodic orbit with two basic frequencies. To better understand the Type II family, we continue them by decreasing the mass of the Sun down to zero, so they are orbits of the RTBP. As an example, in Figure 3.12, up, we have plotted two RTBP orbits that come from the continuation of the Type II orbits with rotation numbers $\rho = \texttt{0.7394766853097875}$ and $\rho = \texttt{0.8587717051237963}$. Then, we have performed the reduction to the center manifold around L_2 ([Jorba, 1999, Jorba and Masdemont, 1999]). By means of the change of coordinates, we have sent initial data of each orbit to the center manifold coordinates. Then, we have plotted a Poincaré map for the level of energy of each orbit and we have marked the initial data of each orbit in the map with a big dot (with the same color used to plot the orbits). The results are shown in Figure 3.12, down. This shows that the Type II orbits come from quasi-halo orbits of the RTBP that have one of its two frequencies in resonance with the frequency of the Sun. In this way, the effect of the Sun does not add a new frequency and the quasi-halo is continued into the BCP as a quasiperiodic orbit with two basic frequencies that we refer as Type II.

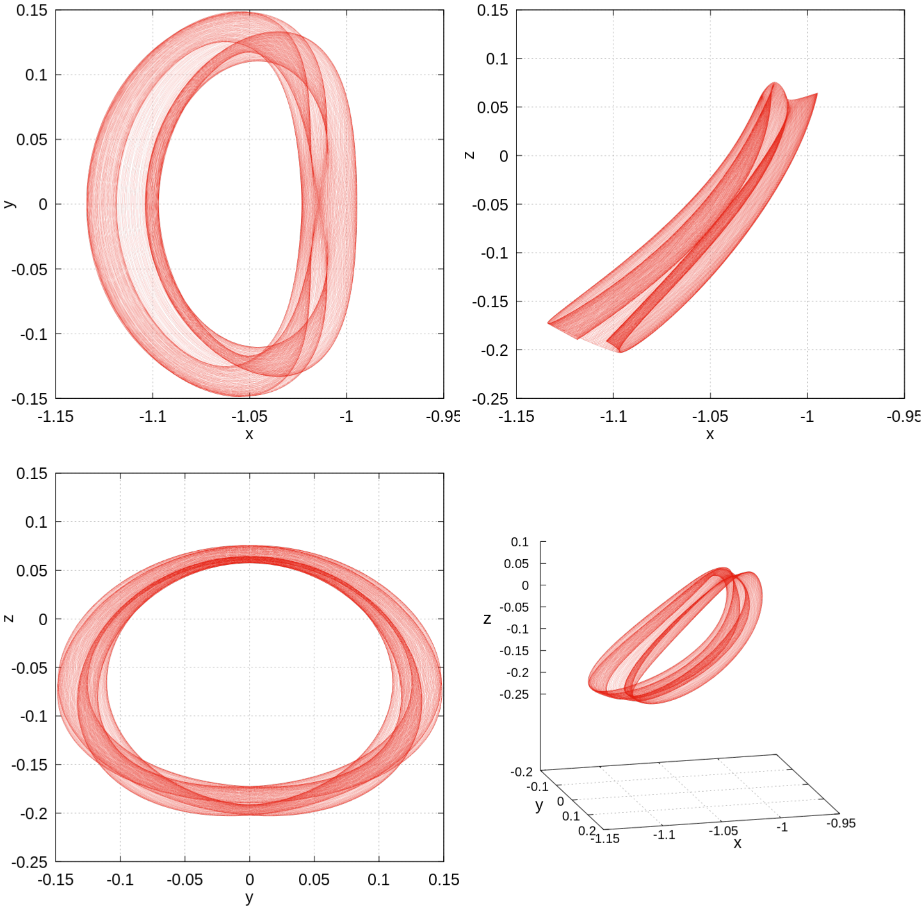

Figure 3.8: Different projections of a Type I Halo orbit.

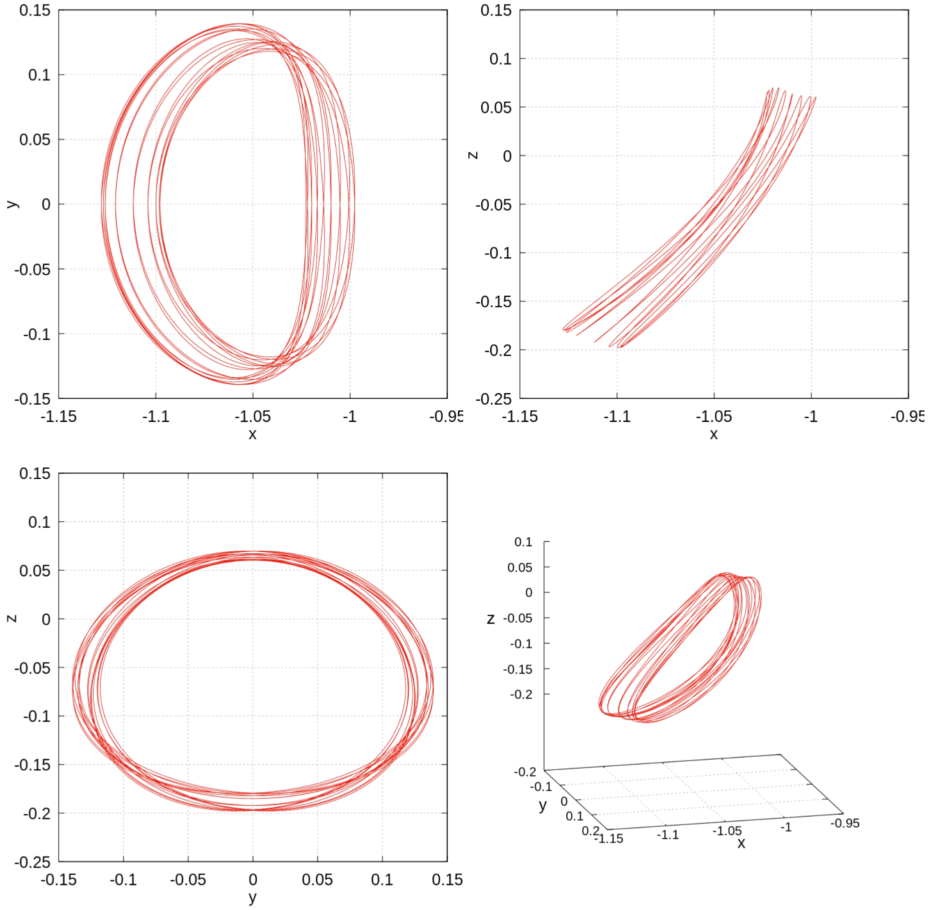

Figure 3.9: Different projections of a Type I Halo orbit near a resonance.

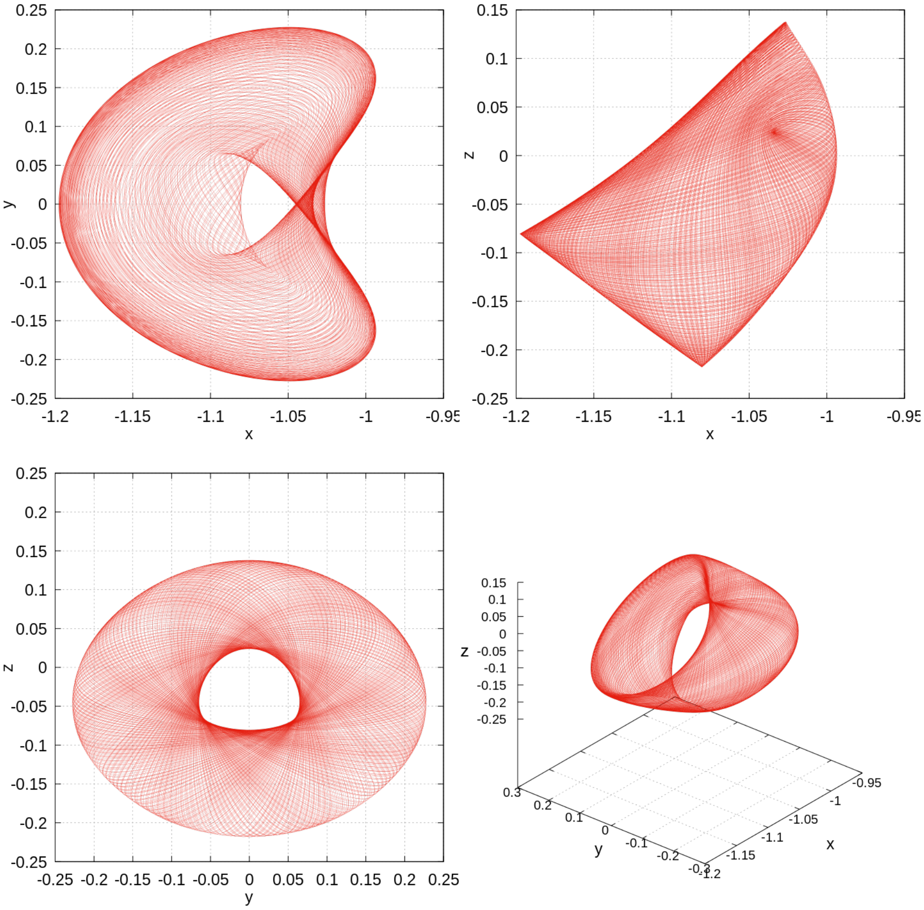

Figure 3.10: Different projections of a Type II Halo orbit.

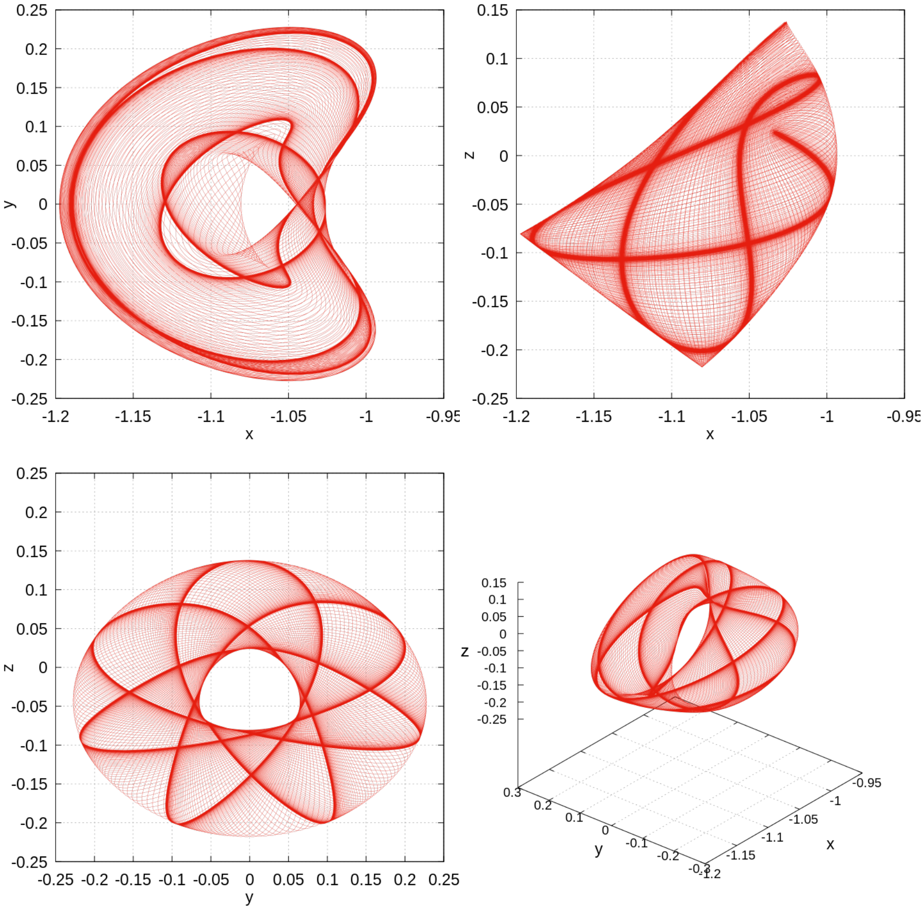

Figure 3.11: Different projections of a Type II Halo orbit near a resonance.

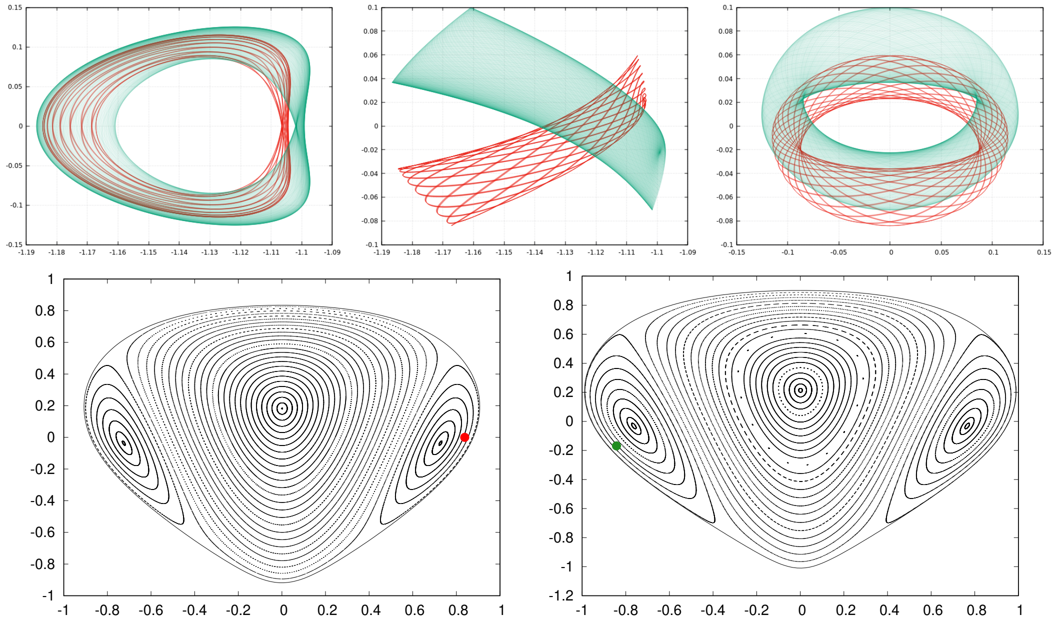

Figure 3.12: Up: (x, y), (x, z) and (y, z) projections of two orbits of the RTBP that correspond to two orbits of the Type II Family. Down: These two orbits are marked (with the same color) in the Poincaré section of the center manifold of the RTBP at L_2.

3.4.1 Stability

To fully characterize these orbits, we study their stability. Using the method described in Section 2.3, the stability of all the tori computed for each one of the families is obtained. For the Type I Halo family, they mostly behave like their counterparts in the RTBP, the Halo orbits. Due to the Hamiltonian structure, there is always the eigenvalue 1 with multiplicity two. For each tori of this family there is a large real eigenvalue (and its inverse), and, for almost each tori, a complex eigenvalue (and its inverse) with modulus 1. The absolute value of the latter pair of eigenvalues is shown in Figure 3.13 with respect to the x component of the invariant curve at $\theta = 0$. It is observed that most of these pairs of eigenvalues have modulus 1 with the exception of some isolated zones. However, the main takeaway is that most of the tori are partially elliptic with one saddle. On the other hand, the Type II Halo family has a different stability type. In this case, and as in the case of the Type I Halo family, there is always the eigenvalue 1 with multiplicity two. There is also a large real eigenvalue (and its inverse). The other pair, however, is also real and positive. Figure 3.14 shows the evolution of this eigenvalue with respect to the x component of the invariant curve at $\theta = 0$. Hence, the Type II Halo family has two saddles. We note that the largest eigenvalues of the Type I and Type II families are of the same order of magnitude.

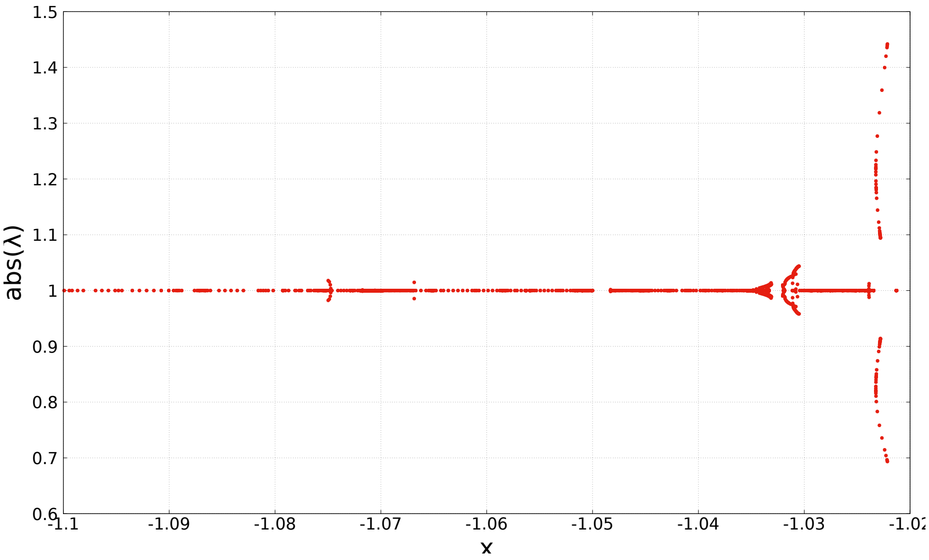

Figure 3.13: Absolute value of the second eigenvalue along the Type I Halo family in the BCP. See the text for more details.

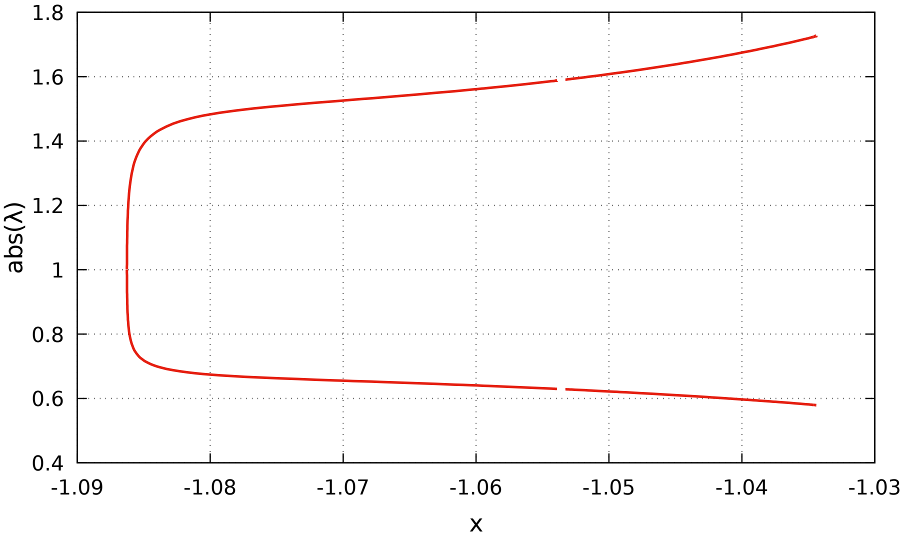

Figure 3.14: Absolute value of the second eigenvalue along the Type II Halo family in the BCP. See the text for more details.

3.5 Applications

The existence of two Halo-like families illustrates a resonance between the direct effect of the Sun's gravity, as modeled in the BCP, with a quasi-Halo orbit of the RTBP. We emphasize the dependency on how the effect of the Sun is accounted for because, for example, the QBCP also models the direct effect of the Sun's gravity but, as of today, only the quasi-periodic counterparts of the Halo orbits (Type I family) have been computed (see [Andreu, 1998]). The existence of Type II Halo-like orbits in the QBPC is an open problem. Hence, the BCP has this feature that may be exploited for mission design: the existence of a second family with a similar topology to the Halo orbits, provides mission analysts with new potential candidates to meet the requirements for missions to the vicinity of the Moon.

However, when it comes to practical applications, there are some caveats that need to be addressed. The main one is that the Type I and Type II families need a counterpart in a real ephemeris model. We are aware that the usefulness of a model is limited by how well it captures the reality it tries to represent. There is numerical and experimental evidence that the Halo orbits in the Sun-Earth-Moon system exist in the real one. In [Andreu, 1998], using quasi-periodic Halo orbits in the QBCP and the DE403 JPL ephemeris, the author propagates for times intervals between 22 and 45 years Halo orbits of the Solar System. Hence, there is reason to believe that the same applies to the orbits in the BCP of the Type I family. However, for the Type II family there is no evidence that they are feasible in an ephemeris model. We may be in a situation where they do not survive the transition between the BCP and the ephemeris model. The study of the persistence of these families in a realistic model is future work.

Finally, let us comment a bit more on the Type II Halo family, that shares some topological features with Type I Halo family. This gives the mission designer more options to explore potential orbits for the mission. Note that there are representatives members of each family that are not blocked by the Moon, making them useful for missions to the neighborhood of the Moon that require constant contact to the Moon. Figure 3.15 shows the projection on the $x = 0$ plane corresponding to how these orbits would be seen from an observer in the Earth. The projections in Figure 3.15 correspond to the same orbits shown on Figures 3.10 and 3.11. In these figures, the center of the Moon is at the origin, and it has been plotted a circle with the approximated radius of the Moon, and another one with a circle twice the radius of the Moon. In both cases it is observed that there is continued line-of-sight between the Earth and the orbit. Finally, it is worth noting that in the particular case of the Type II Halo family, given that they are less stable, they would be most likely discarded to place a permanent station. However, their suitability for other applications would be always contingent to the mission requirements.

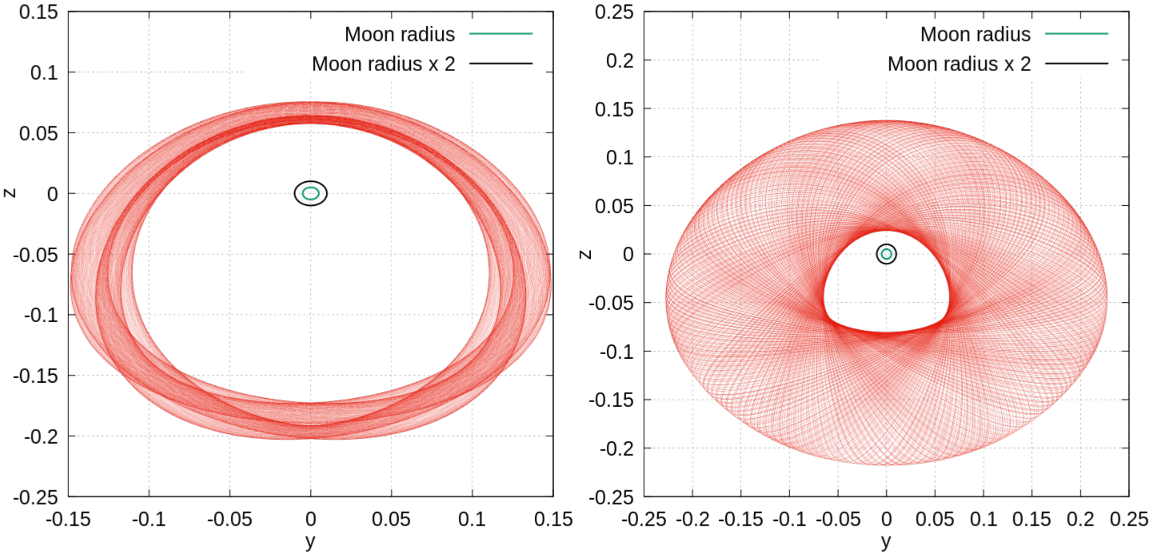

Figure 3.15: Type I (left) and Type II (right) Halo orbits as seen from the Earth with the Moon radius superimposed.

3.6 Examples of other families

In this section some examples of tori from the other families found are given (see Figure 3.4). They are provided here to illustrate the richness of the Sun-Earth-Moon BCP, and to evidence that the vertical families V1 and V2 are not Halo-like. A complete study of their stability properties and how they transition from the RTBP to the BCP was not done in the context of this dissertation.

The planar tori from the families H1 and H2 are very similar, and two examples of each one are shown in Figure 3.16. The representative of the family H1 (left) has rotation number $\rho =$ `0.5226878126286740`. The rotation number of the representative of the family H2 (right) is $\rho =$ `0.2586841081044178`.

More interesting are the families V1 and V2 with a vertical component. Different projections of a representative of the family V1 with rotation number $\rho =$ `0.6510146280704701` are shown in Figure 3.17. The projection onto the plane $x = 0$ (botton-left image) shows that this orbit falls behind the Moon.

Finally, and example of the family V2 is illustrated in Figure 3.18. This torus has rotation number $\rho =$ `0.5852970529159898`. It also falls behind the Moon. However, the projection onto the plane $x = 0$ (botton-left image) show that it has different symmetry than the representative of the V1 family.

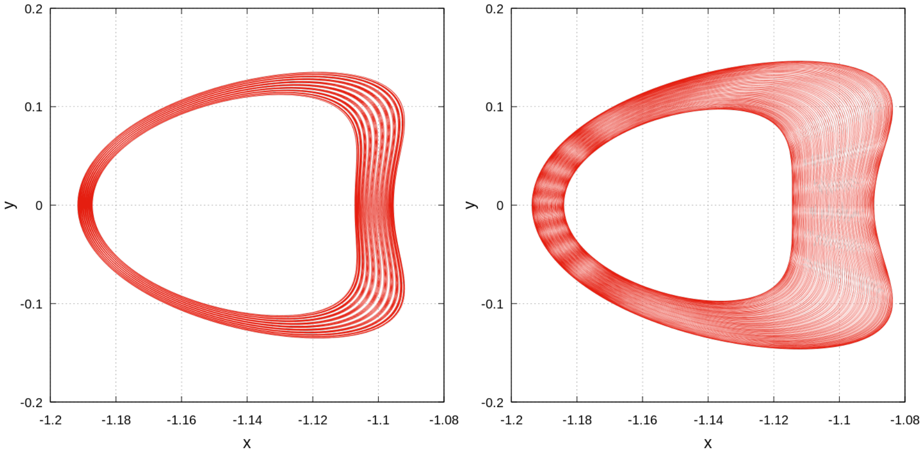

Figure 3.16: Projections of a H1 orbit (left) and a H2 orbit (right).

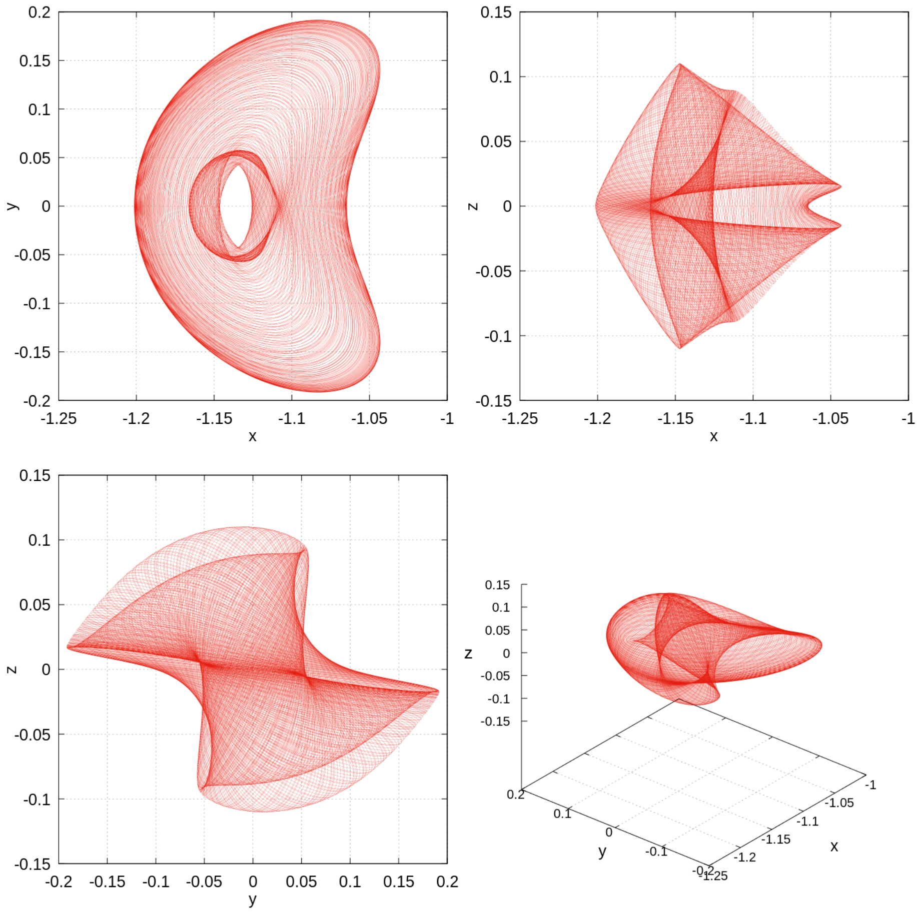

Figure 3.17: Different projections of a V1 orbit.

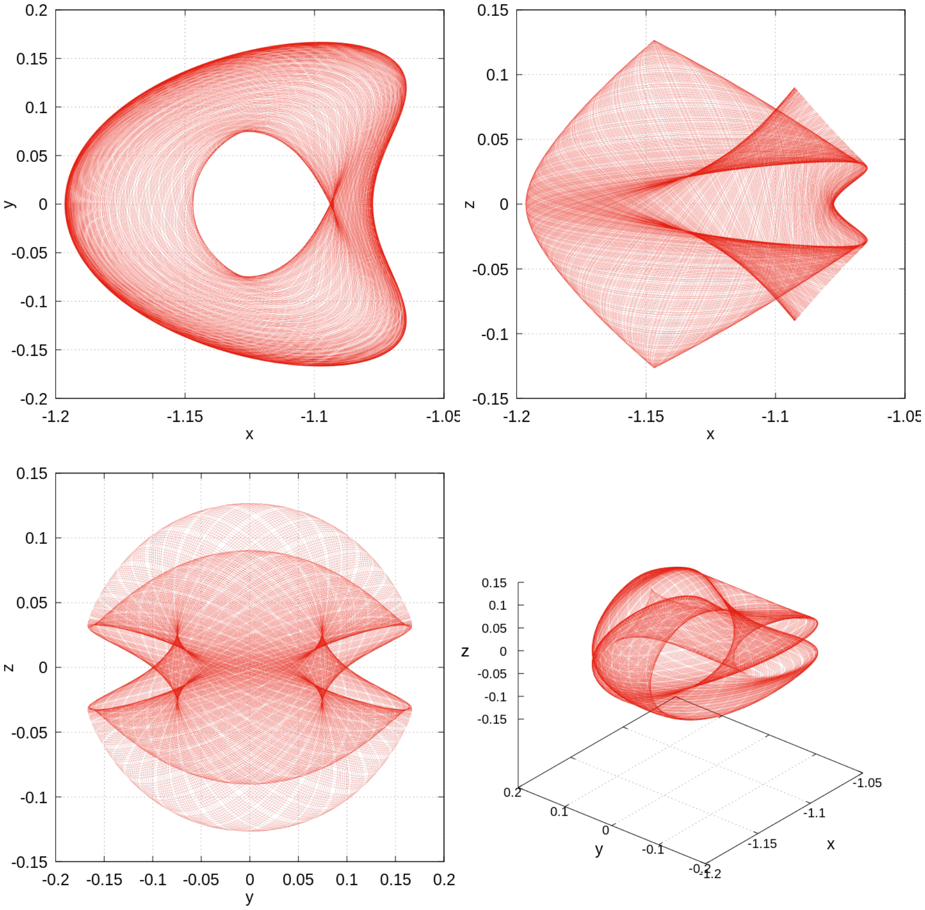

Figure 3.18: Different projections of a V2 orbit.

Chapter 4

Contributions to the Quasi-Bicircular Problem

This chapter studies some aspects of the dynamics around the collinear points in the QBCP model. In this model, the reduction to the center manifold provides meaningful results for L_1 and L_2, but not for L_3. Also, by continuing 2D invariant tori we can identify some of the families that exist and how they are connected. This chapter starts reviewing in Section 4.1 the connection between the collinear libration points in the RTBP, and their dynamical equivalents in the QBCP. These results are known (see for example [Andreu, 1998, Jorba-Cuscó et al., 2018]), but due to their relevance it was considered that they deserve their own section. This paves the way to Section 4.2, where a qualitatively description of the dynamics in a vicinity of the L_1 and L_2 points is provided by means of a reduction to the center manifold technique described in Section 2.1. Finally, the analysis around the L_1 and L_2 is complemented with a study of some families of 2D invariant tori. These results are discussed in Section 4.3.

4.1 Dynamical substitutes of the collinear points

In the QBCP, the collinear points in the RTBP are replaced in the QBCP by small periodic orbits with the same period as the perturbation. These orbits are computed by continuation from the RTBP to the QBCP. The formulation of the problem is defined in [Andreu, 1998], and reproduced here for completeness. The starting point is the family of Hamiltonians H^{ε}, where $\varepsilon \in [0,1]$ is a parameter:

$$H^{\varepsilon} = H_{RTBP} + \varepsilon(H_{QBCP} - H_{RTBP}), \quad \varepsilon \in [0,1] \tag{4.1}$$

Note that in Equation (4.1), $H^0 = H_{RTBP}$, and $H^1 = H_{QBCP}$. The process is the same used in the context of the BCP in Section 3.1: the starting point is the collinear equilibrium point $L_i, i = 1, 2, 3$, and then the value of ε is increased until it reaches $\varepsilon = 1$ (this is, the QBCP model). For each value of $\varepsilon \in [0,1]$, there is a T_s-periodic orbit. The result of this

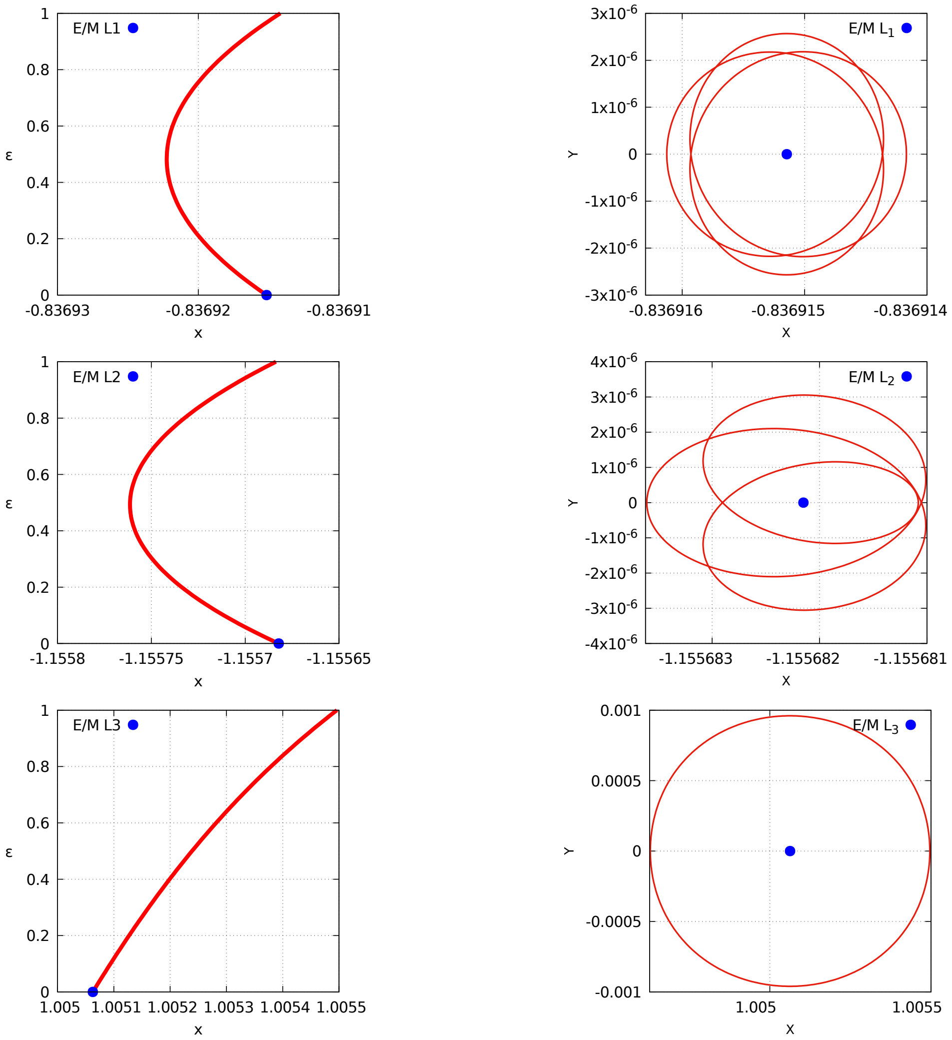

Figure 4.1: Dynamical substitutes of the RTBP collinear points in the QBCP (L_1, top row; L_2, middle row; and L_3, bottom row). The first column represents in the x-axis the first component of the periodic orbit's position at $t = 0$, and the y-axis its associated value of $\varepsilon \in [0, 1]$. The second column contains the dynamic substitutes in the QBCP (this is, the periodic orbits obtained for $\varepsilon = 1$).

continuation process is illustrated in the first column of Figure 4.1 for the collinear libration points, and the second column shows their dynamic substitutes in the QBCP. The first row corresponds to L_1, the second row to L_2, and the third one to L_3.

In all three cases there is a direct connection between the starting point and the final periodic orbit. We recall that in the BCP, for L_2 this was not the case (see Figure 3.1). Also, in the QBCP there are no changes of stability, and throughout the continuation process the stability type of the periodic orbits is saddle×center×center for all values of $\varepsilon \in [0, 1]$. For completeness, the eigenvalues of the monodromy matrices associated to the dynamical substitutes for the collinear points are listed in Table 4.1.

Table 4.1: Monodromy matrix eigenvalues $\lambda_{i,j}, i, j = 1, 2, 3$ of the dynamical substitutes for $L_i, i = 1, 2, 3$. (L_1, top; L_2, middle; and L_3, bottom).

j	abs($\lambda_{1,j}$)	arg($\lambda_{1,j}$)
1	`460182151.5759`	`0.000000000000`
2	`1.000000000000`	`2.871101174766`
3	`1.000000000000`	`2.981120162511`

j	abs($\lambda_{2,j}$)	arg($\lambda_{2,j}$)
1	`2397196.843443`	`0.000000000000`
2	`1.000000000000`	`0.408977840813`
3	`1.000000000000`	`0.091483781904`

j	abs($\lambda_{3,j}$)	arg($\lambda_{3,j}$)
1	`3.370855392447`	`0.000000000000`
2	`1.000000000000`	`0.527951493583`
3	`1.000000000000`	`0.571392912449`

4.2 Center manifold around the collinear points

In this section the dynamics in a vicinity of the collinear Earth-Moon $L_i, i = 1, 2, 3$ points in the QBCP model are studied by means of a reduction to the center manifold. The center manifold has been computed for the dynamic equivalents of the L_1, L_2, and L_3 collinear points. These are the T_s-periodic orbits presented in Figure 4.1. From now on, we will refer to the dynamic equivalent of L_1 as POL1, L_2 as POL2, and L_3 as POL3.

The implementation of the reduction to the center manifold follows the algorithm described in Section 2.1. As a summary, this process consists in the following steps:

- A linear time-dependent change of coordinates such that in the new variables the periodic orbit becomes an equilibrium point centered at the origin, plus a scaling to make the unit of distance equal to the distance between the libration point studied and the closest primary. We call this distance $\gamma_i, i = 1, 2, 3$, and the values used are listed below:

i	γ_i
1	0.1509342729900642
2	0.1678327317370704
3	0.9929120625260284

This results in a (non-autonomous) Hamiltonian with no linear components. (See Section A for details on this transformation.)

- A symplectic time-dependent change of coordinates such that in the new variables the second order components of the (non-autonomous) Hamiltonian obtained in the previous step are in normal form and time-independent. (See Section 2.1.1.) The normal frequencies chosen in each case are:

Case	α_1	ω_1	ω_2
POL1	2.93720564115629	2.27316022488810	2.33661946019073
POL2	2.16306748237037	1.79017018257069	1.86386291350378
POL3	0.17893268263693	1.00293658659005	1.00933331442407

  where in all three cases α_1 corresponds to the hyperbolic part, and ω_1 and ω_2 to the elliptical parts. Note that, for each case, these normal frequencies are very similar to their associated equilibrium points counterparts in the RTBP. We define for convenience the following vector $\omega = (\alpha_1, i\omega_1, i\omega_2)$.

- An expansion of the Hamiltonian with second order terms in an autonomous normal form, and other non-linear terms expanded as a series of homogeneous polynomials. (See Section B for details on this expansion.)

- A symplectic and time-dependent change of variables to transform the non-autonomous Hamiltonian in an autonomous one up to certain degree N. (See Section 2.1.2.)

The last step is done such that the resulting expansion of the Hamiltonian has the elliptic and the hyperbolic dynamics decoupled. In other words, that we have a description of the neutral dynamics (this is, the center manifold) around the periodic orbit of choice. Note that for dynamic equivalents of the collinear $L_i, i = 1, 2, 3$ points, the center manifold has dimension four.

The coefficients of the Hamiltonian restricted to the central manifold around POL1, POL2, and POL3 have been computed up to degree $N = 16$. During this process, the following indicators have been calculated:

- The presence of small divisors

- Estimated radius of convergence of the series for different values of N

A proxy to measure the presence of small divisors are the denominators of the form $\delta_D(j, K^0, K^1) = j\omega_S\sqrt{-1} - < \omega, K^1 - K^0 >$ that appear the generating functions as defined in Section 2.1.2. Only for the reduction to the center manifold around POL3 there were values of $\|\delta_D(j, K^0, K^1)\|$ of the order of 10^{-3}. These values appeared for degrees above 10. No small divisors smaller that 10^{-2} were identified in the computation of the center manifold around POL1 or POL2 for degrees up to $N = 16$.

About the radius of convergence, let $H = H_2 + ... + H_N$ be a Hamiltonian defined as in Equation (2.1), where $H_i, i = 2, ..., N$ are as defined in Equation (2.3). The radius of convergence is computed as

$$r_n = \frac{1}{\sqrt[n]{\|H_n\|_1}}$$

where $\|H_n\|_1 = \sum_{|k|=n} |a_k|, 3 \leq n \leq N$. The radius of convergence for different values of n are shown in Table 4.2 for POL1, Table 4.3 for POL2, and in Table 4.4 for POL3.

Table 4.2: Radius of convergence for some values of n for the center manifold around POL1

n	r_n	n	r_n
6	9.813101e-01	12	9.838444e-01
8	9.913491e-01	14	9.708615e-01
10	9.909848e-01	16	9.609837e-01

Table 4.3: Radius of convergence for some values of n for the center manifold around POL2

n	r_n	n	r_n
6	8.199574e-01	12	7.106946e-01
8	8.108276e-01	14	5.779491e-01
10	7.983601e-01	16	5.137823e-01

Table 4.4: Radius of convergence for some values of n for the center manifold around POL3

n	r_n	n	r_n
6	1.701723e-01	12	7.586620e-02
8	1.325412e-01	14	6.418318e-02
10	8.533646e-02	16	5.916533e-02

For POL3 it is observed that the radius convergence is very small. Hence, the reduction to center manifold does not provide useful information about the dynamics in a large enough neighborhood around L_3. This is consistent with the results obtained in [Jorba and Masdemont, 1999]. As a result of this, we will focus our attention on the

L_1 and L_2, where the radius of convergence of the center manifold series is big enough to capture the dynamics in a big vicinity of these points. Sections 4.2.1 and 4.2.2 discuss the results for the L_1 and L_2 cases respectively.

4.2.1 Center manifold around L_1

The expansion of the center manifold is a Hamiltonian an expression $H_{CM} = H_2 + ... + H_N$ like Equation (2.1), where $H_k, k = 2, ..., N$ are as defined in (2.3). Specifically, each H_k is an expression of the form

$$H_k = \sum_{k_1+k_2+k_3+k_4=k} a_{(k_1,k_2,k_3,k_4)} Q_1^{k_1} P_1^{k_2} Q_2^{k_3} P_2^{k_4}, \quad k_i \in \mathbb{N}, i = 1, ..., 4 \tag{4.2}$$

where (Q_1, Q_2) are the positions, and (P_1, P_2) the conjugated momentums. The coefficients, up to degree 6, of the Hamiltonian of the center manifold corresponding to the periodic orbit POL1 are captured in Table 4.5.

Table 4.5: Hamiltonian reduced to the central manifold up to order 6 around POL1

k_1	k_2	k_3	k_4	$a_{(k_1,k_2,k_3,k_4)}$	k_1	k_2	k_3	k_4	$a_{(k_1,k_2,k_3,k_4)}$
2	0	0	0	1.1365801124440E+00	1	1	0	3	-7.4012409047879E-02
0	2	0	0	1.1365801124440E+00	0	2	0	3	9.6176086630088E-09
0	0	2	0	1.1683097300953E+00	0	0	2	3	8.0037887245600E-08
0	0	0	2	1.1683097300953E+00	0	0	1	4	1.4436762488537E-01
2	0	1	0	-4.2742797554386E-01	0	0	0	5	-6.7934034132082E-08
0	2	1	0	-5.3891327233143E-05	6	0	0	0	6.2094210958681E-03
0	0	3	0	2.5523418206125E-02	5	1	0	0	-6.7815393271166E-09
1	1	0	1	-1.2254290645138E-04	4	2	0	0	-2.0086057404615E-02
0	0	1	2	-4.9529829287648E-01	2	4	0	0	2.7250801950251E-02
4	0	0	0	-1.0387633163417E-01	0	6	0	0	-1.2378414626373E-03
2	2	0	0	8.5654706992094E-02	4	0	2	0	-2.1866965033703E-03
0	4	0	0	1.0812958900733E-05	3	1	2	0	1.6754220796143E-09
2	0	2	0	2.1622139838010E-01	2	2	2	0	1.0778375887518E-01
1	1	2	0	-1.4863019899213E-09	1	3	2	0	1.0666533414263E-08
0	2	2	0	-1.5360957052390E-02	0	4	2	0	-8.5673296189717E-03
0	0	4	0	-1.5779796388201E-02	2	0	4	0	5.0908816751363E-02
2	0	1	1	-9.1489731924294E-08	1	1	4	0	1.0801455668335E-08
1	1	1	1	-3.2495127186968E-02	0	2	4	0	-1.2873305122172E-02
0	2	1	1	-3.2599524388118E-08	0	0	6	0	-5.5676966532490E-03
0	0	3	1	-2.1506277895067E-08	4	0	1	1	7.1268148429479E-08
2	0	0	2	-2.4182953302687E-01	3	1	1	1	8.6670022069764E-02
1	1	0	2	1.4246394326115E-09	2	2	1	1	-4.8046664060818E-08
0	2	0	2	9.9396670609705E-02	1	3	1	1	-3.7167629573763E-02
0	0	2	2	2.8794821677007E-01	0	4	1	1	-1.6472545989214E-08

Table 4.5: (continued)

k_1	k_2	k_3	k_4	$a_{(k_1,k_2,k_3,k_4)}$	k_1	k_2	k_3	k_4	$a_{(k_1,k_2,k_3,k_4)}$
0	0	1	3	-9.9796480381400E-08	2	0	3	1	-7.0795221695100E-08
0	0	0	4	-1.4074479895471E-01	1	1	3	1	-1.0655124578491E-01
4	0	1	0	3.7745746907786E-02	0	2	3	1	-3.9935005395564E-08
3	1	1	0	-3.1696042934014E-09	0	0	5	1	-2.4022343097574E-08
2	2	1	0	-1.2726077950140E-01	4	0	0	2	2.0982296568260E-02
0	4	1	0	1.0507633803701E-02	3	1	0	2	-3.3030448427256E-08
2	0	3	0	-1.1083737547103E-01	2	2	0	2	-3.1233429812347E-02
1	1	3	0	-6.0652645741202E-09	1	3	0	2	-4.9317299850824E-09
0	2	3	0	2.2665985616829E-02	0	4	0	2	2.0641390341789E-02
0	0	5	0	1.1494979183962E-02	2	0	2	2	-8.3158755543959E-02
4	0	0	1	-6.0213290782196E-08	1	1	2	2	-1.4711027029686E-09
3	1	0	1	-6.3675915101523E-02	0	2	2	2	1.0852170163338E-01
2	2	0	1	8.9009096319913E-09	0	0	4	2	1.2851003627049E-01
1	3	0	1	1.7507059394155E-02	2	0	1	3	1.7764130617398E-07
0	4	0	1	2.2357098086265E-08	1	1	1	3	1.1650111509816E-01
2	0	2	1	7.4917970217832E-08	0	2	1	3	-4.4546287345114E-08
1	1	2	1	1.0126378333879E-01	0	0	3	3	-7.3158413868625E-08
0	2	2	1	4.8672743292813E-08	2	0	0	4	2.3630929451164E-02
0	0	4	1	3.0269274038578E-08	1	1	0	4	-2.6455321799499E-08
2	0	1	2	1.6813758407154E-01	0	2	0	4	-1.5729517313961E-03
1	1	1	2	-1.8563276032978E-09	0	0	2	4	-1.0317240849019E-01
0	2	1	2	-1.3157209372648E-01	0	0	1	5	1.0687307053187E-07
0	0	3	2	-2.0539268138325E-01	0	0	0	6	8.8701987970122E-03
2	0	0	3	-1.2846150897253E-07					

After the computation of the center manifold, the test described in Section 2.1.3 was executed to check the software implementation and that, numerically, the computed center manifold behaves as expected. The initial condition integrated was of the form $x_0 = (\lambda_0, \lambda_0, \lambda_0, \lambda_0)/2$, where $\lambda_0 \in \mathbb{R}^+$. Note that x_0 is divided by 2. This is done so the value λ_0 is equal to the distance of the initial condition from the origin (i.e., $\|x_0\|_2 = \lambda_0$). The integration timespan was from $t = 0$ to $t = 1$.

For the L_1 case (orbit POL1), the results of the test for $N = 16$ are in Table 4.6 and Table 4.7. The results in Table 4.5 illustrate how as the distance of the initial condition x_0 from the origin increases, the error also increases. The Table 4.5 shows good agreement between the degree of the center manifold approximation and the order of the error. Hence, it is safe to conclude that the center manifold has been properly computed.

For the sake of completeness, the accuracy of the center manifold obtained was estimated. The process to estimate the accuracy is described in [Andreu, 2002], and also in a similar fashion in [Le Bihan et al., 2017a]. The results of this test are plotted in Figure 4.2a and Figure 4.2b. In Figure 4.2a the logarithm of the error is plotted against the distance

Table 4.6: Differences between the POL1 center manifold predictions and a numerical integration for $N = 16$

λ_0	$\|v_0 - v_0^1\|_2$	λ_0	$\|v_0 - v_0^1\|_2$
0.125	2.532617e-10	0.250	3.989719e-08
0.150	3.631822e-10	0.275	1.817547e-07
0.175	5.019000e-10	0.300	7.241818e-07
0.200	1.267081e-09	0.325	2.579780e-06
0.225	7.452637e-09	0.350	8.355658e-06

Table 4.7: Estimations of the truncation order for the reduction to the centre manifold around POL1 for $N = 16$

$\lambda_0^{(1)}$	$\lambda_0^{(2)}$	n
0.125	0.150	1.97717
0.150	0.175	2.09857
0.175	0.200	6.93523
0.200	0.225	15.04336
0.225	0.250	15.92378
0.250	0.275	15.90966
0.275	0.300	15.88740
0.300	0.325	15.87174
0.325	0.350	15.85841

to the origin, and in Figure 4.2b with respect to the energy for different degrees. As before, these results have been obtained by integrating an initial condition x_0 of the form $x_0 = (\lambda_0, \lambda_0, \lambda_0, \lambda_0)/2$. The data shows that increasing the degree of the expansion does not necessarily translate in a better accuracy around a distance of the origin. This behavior is expected, since the series is not in general convergent in any open set. Finally, the relationship between the distance from the origin and the energy is depicted in Figure 4.2c for different values of N. It can be seen that for different degrees there is good agreement. Note that the analysis described is limited to the subspace defined by $Q_1 = Q_2 = P_1 = P_2$, but is still a good indicator.

One of the main takeaways of the accuracy analysis is that, if we pick an orbit on the center manifold and apply the change of coordinates to transform it to the synodic frame, the resulting object may not be (quantitatively) representative. In some cases, it may be a good initial condition for a refinement algorithm. However, the benefit of the center manifold is that qualitatively it provides a good picture of the dynamics. For the validity of the qualitatively analysis, the radius of convergence (see Table 4.2 for POL1) is the right metric to use. Finally, quantitative description on how some families of objects are organized in a vicinity of L_1 will be discussed in Section 4.3.1.

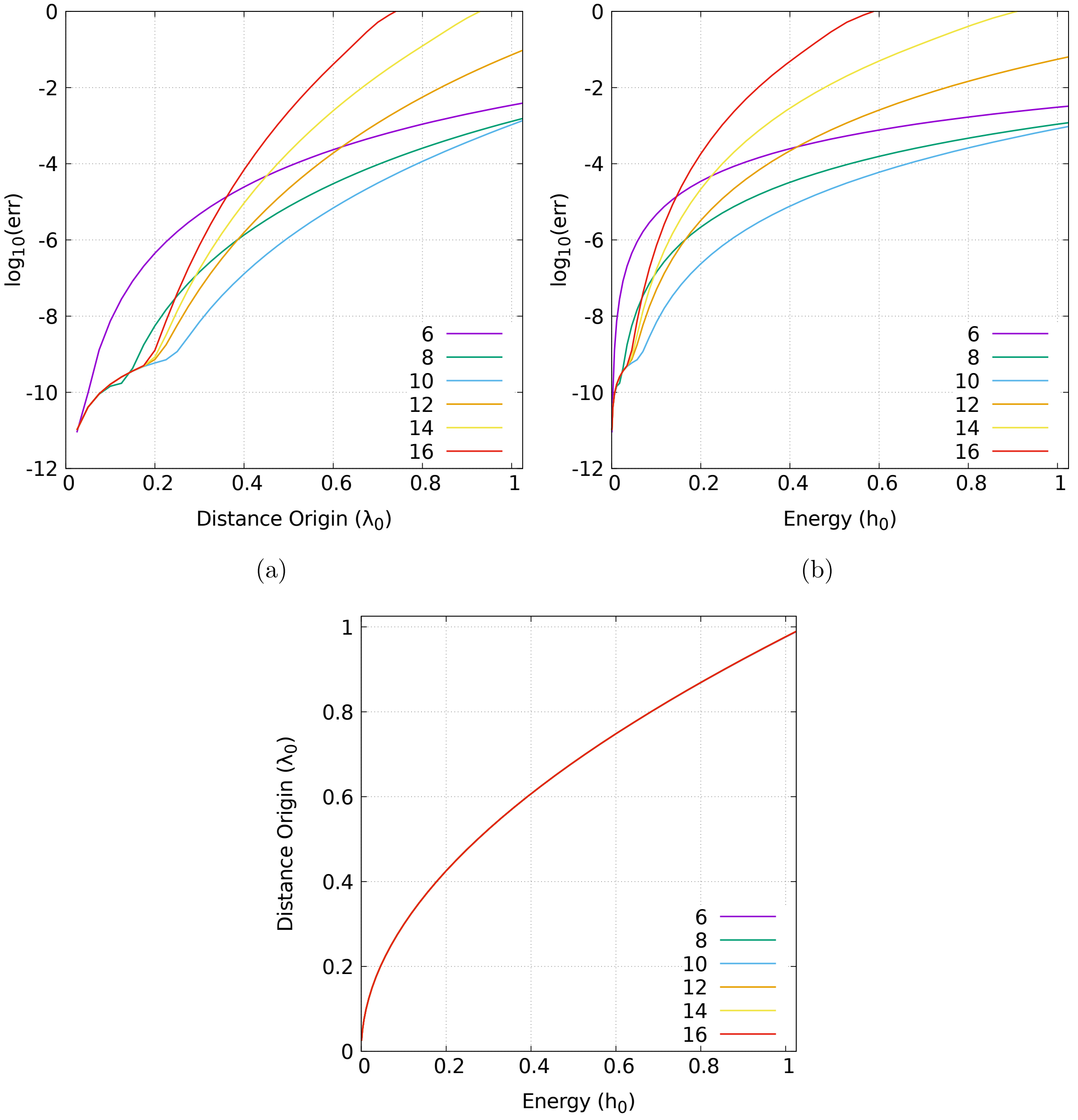

(a) (b)

(c)

Figure 4.2: Accuracy of the center manifold around POL1. See text for details.

To obtain a qualitative description of the dynamics, the (truncated) Hamiltonian reduced to the center manifold has been integrated with degree $N = 16$. Note that the Hamiltonian integrated has two-degrees of freedom. This means that the phase space has dimension four. To visualize the center manifold, it was implemented the process described in [Jorba and Masdemont, 1999]: let (Q_1, P_1, Q_2, P_2) be the coordinates of the Hamiltonian reduced to the center manifold. The starting point is the selection of the 3D Poincaré section $Q_2 = 0$. Then, an energy level h_0 is fixed to obtain a 2D section. Note that the Hamiltonian is autonomous up to order N. Hence, the energy h_0 is conserved for the truncated Hamiltonian. Using this fact, and that $Q_2 = 0$, if values (Q_1, P_1) are picked, the component P_2 in constrained by the energy level and can be computed numerically. (There are two solutions for P_2, one negative and one positive; we used the positive one.) This gives an algorithm to compute initial conditions. These initial conditions are integrated numerically, storing the points that have $Q_2 = 0$ and $P_2 > 0$. The process can be applied by picking as a Poincaré section $Q_1 = 0$ and $P_1 > 0$.

The Poincaré sections for different energy levels using $Q_1 = 0$ are shown in Figure 4.3. Respectively, the Poincaré sections for different energy level for $Q_2 = 0$ are in Figure 4.4. In Figure 4.3 is it observed that for low energy levels ($h = 0.2$), there is a fixed point that corresponds to a periodic orbit. It is observed that this orbit is surrounded by invariant curves that correspond to 2D invariant tori for the reduced Hamiltonian. Note that for the original QBCP Hamiltonian in synodical coordinates, these objects are 3D invariant tori. If the energy level is increased, the space phase undergoes pitchfork bifurcation. The interpretation in the synodic reference is the following: the fixed point close to the origin corresponds to a quasi-periodic vertical Lyapunov in the synodic reference frame. These are invariant tori with two basic frequencies. The quasi-periodic orbit surrounding the origin correspond to quasi-periodic Lissajous orbits with three basic frequencies. The fixed points that appear after the bifurcation takes place correspond to the northern and southern families of quasi-periodic Halo orbits with two basic frequencies. The quasi-periodic orbits around them correspond to quasi-Halo orbits with three basic frequencies.

This is qualitatively similar to the dynamics in around the L_1 region in the BCP (see [Jorba et al., 2020]), and to the results obtained by [Le Bihan et al., 2017a] in the QBCP using the parametrization method to compute the center manifold.

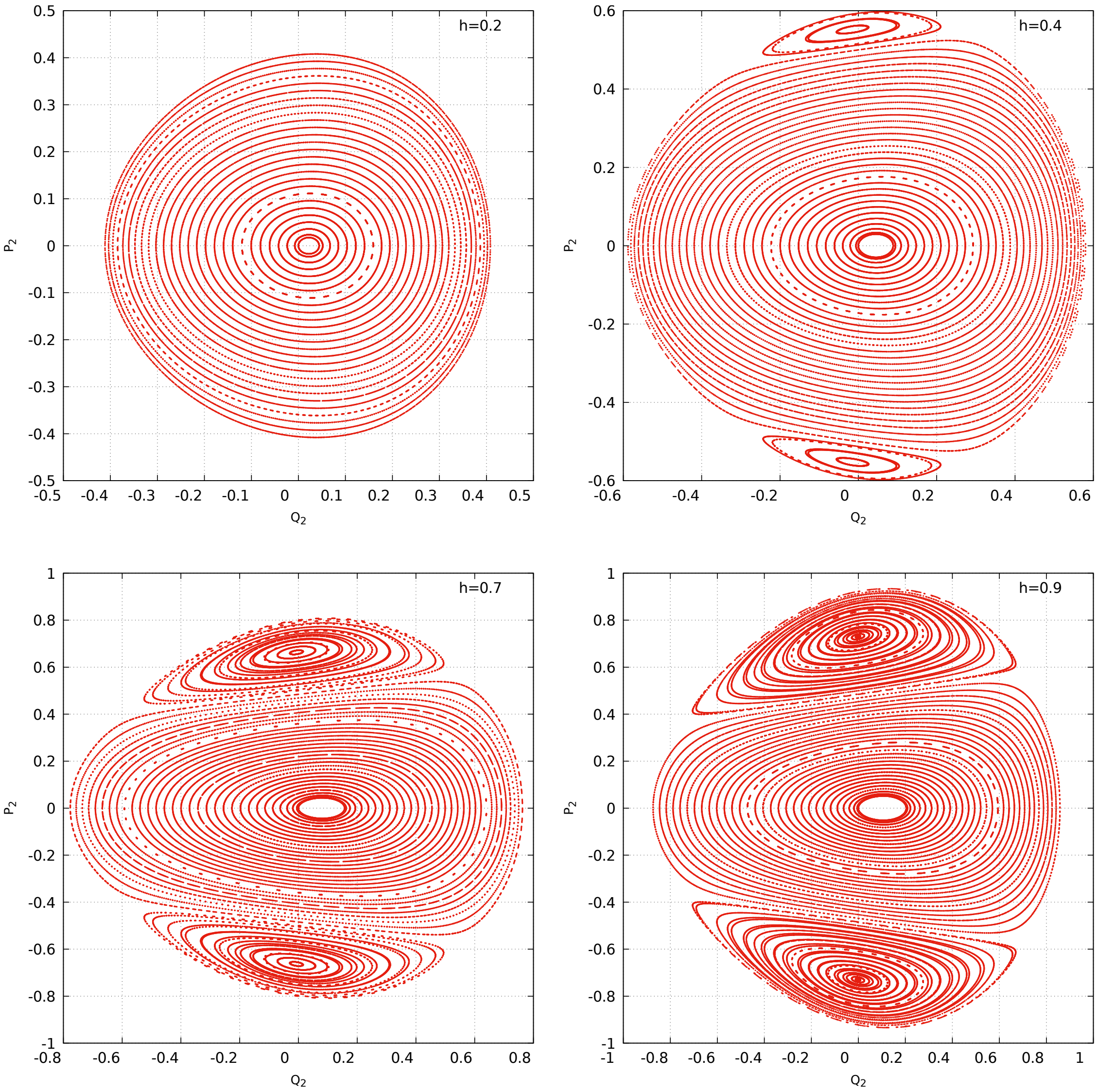

Figure 4.3: Poincaré section $Q_1 = 0$ of the center manifold around POL1 for different energy levels with $N = 16$

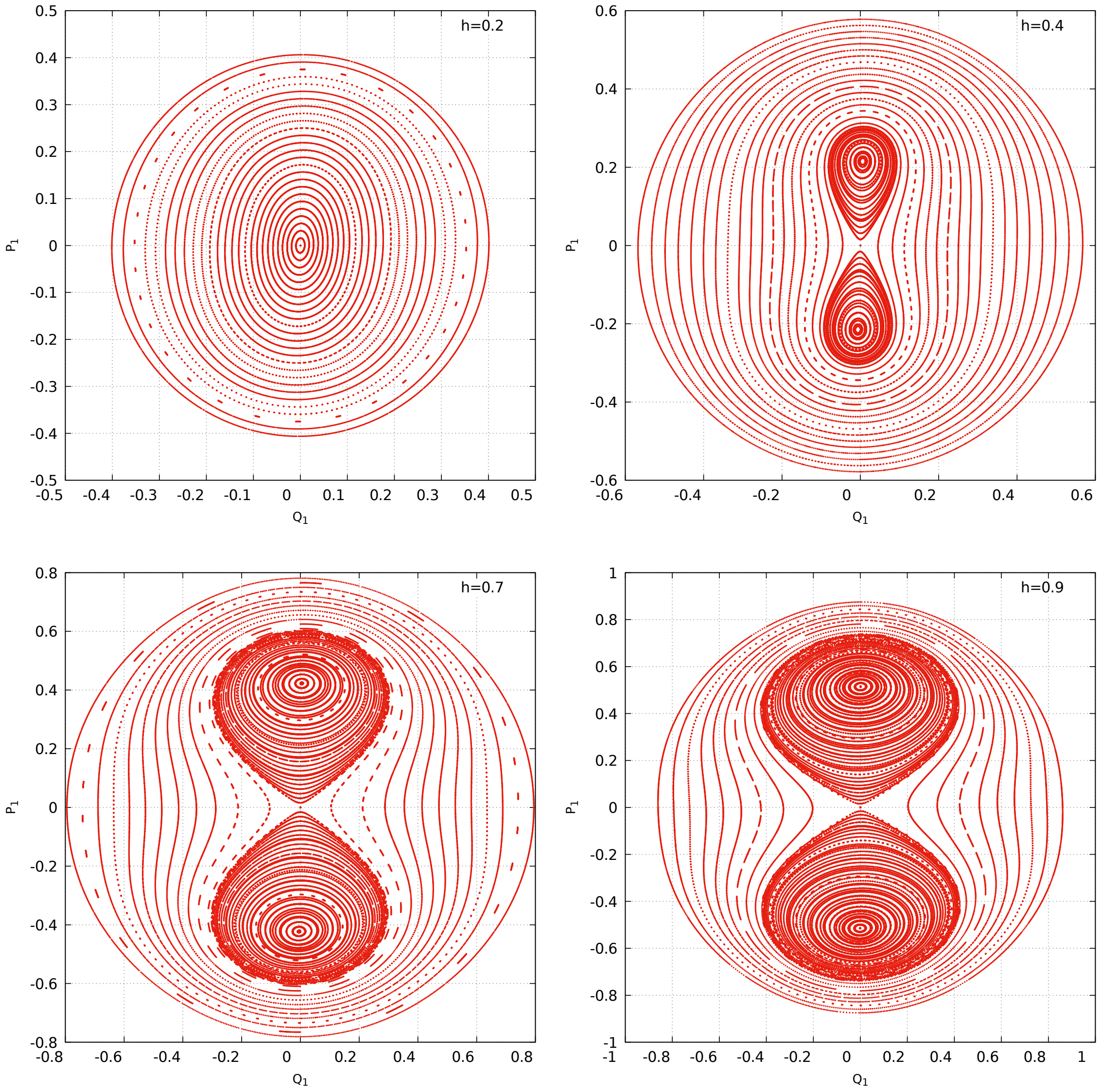

Figure 4.4: Poincaré section $Q_2 = 0$ of the center manifold around POL1 for different energy levels with $N = 16$

4.2.2 Center manifold around L_2

The same process described in Section 4.2.2 is repeated for the L_2 case. The Table 4.8 contains the coefficients, up to degree 6, of the reduced Hamiltonian of the center manifold. Also, the same tests described in Section 4.2.1 are done for the present case. Again, the initial condition is of the form $x_0 = (\lambda_0, \lambda_0, \lambda_0, \lambda_0)/2$, with $\lambda_0 \in \mathbb{R}^+$, and the integration timespan is from $t = 0$ to $t = 1$. The results are captured in Table 4.9 and in Table 4.10. In this case, because the radius of convergence is not as good as in the L_1 case, the degree of the expansion used is $N = 12$. The results in Table 4.8 show that as the distance of the initial condition x_0 from the origin increases, the error increases, too. This behavior is expected. The Table 4.8 shows that the error increases consistently with the degree of the expansion, as explained in Section 2.1.3.

Table 4.8: Hamiltonian reduced to the central manifold up to order 6 around POL2

k_1	k_2	k_3	k_4	$a_{(k_1,k_2,k_3,k_4)}$	k_1	k_2	k_3	k_4	$a_{(k_1,k_2,k_3,k_4)}$
2	0	0	0	8.9508509128534E-01	0	0	3	2	5.8051203522045E-01
0	2	0	0	8.9508509128534E-01	1	1	0	3	-1.7844450052689E-01
0	0	2	0	9.3193145675189E-01	0	0	2	3	-3.0394344483381E-09
0	0	0	2	9.3193145675189E-01	0	0	1	4	-3.0140880721764E-01
2	0	1	0	6.5589636328480E-05	6	0	0	0	-6.4307281988146E-03
0	2	1	0	6.4841149489243E-01	4	2	0	0	8.1725097260177E-02
0	0	3	0	-6.4947365185738E-02	2	4	0	0	-4.2728780806097E-03
1	1	0	1	-1.4657320225294E-04	0	6	0	0	-1.3308183673882E-02
0	0	1	2	8.3042596977058E-01	4	0	2	0	-2.7581282162579E-02
4	0	0	0	1.6691540956563E-05	2	2	2	0	3.0570142682015E-01
2	2	0	0	1.6501717240559E-01	0	4	2	0	4.1375312168077E-02
0	4	0	0	-1.8016477271676E-02	2	0	4	0	-3.0925874741699E-02
2	0	2	0	-4.9579201703060E-02	0	2	4	0	9.6429491577036E-02
0	2	2	0	3.5651315214778E-01	0	0	6	0	-1.0289658815507E-02
0	0	4	0	-4.1231015606744E-02	3	1	1	1	1.9906619251976E-01
1	1	1	1	1.0973656675138E-01	2	2	1	1	-1.7463324777085E-09
2	0	0	2	2.1143854714294E-01	1	3	1	1	-1.5531042568898E-01
0	2	0	2	-4.7292944632242E-02	1	1	3	1	4.7597114070644E-01
0	0	2	2	5.9236862155832E-01	0	2	3	1	-3.0413181902431E-09
0	0	0	4	-3.1058453169198E-02	4	0	0	2	4.1938736410204E-02
4	0	1	0	-4.3777802018475E-02	2	2	0	2	-4.3943735317670E-02
2	2	1	0	2.8508460013478E-01	0	4	0	2	-7.3614758826606E-02
0	4	1	0	-8.3453433400644E-03	2	0	2	2	3.5211138710868E-01
2	0	3	0	-7.6670187245196E-02	1	1	2	2	-3.0449382625031E-09
0	2	3	0	1.9426009938526E-01	0	2	2	2	-1.0297348505084E-01
0	0	5	0	-3.1013224023379E-02	0	0	4	2	4.5913199291929E-01
3	1	0	1	7.4667616272107E-02	2	0	1	3	-1.9587319456264E-09

Table 4.8: (continued)

k_1	k_2	k_3	k_4	$a_{(k_1,k_2,k_3,k_4)}$	k_1	k_2	k_3	k_4	$a_{(k_1,k_2,k_3,k_4)}$
2	2	0	1	-1.0319019428507E-09	1	1	1	3	-2.9968970918954E-01
1	3	0	1	-1.3880815534462E-01	0	0	3	3	-5.6536567341678E-09
1	1	2	1	4.1875686746481E-01	2	0	0	4	-6.3932143025888E-03
0	2	2	1	-1.5463320553586E-09	0	2	0	4	-1.2340310730044E-01
2	0	1	2	2.8479184552457E-01	0	0	2	4	-2.7360468675825E-01
1	1	1	2	-1.6240816892809E-09	0	0	1	5	-1.2601762375995E-09
0	2	1	2	-2.4495800601342E-01	0	0	0	6	-6.5234840557094E-02

Table 4.9: Differences between the POL2 center manifold predictions and a numerical integration for $N = 12$

λ_0	$\|v_0 - v_0^1\|_2$	λ_0	$\|v_0 - v_0^1\|_2$
0.100	2.226642e-12	0.225	3.051407e-09
0.125	3.706322e-12	0.250	1.095514e-08
0.150	2.248650e-11	0.275	3.497710e-08
0.175	1.457249e-10	0.300	1.014818e-07
0.200	7.336179e-10	0.325	2.719555e-07

Table 4.10: Estimations of the truncation order for the reduction to the centre manifold around POL2 for $N = 12$

$\lambda_0^{(1)}$	$\lambda_0^{(2)}$	n
0.100	0.125	2.28349
0.125	0.150	9.88844
0.150	0.175	12.12324
0.175	0.200	12.10403
0.200	0.225	12.10166
0.225	0.250	12.13174
0.250	0.275	12.18007
0.275	0.300	12.24192
0.300	0.325	12.31541

The same analysis of accuracy has been done in this scenario, and the main takeaway is the same as for the L_1 case. The results are captured in Figure 4.5a for the evolution of the logarithm of the error with respect to the distance of the initial condition from the origin, and in Figure 4.5a its evolution with respect to the energy for different degrees of the expansion of the center manifold. The main difference is that initially, for low energies, the error is approximately two orders of magnitude smaller that in the L_1 case. This is consistent with what is observed in [Le Bihan et al., 2017a]. Finally, the distance with respect to the energy is in Figure 4.5c, and again it is shown good agreement for different degrees.

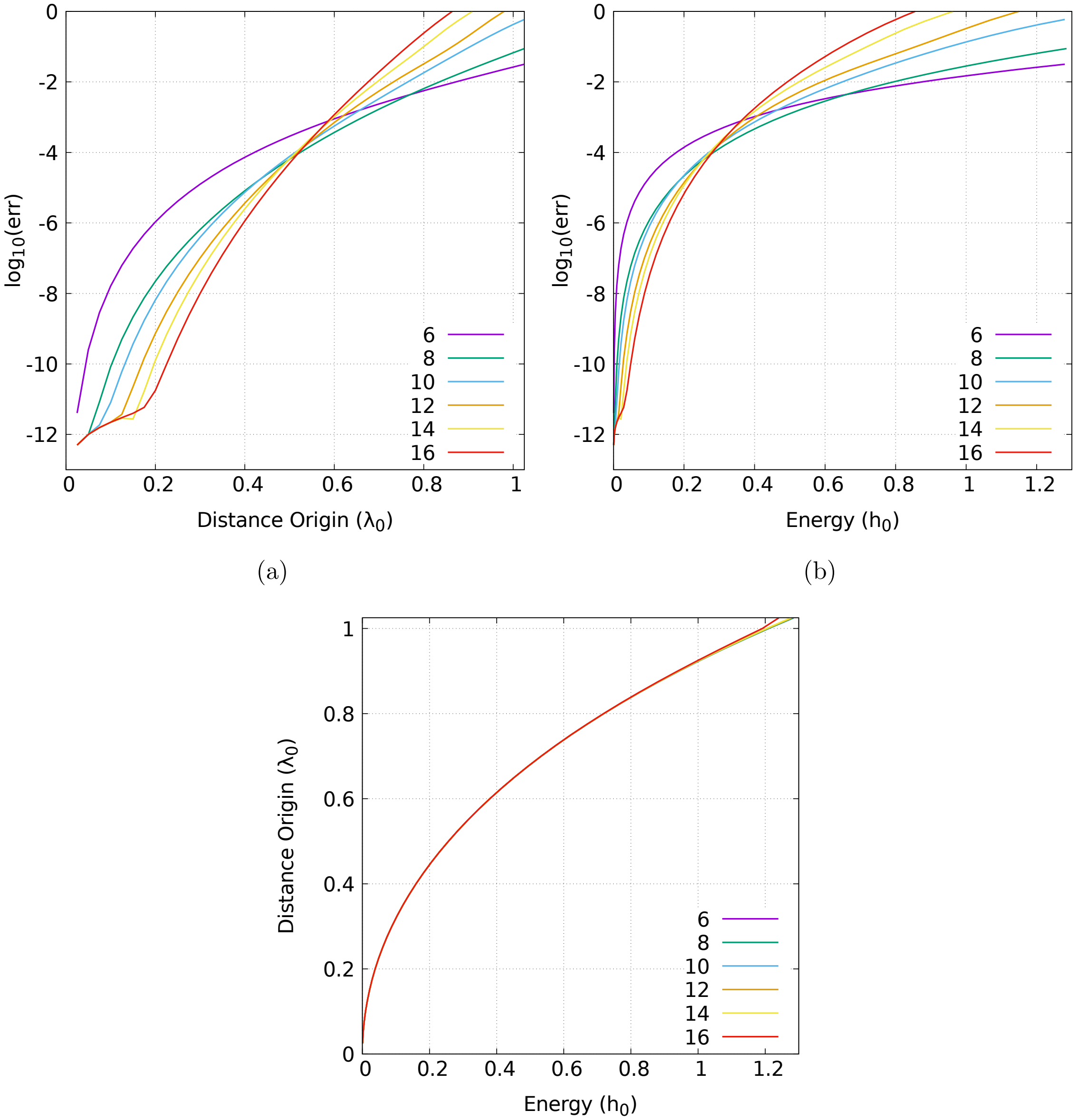

(a)

(b)

(c)

Figure 4.5: Accuracy of the center manifold around POL2. See text for details.

Finally, following the same procedure as for the L_1 case, the Poincaré sections $Q_1 = 0$ and $Q_2 = 0$ at different energy levels have been plotted. These are represented in Figure 4.6 for the section $Q_1 = 0$, and in Figure 4.7 for the section $Q_2 = 0$. The qualitative behavior and its interpretation is equivalent to the L_1 described in Section 4.2.1 and it will not be repeated here. As for the L_1 case, in this scenario the results are also qualitatively consistent with [Le Bihan et al., 2017b]. We remind that in [Le Bihan et al., 2017b] the center manifold was constructed using the parametrization method, and not the Lie transform.

As mentioned in Section 1.2.2, the center manifold around L_2 in the QBCP was also studied (see [Andreu, 2002]). It is important to note that in [Andreu, 2002] the construction of the center manifold is different from the one presented here. The reason is that it follows different criteria. First, the choice of the normal frequencies used in the Floquet transformation for the terms of degree two are different from the ones used here. In [Andreu, 2002], the author uses the following values:

$$\begin{aligned}
\tilde{\omega}_1 &= \texttt{ 1.34709425E-02} \\
\tilde{\omega}_2 &= \texttt{ 2.16306748E+00} \\
\tilde{\omega}_3 &= \texttt{-6.02217885E-02}
\end{aligned}$$

where, in this case, $\tilde{\omega}_1$ and $\tilde{\omega}_3$ correspond to the elliptical parts, and the $\tilde{\omega}_2$ to the hyperbolic part. The differences in the normal frequencies of the elliptical part are due to the multiple determination of the complex logarithm as explained in Section 2.1.1. The relationship between the values used in this thesis and the ones used in [Andreu, 2002] is:

$$\begin{aligned}
\tilde{\omega}_1 &= \omega_1 - 2\omega_s \\
\tilde{\omega}_3 &= \omega_2 - 2\omega_s
\end{aligned}$$

The rationale behind using in 2.1.1 the values $\tilde{\omega}_i, i = 1, 2, 3$ for the Floquet transformation as opposed to those close to the natural frequencies of L_2 is, as argued in [Andreu, 2002], to improve the radius of convergence.

Second, the criteria to kill monomials is also slightly different in [Andreu, 2002]. In that case, the center manifold is computed removing the time dependency (up to certain order), killing all the monomials associated to the hyperbolic part, and those monominals where $K^0 = K^1$ ($K^i, i = 1, 2$ as defined in Section 2.1) as long as the denominators in the creation of the generating function are not smaller that the threshold $\varepsilon = 0.05$.

However, the penalty of constructing the center manifold as in [Andreu, 2002] is that it only provides information for low energy levels. With the criteria used to compute the center manifold in this dissertation, the expression obtained is good enough to provide a good qualitatively description of the dynamics around the L_2 point. Overall, both approaches are valid and offer a different perspective on how the dynamics are organized.

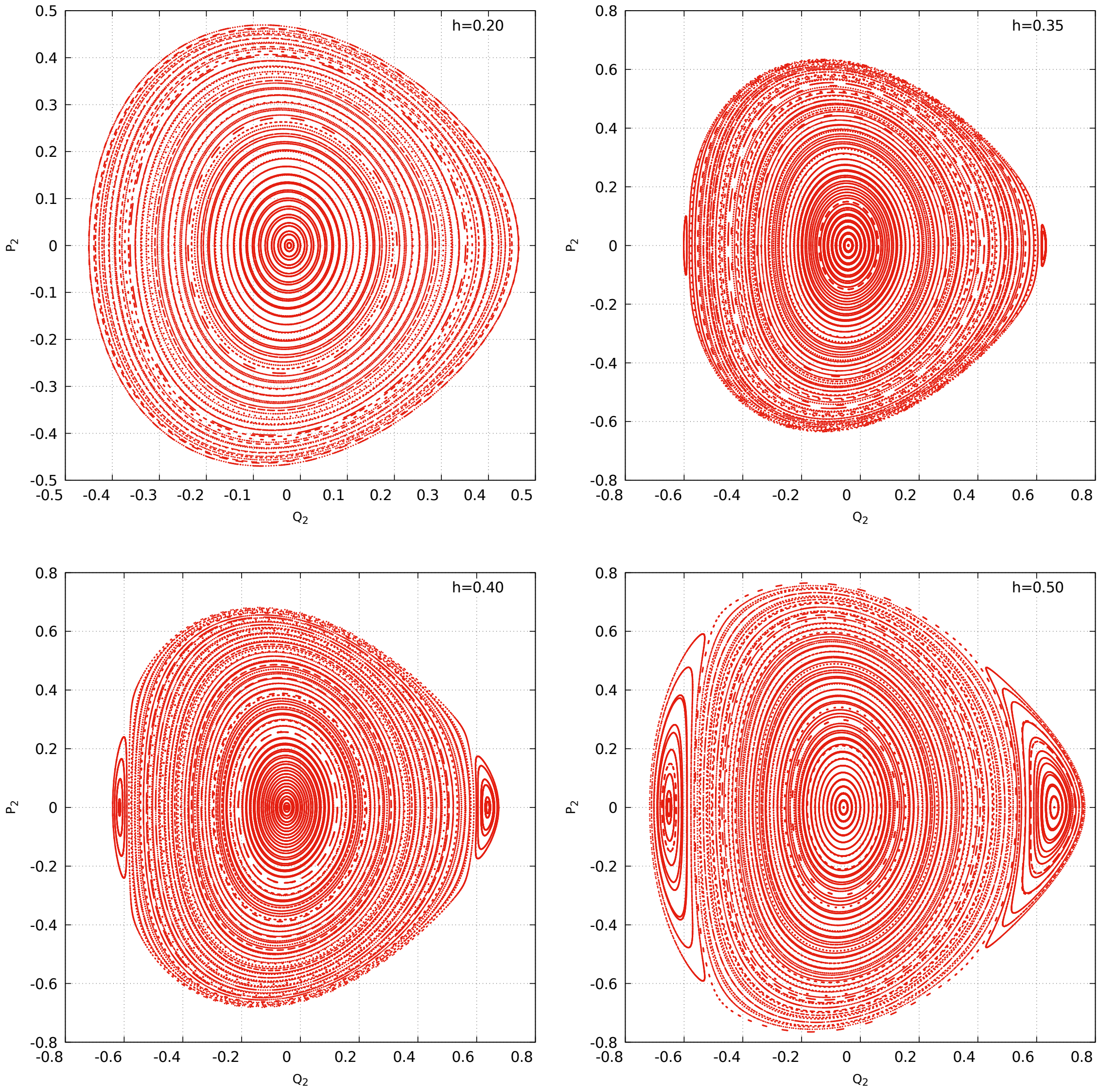

Figure 4.6: Poincaré section $Q_1 = 0$ of the center manifold around POL2 for different energy levels with $N = 12$

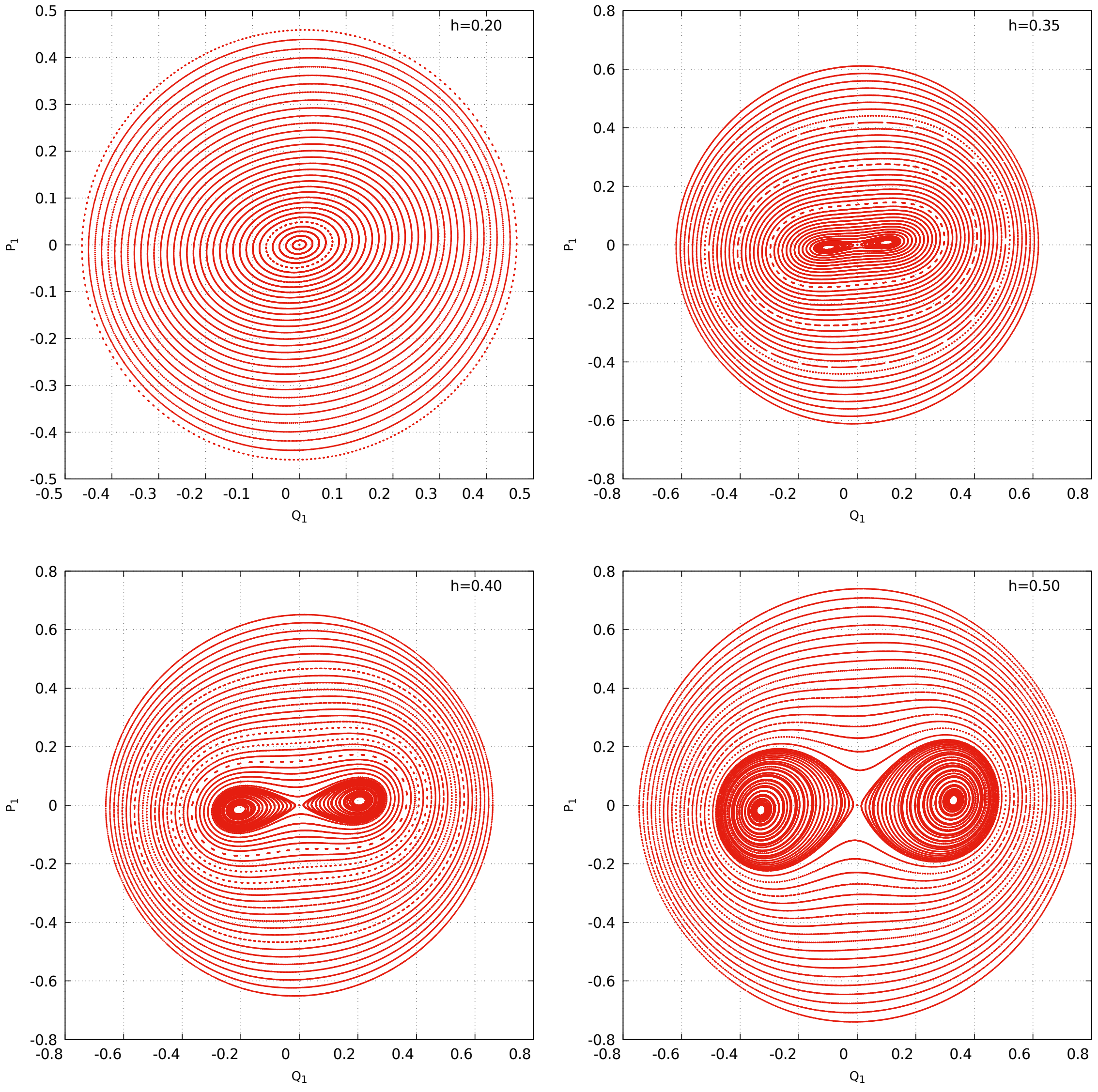

Figure 4.7: Poincaré section $Q_2 = 0$ of the center manifold around POL2 for different energy levels with $N = 12$

4.3 Families of 2D invariant tori

In this section we compute some of the families of 2D invariant tori that live in a vicinity of the collinear points. This is similar to the results described in Section 3.3 for the BCP.

We recall that in the BCP, the tori computed are born around the reference orbit obtained by continuing the L_2 point in the RTBP to the BCP (see Section 3.1). This orbit is of the type saddle×saddle×center, and the center lies in the plane $\{Z = 0\}$. Hence, contrary to the L_2 point in the RTBP, there is no equivalent to the vertical Lyapunov family in the BCP. In this section we show that in the QBCP this family exist for L_1 and L_2. In addition to that, we continue the planar Lyapunov family for each L_1 and L_2 and, by identifying bifurcation points, we continue new the families that have an out-of-plane component. Finally, we show that a big set of Halo orbits in the RTBP survive when continued to the QBCP.

The computation of tori and their stability in this section is computed with the algorithms described in Section 2.2 and Section 2.3. Also, the details and observations made in Section 3.3 regarding the challenges of computing tori also apply to the following subsections.

4.3.1 Families around L_1

This section starts with the analysis of the vertical family of quasi-periodic orbits around L_1. This is the family born from the dynamic equivalent of the L_1 (see Figure 4.1), following the vertical component. This family would be quasi-periodic counterparts in the QBCP of the vertical Lyapunov family that appear in the RTBP. The result of continuing this family is shown in Figure 4.8. The x-axis is the third component of the position vector (the vertical component) when the invariant curve is evaluated at $\theta = 0$. The y-axis is the rotation number of the invariant curve of the Poincaré section. We note that the lower-right part of Figure 4.8, between $x = 0.13$ and $x = 0.14$ there is sharp turn. This reminds to the branch a pitchfork bifurcation obtained by symmetry breaking. We attempted to verify this hypothesis, but we were not successful. This is left as future work.

The stability of this family has been computed for a selected subset of tori. Recall from Section 2.3 and from the L_2 case for the BCP described in Section 3.4.1 that 1 is always an eigenvalue with multiplicity two. Hence, there are two pairs of eigenvalues. The analysis showed that there is always a real eigenvalue (and its inverse). The largest eigenvalue starts with a value of the order of 10^8, and decreases with the rotation number until a value of the order of 10^6. The other pair is formed by a complex value of norm 1 and its conjugate. This is represented in Figure 4.9. Thus, this family is formed by partially elliptic tori. As a final remark, note that no bifurcations were identified. However, based on the results from Section 4.2.1 and specifically shown in Figure 4.3, at least one bifurcation exists. One hypothesis is that step-size used to generate this family probably jumped over the bifurcation. Another explanation may be that the family was not continued long enough.

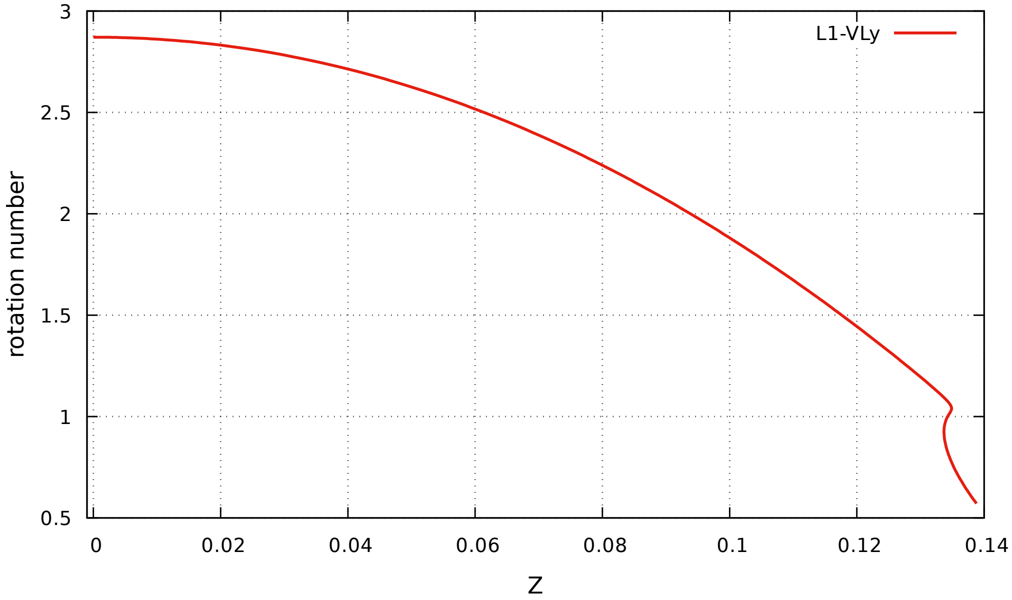

Figure 4.8: Quasi-periodic vertical Lyapunov family in the QBCP around L_1. See text for details.

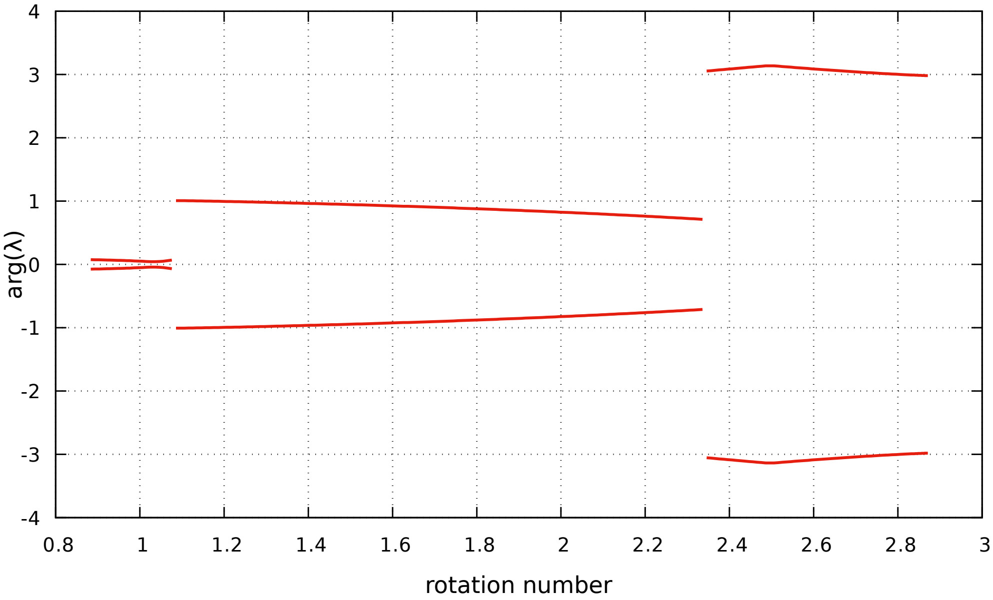

Figure 4.9: Stability of the quasi-periodic vertical Lyapunov family in the QBCP around L_1. See text for details.

The following figures are representative tori of this family, and provided here just to illustrate how their shape and size evolves with the rotation number. The first example, in Figure 4.10 is a torus with rotation number $\rho =$ `2.8710835247657562`. This torus is very small, and close to the periodic orbit that replaces L_1. The second example is in Figure 4.10, and it is a representative of the family with rotation number $\rho =$ `1.7158771247657665`. This is similar to the vertical Lyapunov orbit found in the RTBP around L_1 but "shaken" due to the effect of the periodic time-dependent perturbation. Finally, an example of a large invariant tori with rotation number $\rho =$ `1.0158771247657681` is illustrated in Figure 4.12. It can be seen that all three tori are very different in size and shape.

Next, the family of horizontal quasi-periodic orbits around L_1 born from the planar frequency was computed. This family is the quasi-periodic equivalent to the planar Lyapunov periodic orbits that appear in the RTBP. In addition to the quasi-periodic planar Lyapunov orbits, others families were found during the process. These are captured in Figure 4.13. The x-axis is the first component of the position vector when the invariant curve is evaluated at $\theta = 0$. The y-axis is the rotation number of the invariant curve. The quasi-periodic planar Lyapunov family is colored in green and labeled as L1-HLy. It can be seen that a new family, colored in red and labeled as L1-QV, is born from it. The L1-QV family is born from a bifurcation of the L1-HLy. This bifurcation was identified during the stability analysis of the family L1-HLy. As for the quasi-periodic vertical Lyapunov family, two eigenvalues are real, and the largest one has an order of magnitude between 10^6 and 10^8. Then there is the eigenvalue equal to one with multiplicity two. The last pair of eigenvalues is shown in Figure 4.14, where the x-axis is the rotation number, and the y-axis is the absolute value of the eigenvalue. At the beginning of the family, this pair of eigenvalue are complex with norm equal to one. Then, a bifurcation occurred, and the pair of eigenvalues becomes real. From this bifurcation, the family L1-QV was born. Recall that this bifurcation was observed in the center manifold analysis done Section 4.2.1, where the Figure 4.4 captures the present case.

The first tempting (and natural) thought is to claim that this family corresponds to the Halo orbits in the RTBP. To test this hypothesis, a few Halo orbits in the RTBP were continued from the RTBP to the QBCP. Then this initial orbit was continued in the QBCP. This is the family colored in purple and labeled as L1-Halo seen in Figure 4.13. These two families do not seem to be connected, but it is important to stress the representation of the these families in the figures has its limitations: from one point of a 6-dimensional object, we are picking one component and plotting it against the rotation number. A lot of information is missed during this process, but it is still useful to for a first analysis.

One check done to see if the families L1-Halo and L1-QV are the same is to pick two representatives with similar rotation number and plot them. A member of the family L1-Halo with rotation number $\rho =$ `3.4622727594120977` and a member of L1-QV with rotation number $\rho =$ `3.4623791625106679` are shown in Figure 4.15. Both orbits are different in size and position. It is interesing to see that the representative of the L1-Q1 family is a Halo-like orbit so, from a practical standpoint it is useful and could be a candidate for a mission. The main difference comes when the stability of these families is analyzed. Leaving aside the big real eigenvalue and its inverse and the unit eigenvalue with multiplicity two, it can be seen that they have differnt stability types. For example, Figure 4.16 shows the stability of the Halo family. The x-axis shows the rotation number, and the y-axis the absolute value of the eigenvalues. The majority of the eigenvalues are complex and have norm equal to one, with very few exceptions. On the other hand, following the same convention for the axes, Figure 4.17 characterizes the stabilty of the QV family, and it can be seen that it undergoes a bifurcation that changes its stability from elliptic to hyperbolic. Hence, the numerical experiments and data gathered in this study do not indicate that these two familes are connected, but it is important to remark that this is a local analysis, and hence the results are not conclusive.

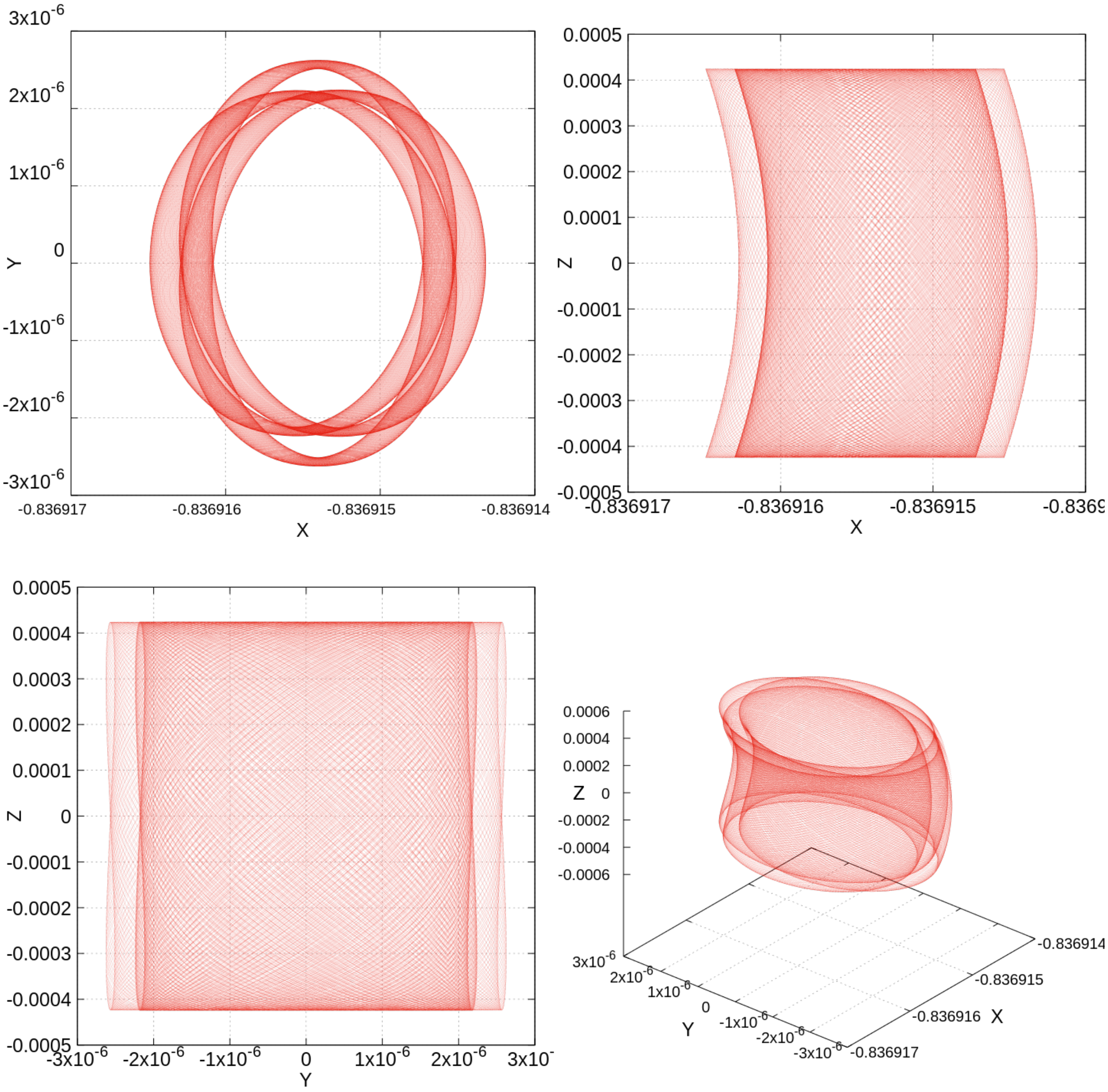

Figure 4.10: Example of small vertical torus around L_1.

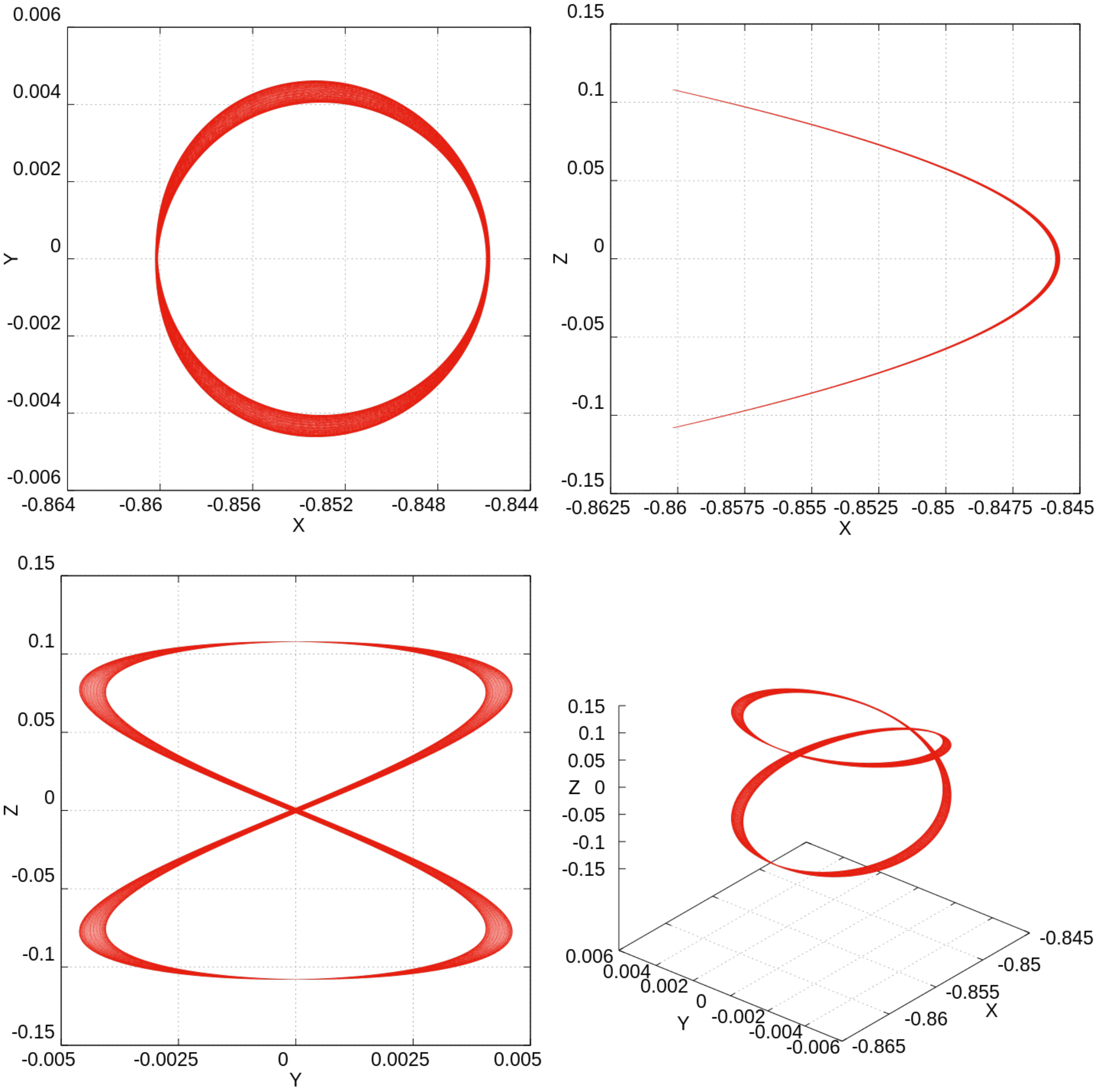

Figure 4.11: Example of medium vertical torus around L_1.

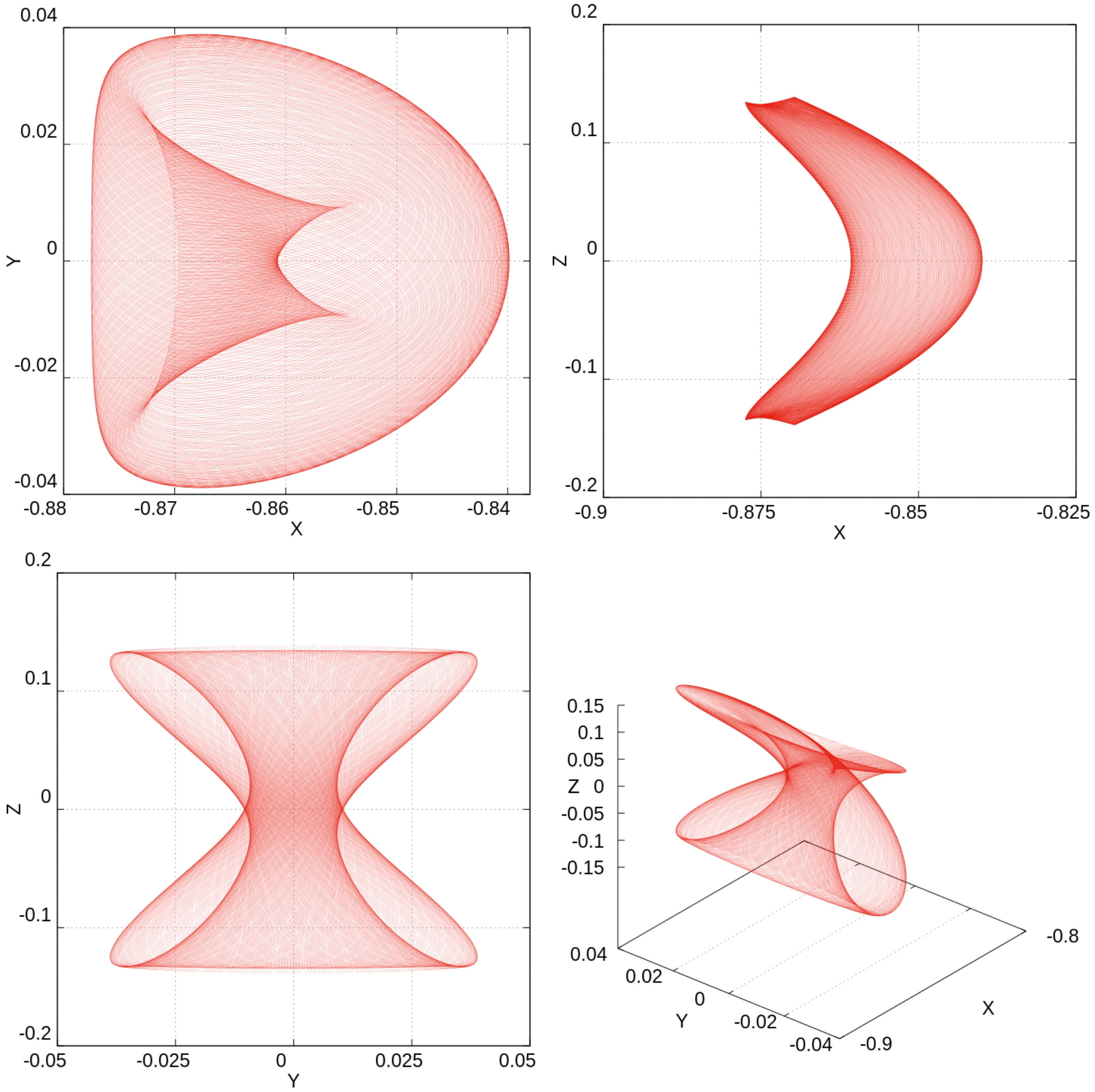

Figure 4.12: Example of a big vertical torus around L_1.

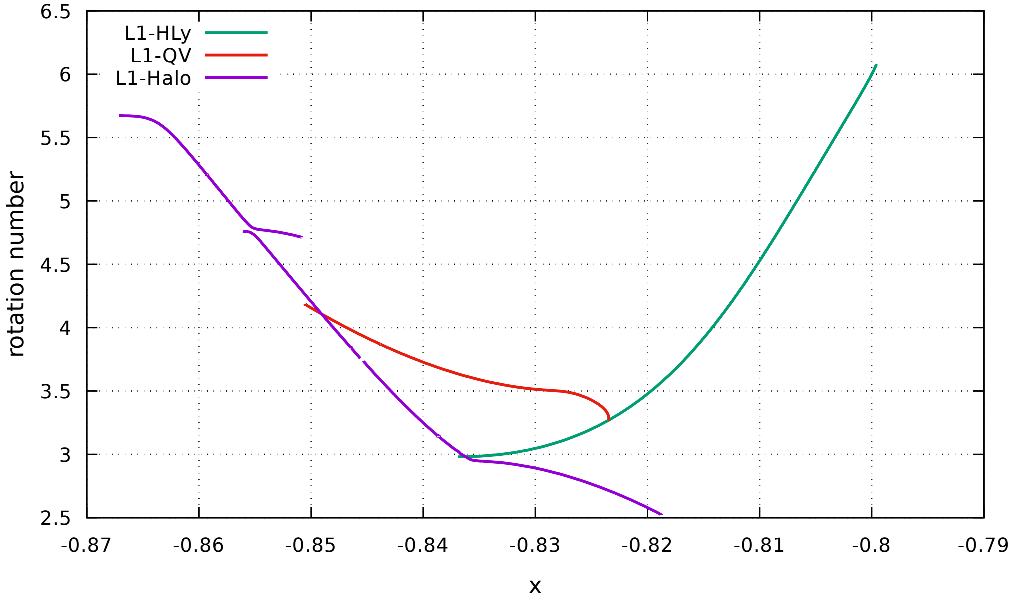

Figure 4.13: Families of 2D invariant tori in the QBCP around L_1. See text for details.

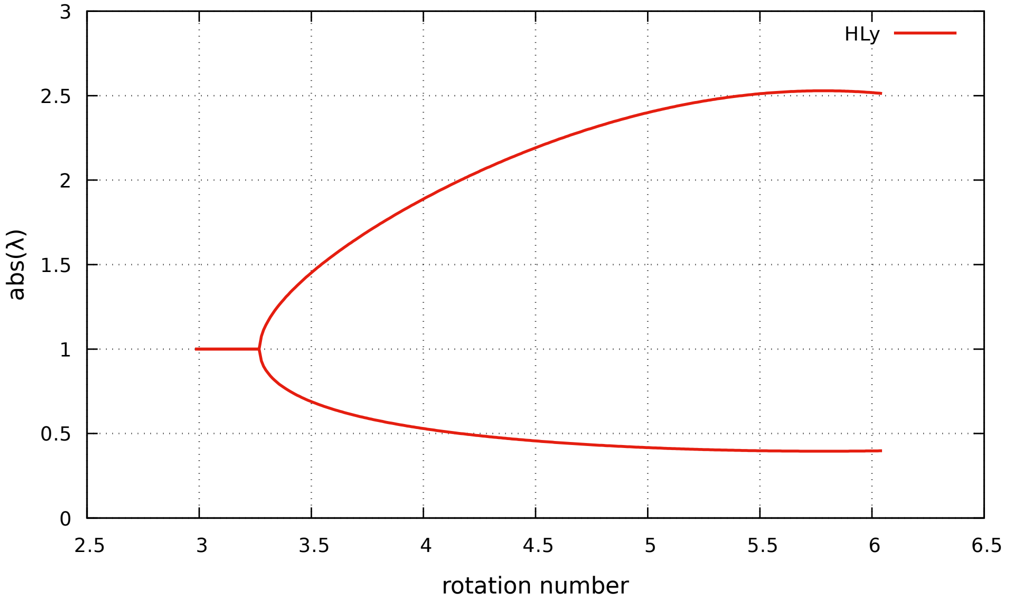

Figure 4.14: Stability of the horizontal Lyapunov family in the QBCP around L_1. See text for details.

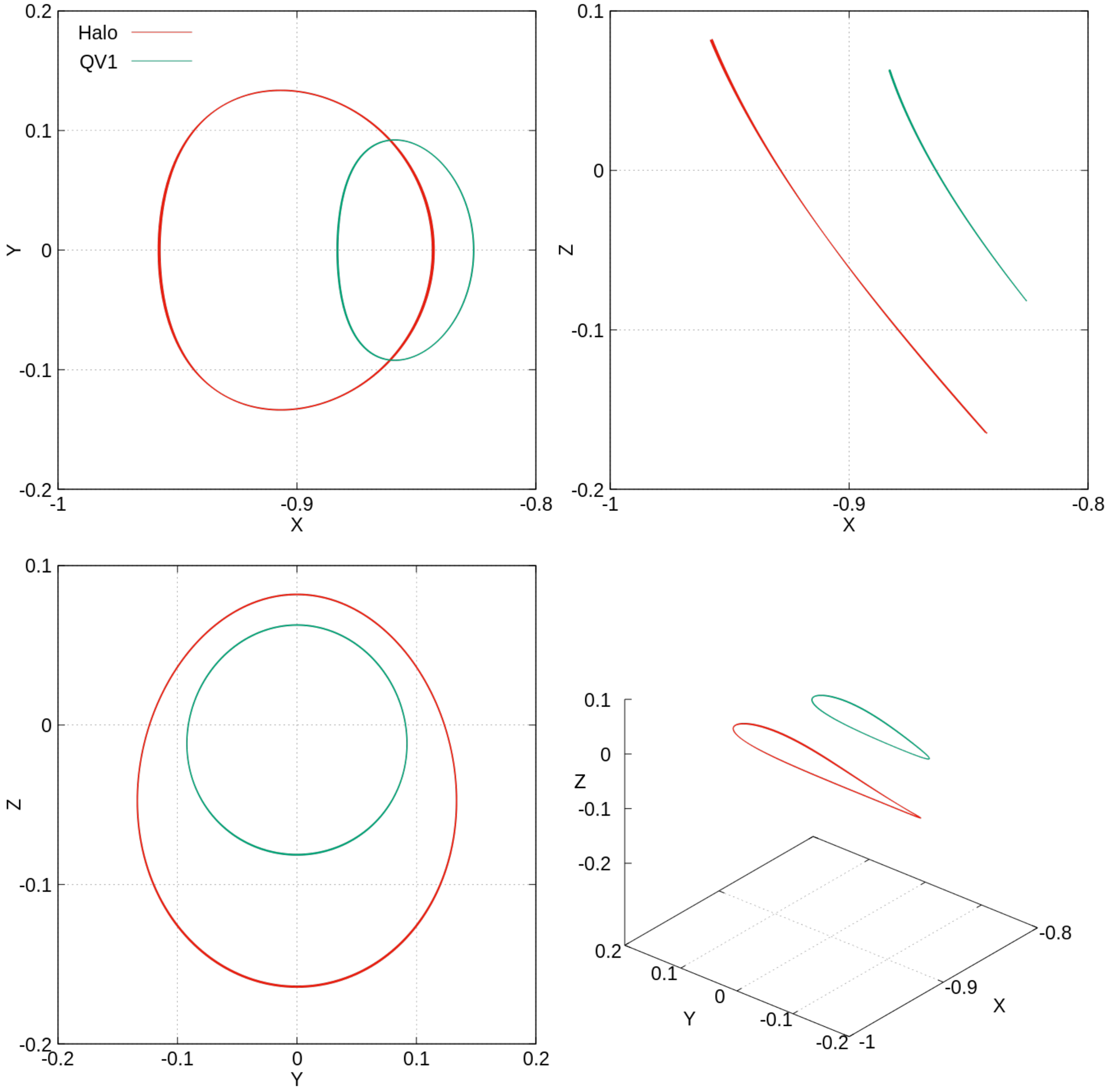

Figure 4.15: Example of representative of the Halo and QV families with similar rotation numbers. See text for details.

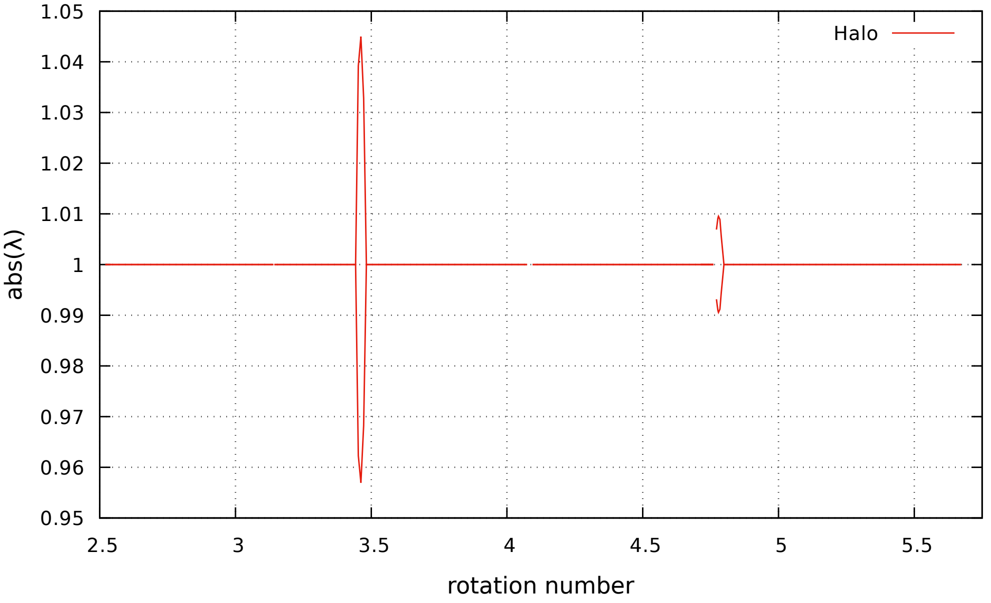

Figure 4.16: Stability of the Halo family in the QBCP around L_1. See text for details.

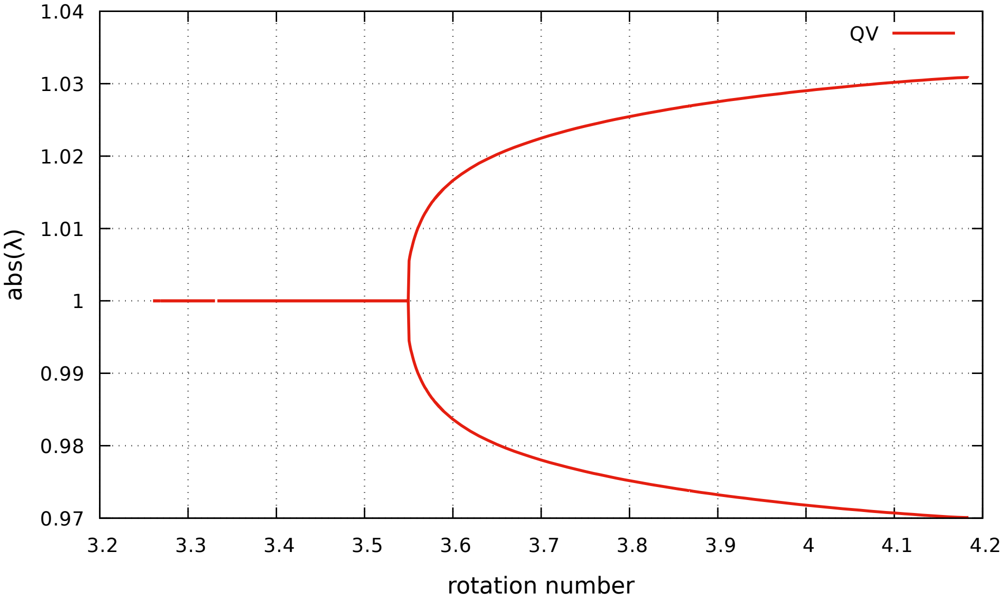

Figure 4.17: Stability of the QV family in the QBCP around L_1. See text for details.

4.3.2 Families around L_2

For the L_2 case, we start analyzing the vertical family. The starting point is again the dynamic equivalent of the L_2 point in the QBCP. This is, the periodic orbit that replaces the L_2 equilibrium point shown in Figure 4.1. By continuing along the vertical direction, the family of quasi-periodic orbits illustrated in Figure 4.18 is obtained. Like in the L_1 case, this family is the quasi-periodic counterpart of the vertical Lyapunov periodic orbits that appear in the RTBP.

The stability of these tori was also computed, and the results for the pair of eigenvalues that are not real or equal to one are shown in Figure 4.19. The x-axis is the rotation number, and the vertical axis is the argument of the eigenvalue. This pair of eigenvalues are complex with norm one, and Figure 4.19 shows how the argument evolves with respect to the rotation number. In this case it is observed that at the end of the family (rotation number $\rho \approx$ `-1.0179`) it seems that the two eigenvalues become real, leading to a change in the stability type. This may be the bifurcation observed in the Figure 4.6 from Section 4.2.2. For completeness, we mention that the large real eigenvalue starts at value on the order of 10^6, and decreases with the rotation number to a value on the order of 10^5.

As for the L_1 case is Section 4.3.1, we plotted some representatives of the family with different rotation numbers. starting from the beginning of the family, Figure 4.20 shows a torus with rotation number $\rho =$ `-0.4089841068128386`. This a torus very close to the reference periodic orbit, and its shape and size is influenced by it. Another example is illustrated in the in Figure 4.21. This example has as a rotation number $\rho =$ `-0.8717553068128412`. This case, a in the L_1 scenario, potrays an orbit that resembles those found in the RTBP, but under the influence of the periodic perturbation. Finally, the last example is a torus with rotation number $\rho =$ `-1.0173803068128409`. The same comments made for the L_1 case apply here.

The next step is to continue the family of planar tori. As in the L_1 case, other families were found, and are plotted together in Figure 4.23. Starting from a the reference orbit, we start continuing the family along the horizontal frequency to find a family of planar quasi-periodic orbits. This family is quasi-periodic counterpart of the planar Lyapunov that appear in the RTBP. Is it shown in read in Figure 4.23 and labeled as L2-HLy. Proceeding as in Section 4.3.1, we computed the stability of this family and found a bifurcation. This is shown in Figure 4.24, where a change of stability can be seen. From this bifurcation, a new family is born. This family was computed, and it is illustrated in Figure 4.24 as the purple curve labeled as L2-QV. This is the bifurcation obtained in the analysis of the center manifold from Section 4.2.2, and shown in Figure 4.7. Note that this bifurcation was also identified in [Andreu, 1998]. However, in [Andreu, 1998] three other small bifurcations were found. These were not noticed here, probably because the step-size used to continue the family was not small enough.

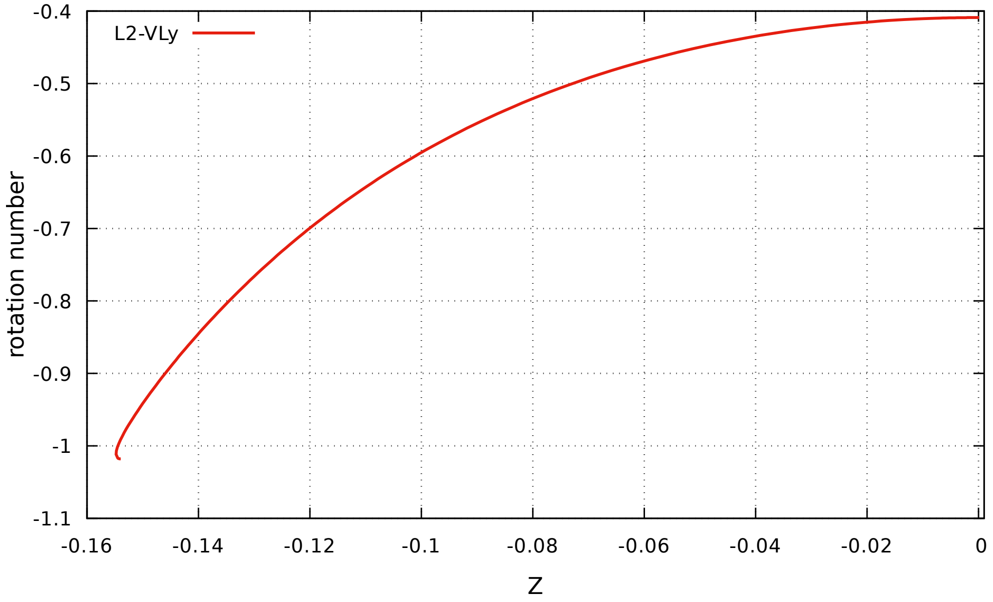

Figure 4.18: Quasi-periodic vertical Lyapunov family in the QBCP around L_2. See text for details.

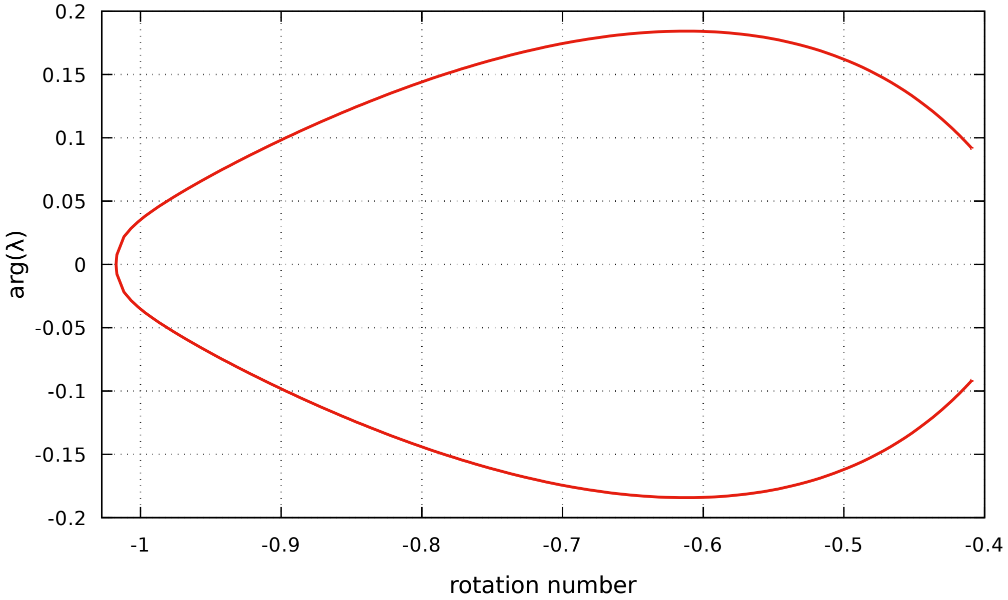

Figure 4.19: Stability of the quasi-periodic vertical Lyapunov family in the QBCP around L_2. See text for details.

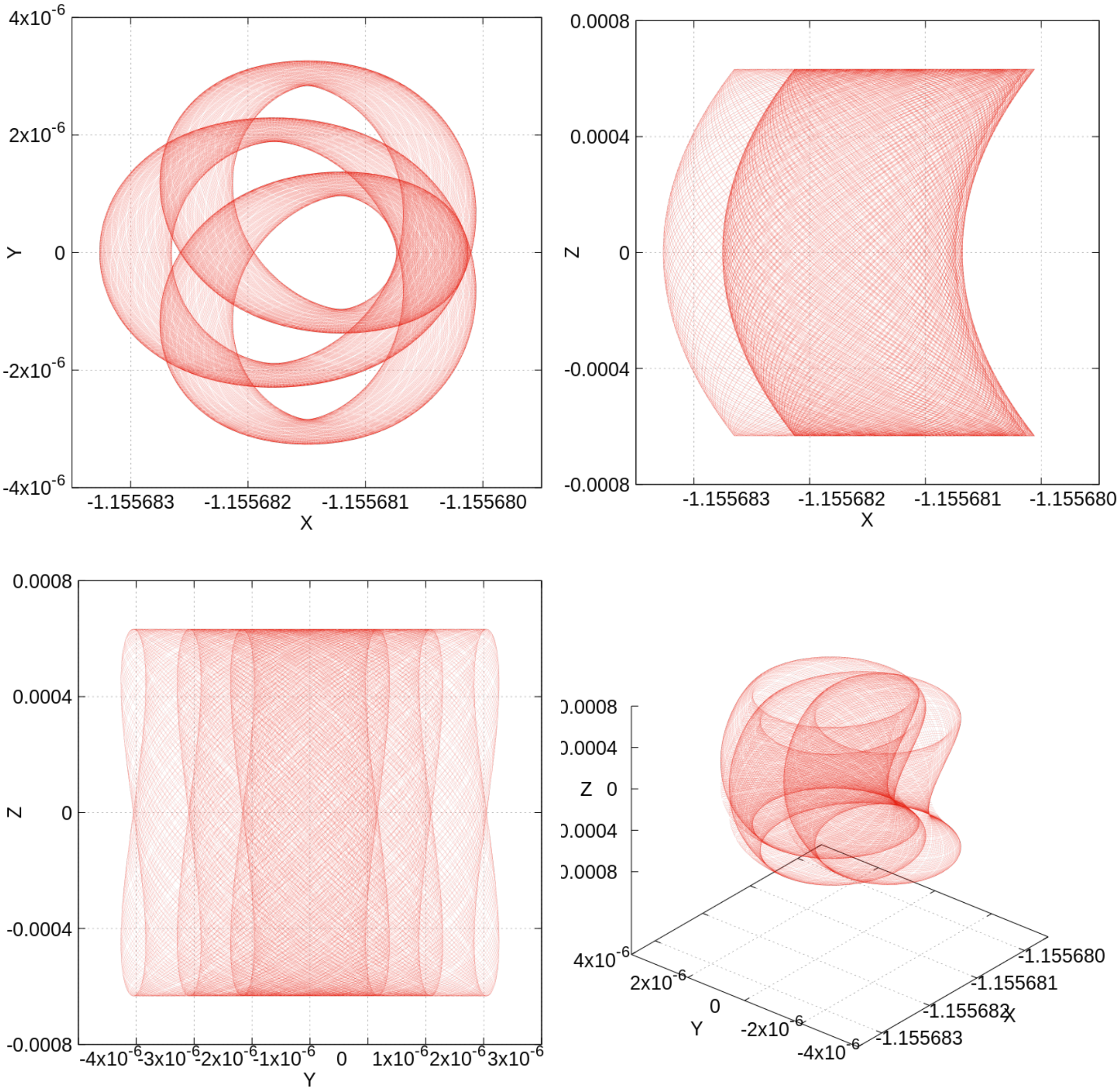

Figure 4.20: Example of small vertical torus around L_2.

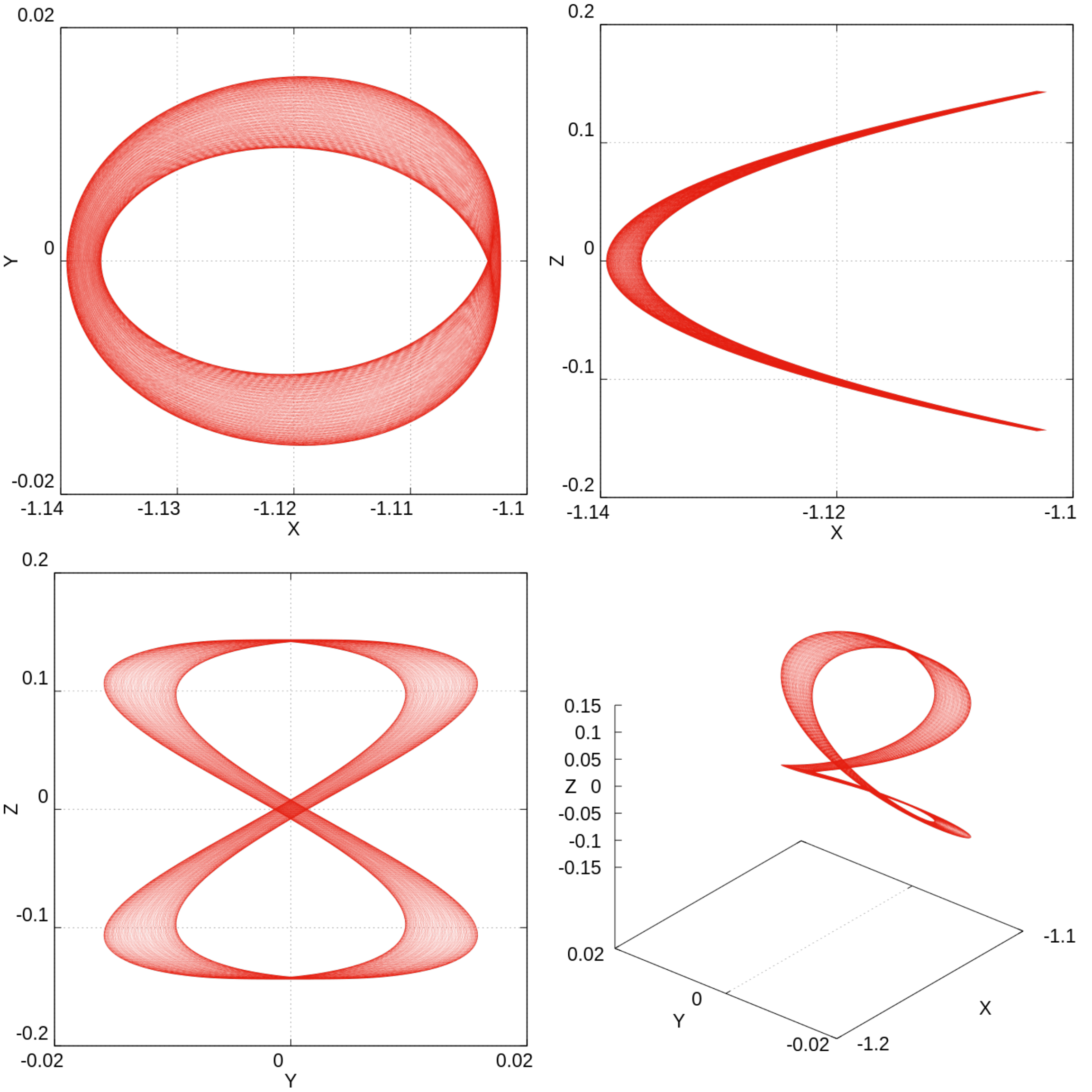

Figure 4.21: Example of medium vertical torus around L_2.

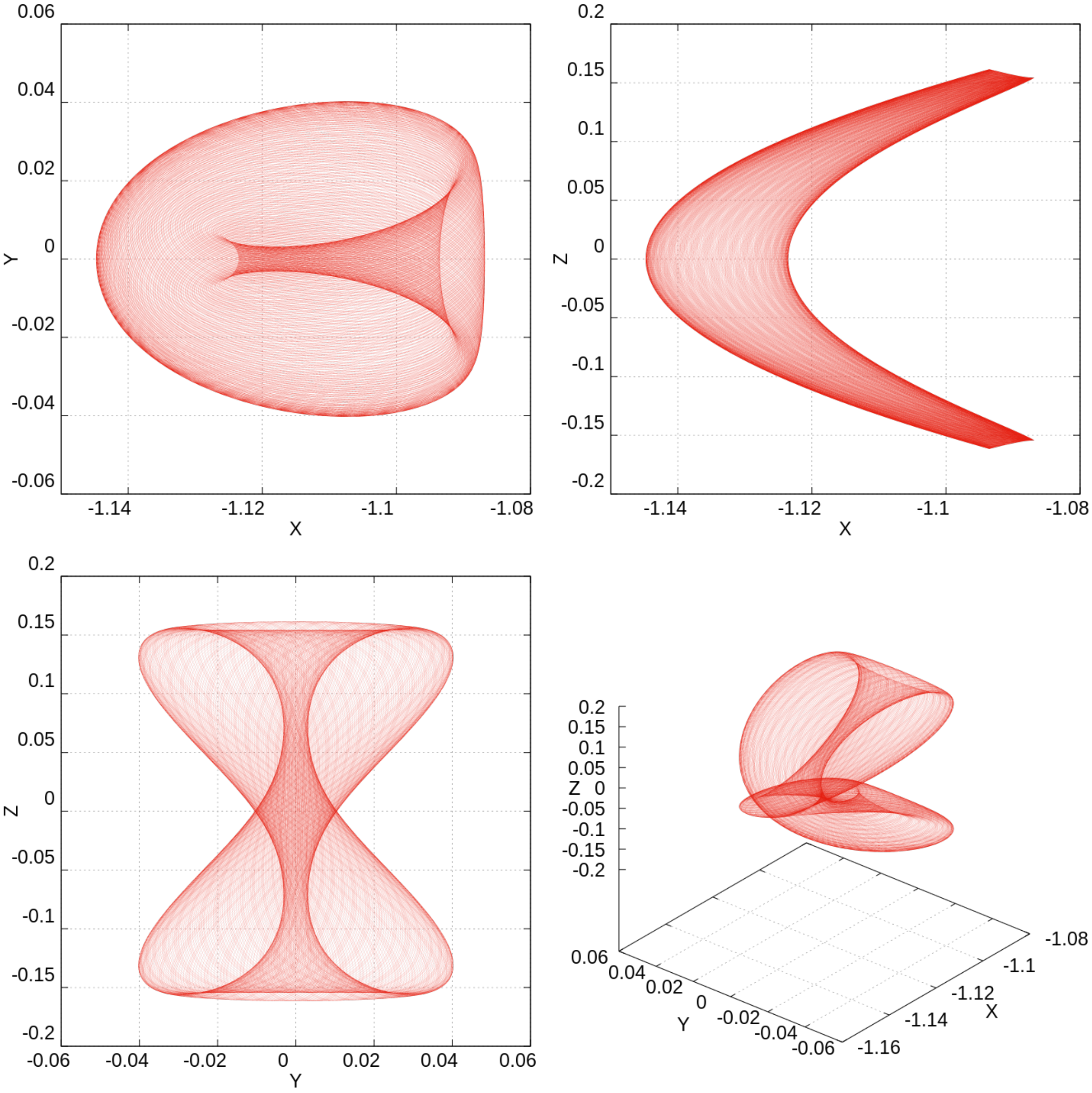

Figure 4.22: Example of big vertical torus around L_2.

Again, it is tempting to claim that the family L1-QV is the equivalent to the Halo family coming form the RTBP. Following the same previous argument made in Section 4.3.1, we continued an Halo orbit from the RTBP to the QBCP. Once in the QBCP, we continued the resulting torus to see how its evolves and to check for any connection with other families. The result of this continuation is the family plotted in Figure 4.23 in color green and labeled as L2-Halo.

Figure 4.25 is an amplification of the area around the bifurcation of the planar quasi-periodic Lyapunov orbits. There are two observations to be made: the first one is that the family L2-QV and L2-Halo are not connected. The second comment is that the L2-Halo family connects to another family of 2D tori resonant with the frequency of the Sun. This is seen around the point $(-1.12, -0.05)$ in Figure 4.25. This connection was conjectured in [Andreu, 1998], and the numerical evidence here seems to prove it.

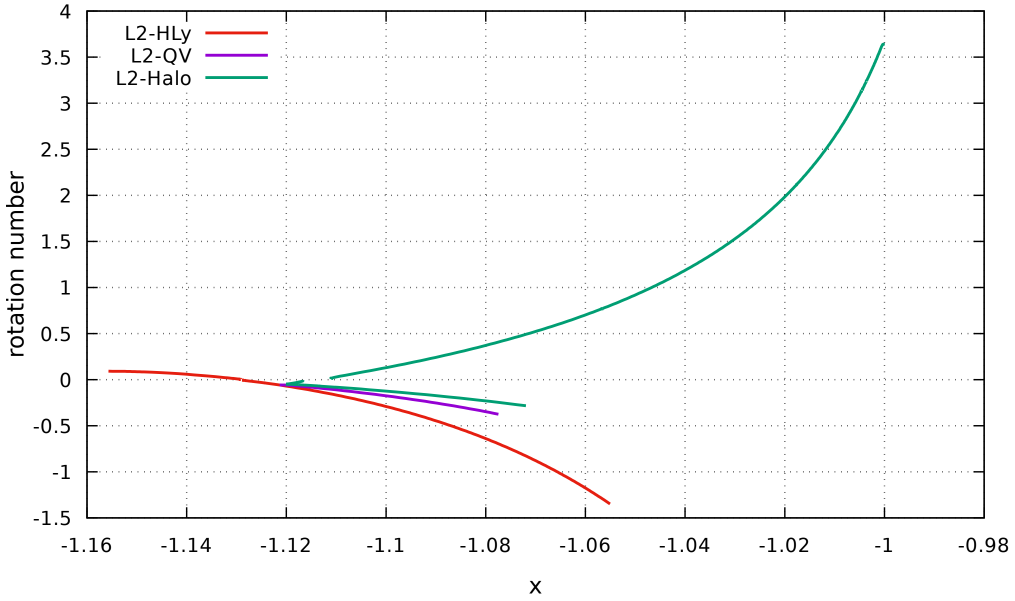

Figure 4.23: Families of 2D invariant tori in the QBCP around L_2. See text for details.

Now, let us show some examples of the different tori computed. Figure 4.26 shows three examples of orbits from the L2-Halo family. The rotation numbers are listed in Table 4.11.

Orbit	Rotation Number ρ
Blue	`-0.0480876152458433`
Red	`3.6403791158911880`
Green	`1.0224171606049586`

Table 4.11: Rotation numbers of the orbits plotted in Figure 4.26

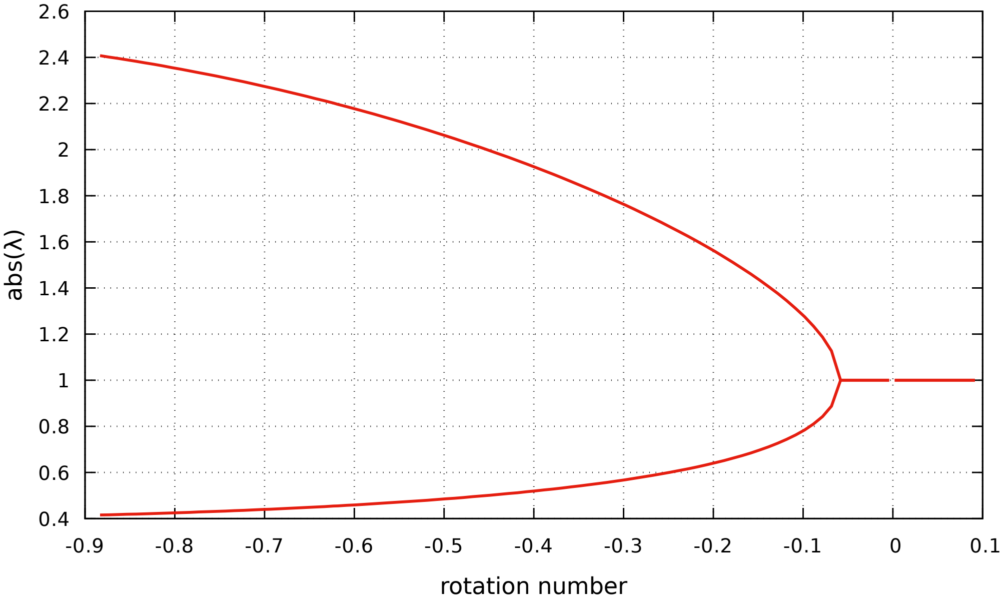

Figure 4.24: Stability of the quasi-periodic horizontal Lyapunov family in the QBCP around L_2. See text for details.

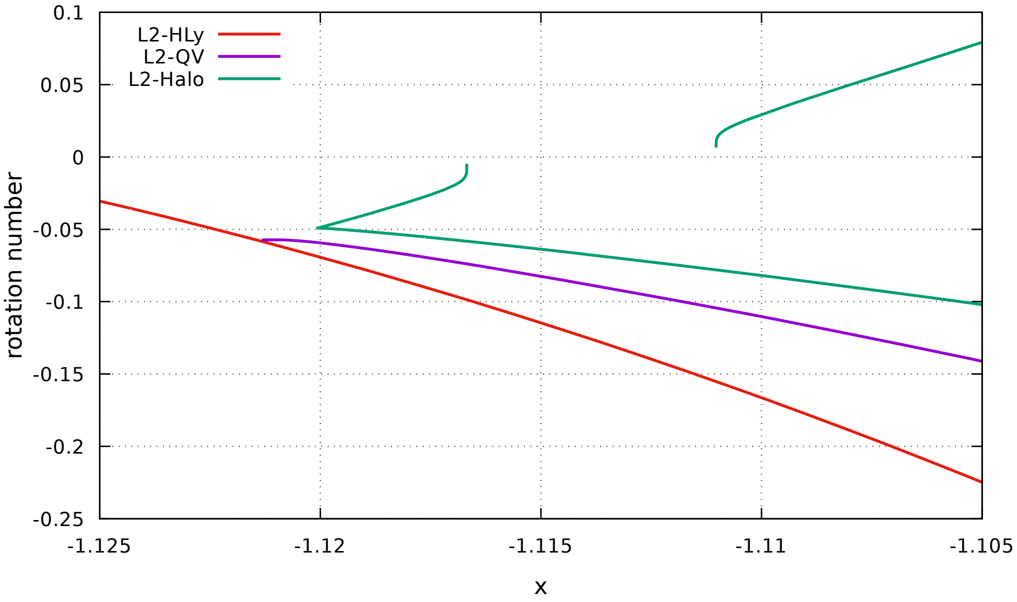

Figure 4.25: Families of 2D invariant tori in the QBCP around L_2. See text for details.

It can be seen that, as expected, the orbits in Figure 4.26 resemble the Halo orbits from the RTBP. An orbit from the Halo-L2 family with a rotation number close to the point where the family L2-Halo meets the family of 2D resonant tori was intentionally chosen for comparison purposes. A representative of the family of 2D resonant tori with rotation number $\rho =$ `-0.0774976152458405` is shown in Figure 4.27. It can be seen the L1-Halo is "thinner" than the 2D resonant torus from Figure 4.27. The end this short catalog of orbits, examples of two representatives of the L2-QV family are plotted in Figure 4.28 and Figure 4.28. The rotation numbers are $\rho =$ `-0.0721362180958642` for Figure 4.28 and $\rho =$ `-0.2449362180958645` for Figure 4.29. It can be seen that this family is not Halo-like.

Finally, the stability of the L2-Halo family and the 2D resonant tori family that continues from it, and L2-QV family has been computed. The results are plotted in Figure 4.30 and Figure 4.31. The x-axis is the rotation number, and the y-axis is the absolute value of the eigenvalues. It can be seen in Figure 4.30 that the tori from the L2-Halo family have an elliptical direction, with some small pockets of real eigenvalues. On the other hand, the stability for the L2-QV tori computed have all real eigenvalues, as shown in Figure 4.31. For both families, the other two eigenvalues are real, with a range between 10^2 and 10^6 for the L2-Halo family, and between 10^5 and 10^6 for the L2-QV family and the family of 2D resonant tori that meet the L2-Halo family.

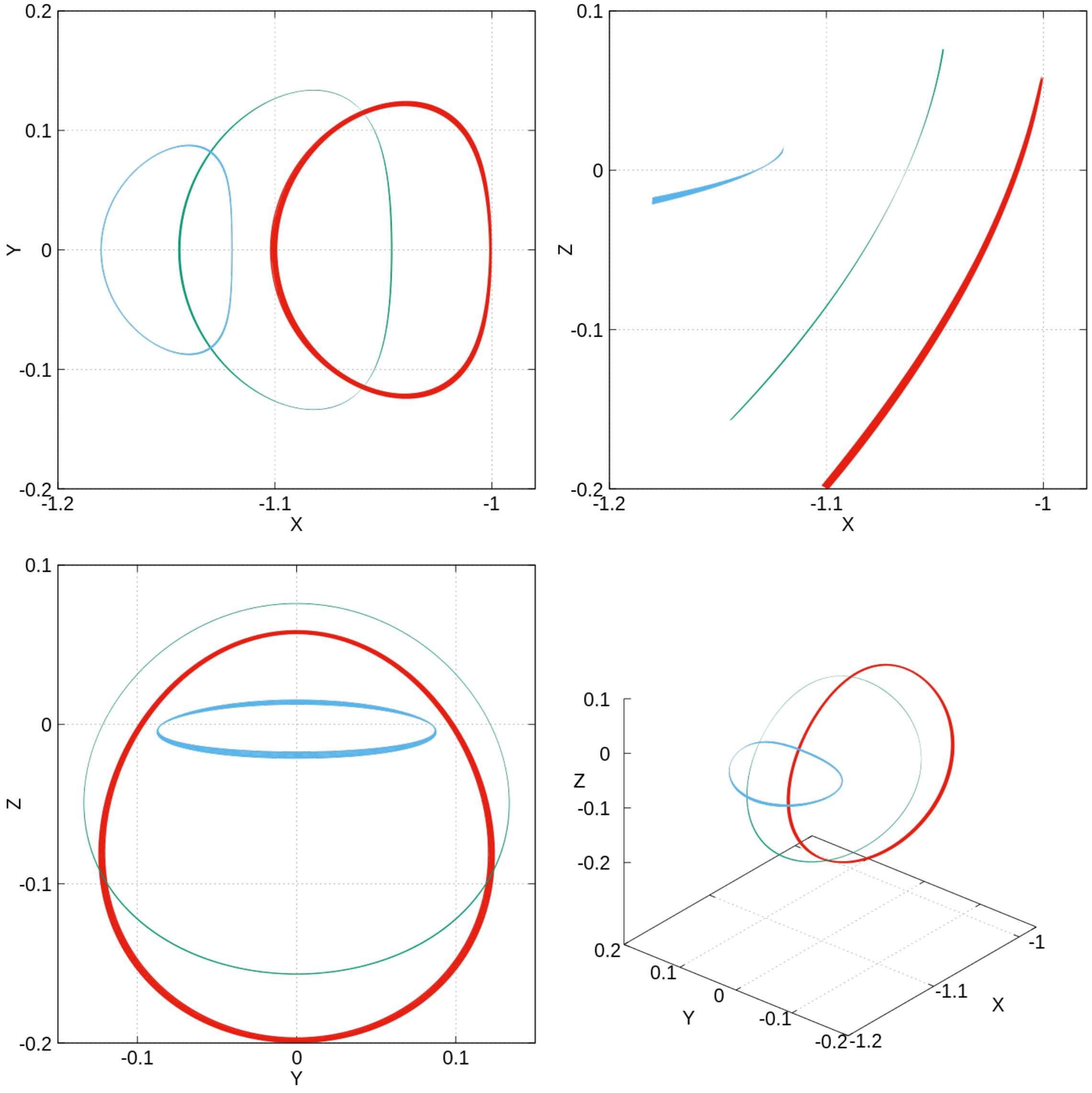

Figure 4.26: The representatives of the family L2-Halo. Rotation numbers are in Table 4.11. See text for details.

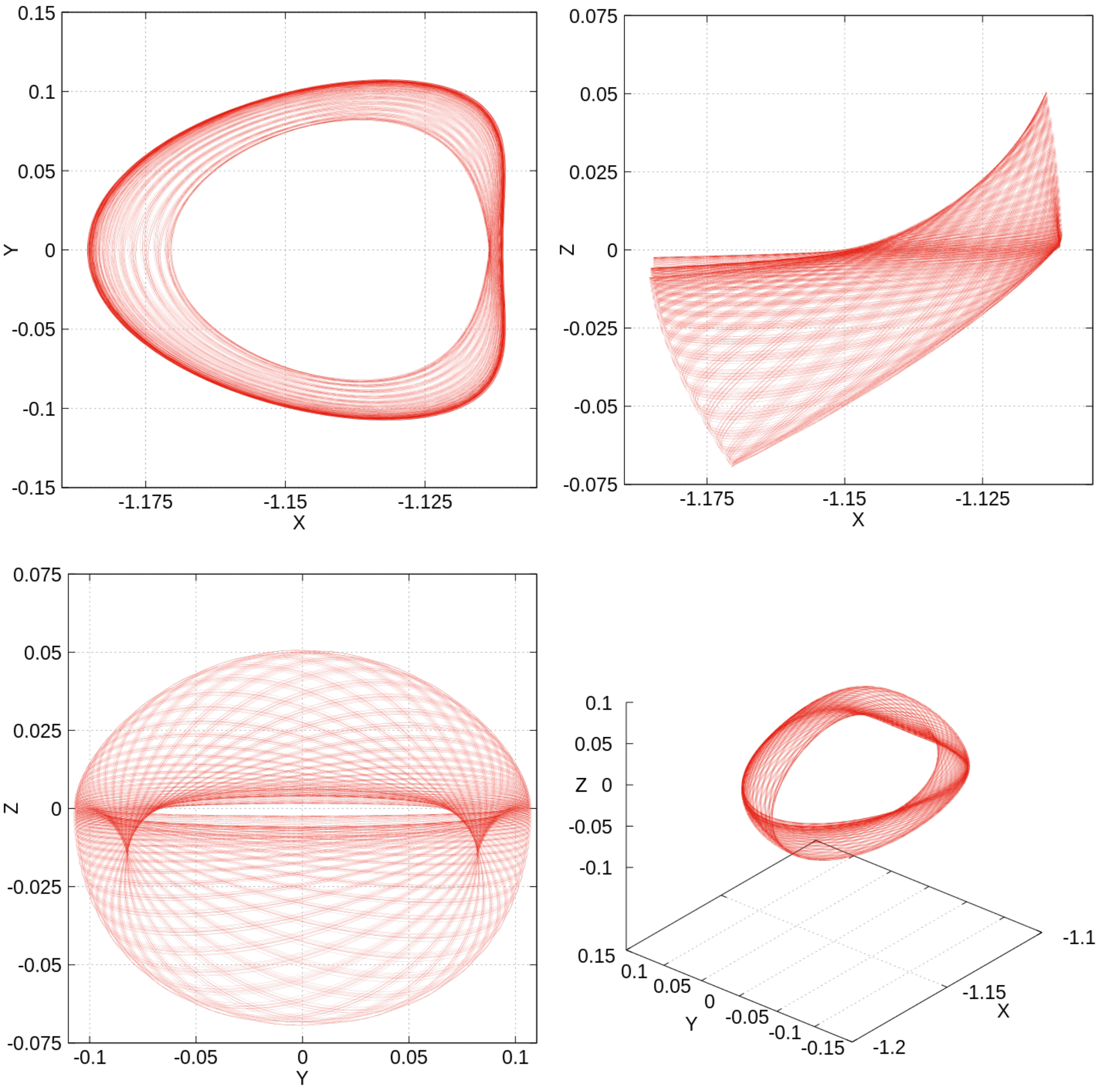

Figure 4.27: Representative of the family of 2D resonant tori that meet the L2-Halo family. See text for details.

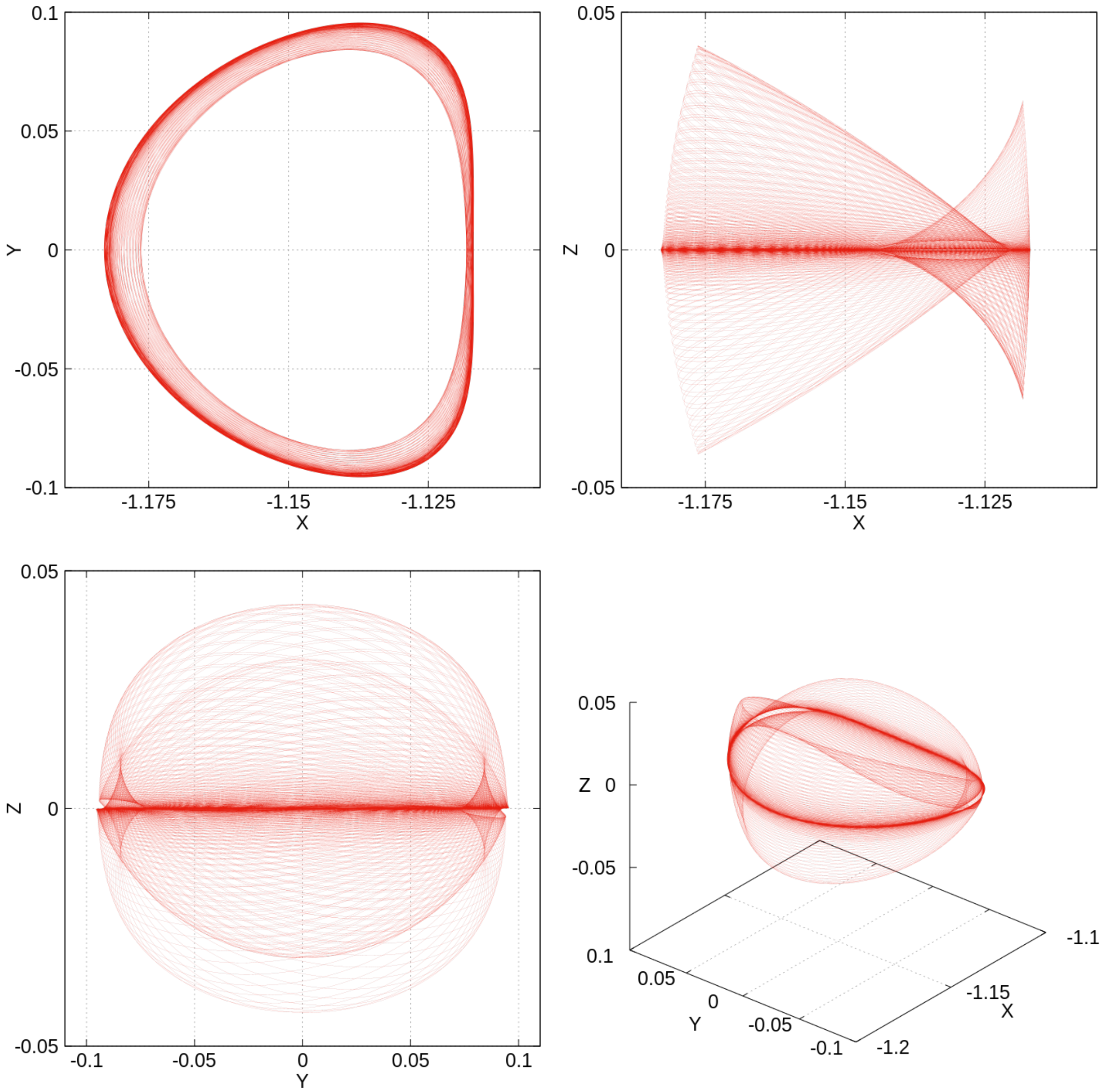

Figure 4.28: Representative of the QV family at the beginning of the family. See text for details.

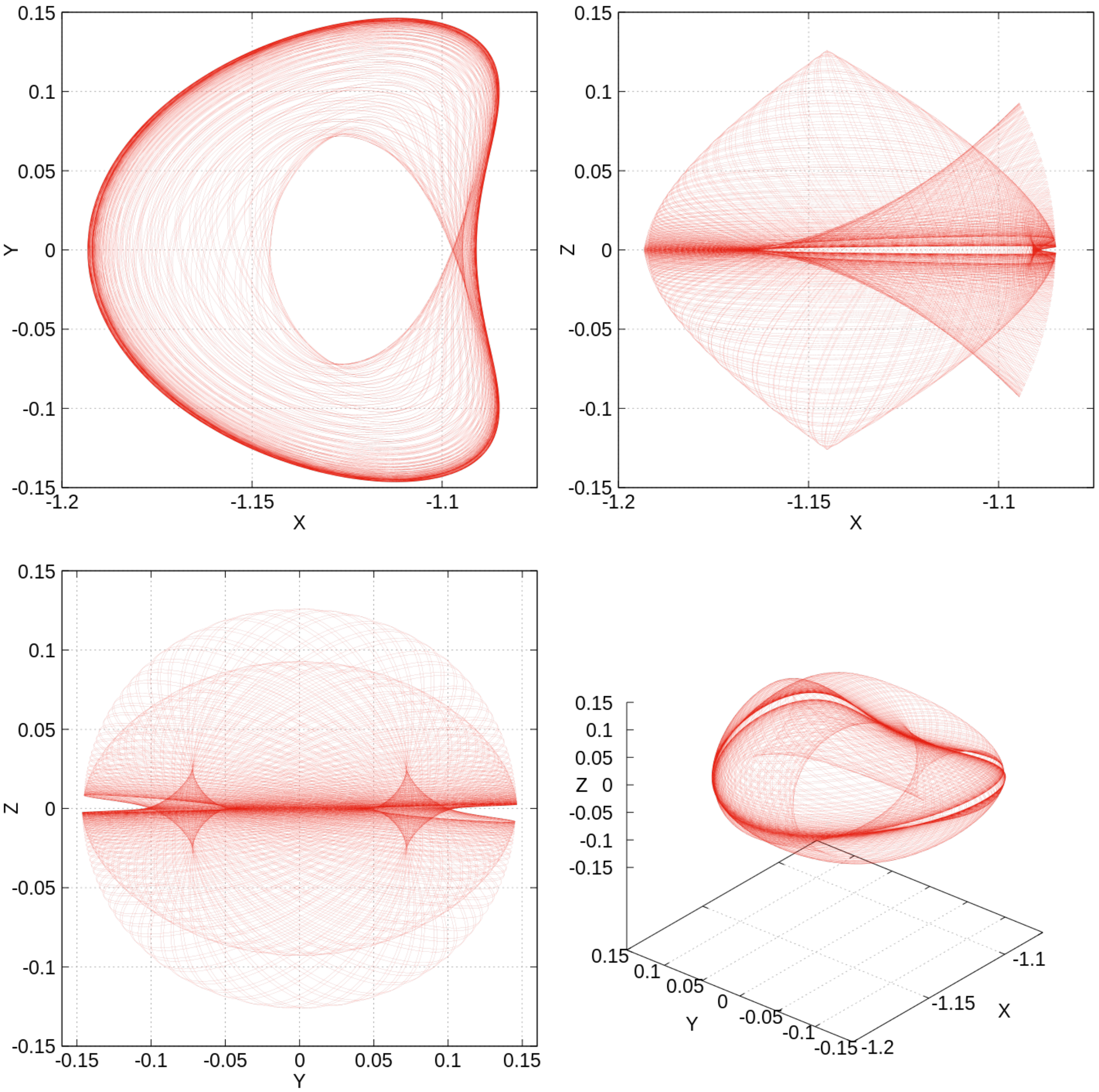

Figure 4.29: Representative of the QV family away from the bifurcation point. See text for details.

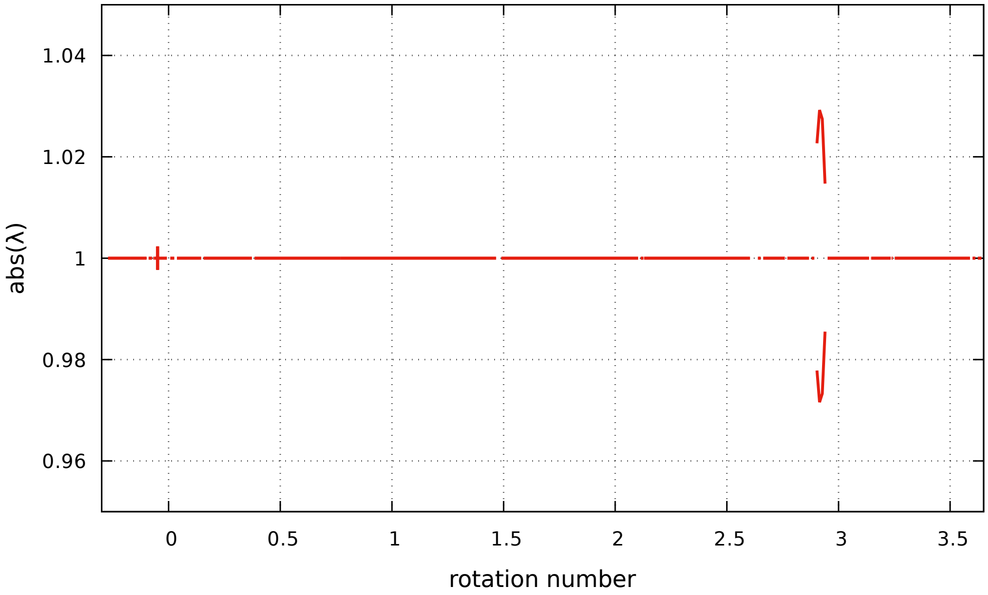

Figure 4.30: Stability of the Halo family in the QBCP around L_2. See text for details.

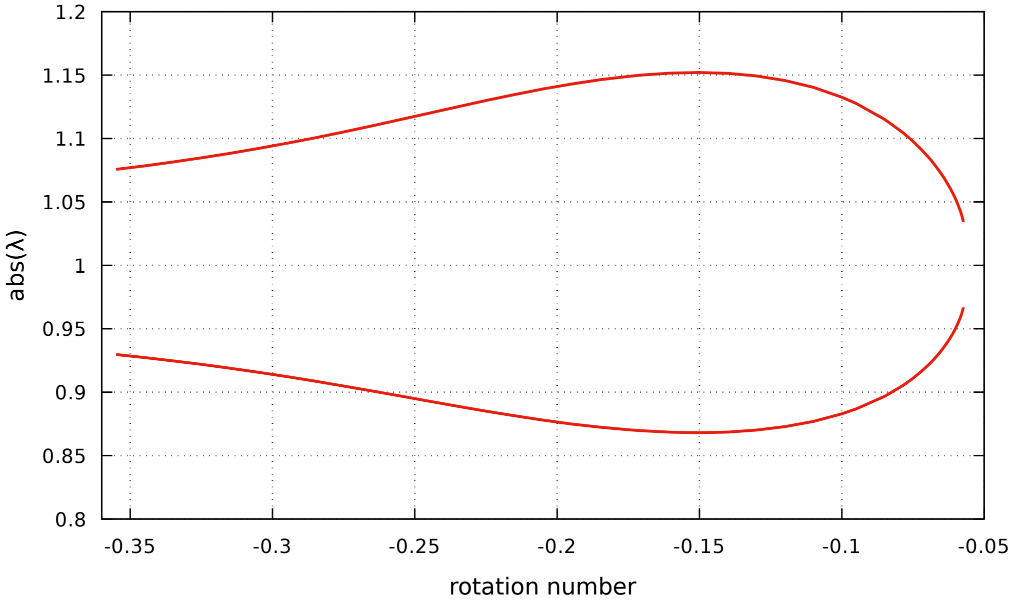

Figure 4.31: Stability of the QV family in the QBCP around L_2. See text for details.

Chapter 5

Transfers from the Earth to L_2 Halo orbits

In this chapter we study the use of invariant manifolds to transfer a spacecraft from a parking orbit around the Earth to a Halo orbit around the L_2 point of the Earth-Moon system in the context of the BCP model. The main result is that there exist one-maneuver transfers from a parking orbit around the Earth to a (quasi-periodic) Halo orbit around L_2, and that the total cost and total travel time of these maneuvers are in some cases consistent to similar approaches that require at least two maneuvers.

The use of the invariant manifolds to transport (and control) a spacecraft to a target orbit was first analyzed in [Gómez et al., 1985] and it has been extensively studied in the context of the RTBP for both the Sun-Earth system, and the Earth-Moon system. For the Sun-Earth system the use of the invariant manifolds is specially interesting because the stable manifold passes close to the Earth. In this case, a spacecraft in parking orbit can be inserted in the stable manifold of a target Halo orbit with only one maneuver. Once the spacecraft is in the manifold, it coasts to the orbit associated to that manifold with no need to perform extra maneuvers[4]. In the Earth-Moon system, unfortunately, this is not the case (see [Bernelli Zazzera et al., 2004, Alessi, 2010]). Different approaches have been developed for the Earth-Moon system, and these in general require two or more maneuvers. These approaches, along with representative references, are outlined in Section 5.1.

Some of the techniques described in Section 5.1, as well as the one presented here, require computing the invariant manifold associated to the target orbit to have a simple transfer. As mentioned before, this is not new. However, all the previous approaches computed the invariant manifold for periodic orbits. In the analysis present here, the target orbit is not periodic, but quasi-periodic. The computation of invariant manifold in the context of quasi-periodic orbits in presented is Section 2.4.

---

[4] This statement is valid from a theoretical point of view, where maneuver execution is perfect and instantaneous, the position and velocity of the spacecraft at the maneuver time is know with no error, and the spacecraft is considered massless. In practice, however, none of these assumptions are true, and usually it is required to perform small correction manuvers.

As mentioned in the first paragraph, one of the results discussed in this chapter is the existence of one-maneuver transfers from a parking orbit around the Earth to a (quasi-periodic) Halo orbit around L_2 in the BCP model. This is relevant because in the RTBP these connections do not exist. Also, recall that the BCP can be considered as a time-dependent perturbation of the RTBP, where the perturbation captures the direct gravitational effect of the Sun. Hence, the main takeaway is that the Sun, as modeled in the BCP, modifies the phase state of the RTBP to the point that connections between a vicinity of the Earth orbits around L_2 exist. Also, these connections are comparable in ΔV magnitude and transfer time to other techniques that use invariant manifolds to do transfers. The numerical experiments that provide details on the transfers, as well as comparisons with the other techniques are detailed in 5.2.

5.1 Approaches to compute transfers

In this section we review some of the main techniques to transfer a spacecraft from a parking orbit to Halo or Lissajous orbits around L_1/L_2. This is not meant to be an exhaustive review of the literature, but just a high level overview of the main approaches. These techniques have been divided in three groups, with a main focus on transfers from a parking orbit around the Earth to a Halo orbit around L_2[5]. These are summarized in the following paragraphs:

- Direct Transfer: This approach is a purely ballistic transfer, and it requires two maneuvers: one to leave the parking orbit, and the second one to insert the spacecraft in the target orbit. This approach requires in general an expensive maneuver to leave the Earth (approximately 3300-3500m/s), and a less expensive maneuver but still relatively big to insert into the Halo orbit (500-700m/s). The main benefit of this approach is that the time of travel spans between 4 and 13 days. Previous works that document this approach can be found in [Rausch, 2005, Le Bihan et al., 2014].

- Indirect Transfer: This approach uses the invariant manifold of the target Halo orbit to provide a low-cost transfer. The use of invariant manifolds has been proved to be useful in the Sun-Earth system, where the invariant manifolds get very close to the sphere of influence of the Earth. Hence, to insert a spacecraft from a parking orbit to the target orbit is relatively cheap. However, in the Earth-Moon system the invariant manifolds of the Halo orbits do not pass close to the Earth. In order to try to take advantage of the natural dynamics of the system provided by the invariant manifolds, in [Bernelli Zazzera et al., 2004] the authors develop an algorithm for the solution of the Lambert's three-body problem that leaves the transfer time free and tries to minimize the cost of the insertion maneuver in the invariant manifold. This is, they target a point in the invariant manifold that requires minimum fuel expenditure, and not its associated Halo orbit. Once in the invariant manifold, the spacecraft coast to

---

[5] The same argument applies to L_1, but for the sake of clarity, we focus our attention to L_2.

the target Halo orbit. The total cost of these transfers from a LEO orbit varies between 3100-3200m/s with a transfer time between 40 and 255 days. Another implementation of the use of invariant manifolds can be found in [Alessi, 2010, Mingtao and Zheng, 2010]. In [Alessi, 2010] the author computes transfers from a LEO orbit to a square Lissajous orbit around L_1 or L_2. The ΔV costs documented in [Alessi, 2010] are are also in the 3000-4000m/s range. It is worth noting that in [Alessi, 2010] the transfers from a LEO to a Lissajous around L_2 are not direct: first, the goal is to go to an orbit around L_1, and then using an heteroclinic connection to go to a target orbit around L_2. In [Mingtao and Zheng, 2010] the authors study indirect transfers to the L_1 libration point with a three-maneuver approach with a total cost of 3439.8m/s and a travel time of 22.9 days.

- Weak Stability Boundary (WSB) transfer: This approach involves considering the Sun-Earth-Moon-spacecraft 4-body system as two decoupled RTBPs, and was developed in [Belbruno and Miller, 1993]. Using the invariant manifold structures of the Lagrange points of the two RTBP, the authors show that it is possible to construct low energy transfer trajectories from the Earth to a Halo orbit about L_2 (see also [Koon et al., 2001]). This approach was successfully used to recover the Japanese mission Hiten in 1991. This method provides a fuel saving of around 18% with respect to the Direct Transfer method but with a penalty on the the total travel time, which varies between 80 and 120 days (see [Mingtao and Zheng, 2010]). See [García and Gómez, 2007] for remarks on the algorithmic definition of the WSB.

Note that all of the above approaches either are limited to the Earth-Moon RTBP, or consider the decoupled Sun-Earth RTBP and Earth-Moon RTBP. Thus, the contribution of the Sun's gravitational effect either is completely neglected, or it is considered only partially during specific parts of the transfer. As mentioned in the previous section, the approach taken in this thesis accounts directly for the effect of the Sun's gravity as modeled in the BCP model. The numerical experiments and the results are discussed in Section 5.2.

5.2 Case Study: transfers in the BCP

In this section we study the transfers from parking orbits around the Earth to three Type I Halo orbits, and three Type II halo orbits in the BCP. The only parameters fixed in the parking orbit are the semi-major axis and the eccentricity. The semi-major axis is set to be equal to the radius of the Earth, $R_E = 6400km$, plus 200km. We define R $= R_E + 200$. The eccentricity is set equal to zero. This is, we consider the family of circular orbits around the Earth traveling at approximately 200km above the Earth's surface. This family can be interpreted as a sphere with center in the center of the Earth, and radius equal to the radius of the Earth plus 200km. From now on, we will refer to this sphere as the LEO sphere.

Note that for practical applications we would also be concerned about the inclination of the parking orbit. Ideally, the inclination should be close to the latitude of a launching facility. For this analysis, this has been intentionally omitted given that the main focus is to study whether or not in the BCP the invariant manifold of the Halo-like orbits considered here intersect with the LEO sphere.

The approach is the following: given a target Halo-like orbit (Type I or Type II), an initial point on the unstable manifold is integrated forward in time. If the unstable manifold intersects the LEO sphere, then it is considered that there is a valid transfer. In that event, the ΔV between the parking orbit in the LEO sphere corresponding to the intersection point, and the corresponding point in the unstable manifold is computed. This gives an initial measure of the total ΔV transfer cost. The total transfer time Δt is also recorded, as well as longitude and latitude of the intersection point in the LEO sphere. The latitude gives a first approximation of the parking orbit inclination. The computation of the ΔV and Δt are given in synodical coordinates and physical units (km/s and days, respectively).

An important remark is that, for practical application, we are interested in the stable manifold; this is, trajectories that naturally converge towards the target orbit. Note that due to the symmetry of the system, the unstable gives us the same information: the stable manifold can be obtained from the unstable one by changing y for $-y$, and p_x for $-p_x$. Also, this symmetry also applies to the Type I and Type II orbits.

Recall from Section 2.4 that in order to get a local representation of the potential transfers, we consider two parameters: one, is a point on the invariant curve parametrized as a angle $\theta \in [0, 2\pi)$; and the second is a measure of the distance h to the invariant curve of a point $p_0^u(\theta)$ on the unstable manifold. This point is assumed to be closed enough to a point $\mathbf{x}(\theta) = (x(\theta), y(\theta), z(\theta), p_x(\theta), p_y(\theta), p_z(\theta))$ on the invariant curve such that it can be approximated as

$$p_0^u(\theta) = \mathbf{x}(\theta) + h\psi_u(\theta) + O(h^2) \tag{5.1}$$

where $\psi_u(\theta)$ is the eigenfunction associated to the unstable eigenvalue λ_u. The distance h is selected such that $|h| < h_0\lambda_u$, for a fixed $h_0 \in \mathbb{R}^+$, is small (for example, on the order of 10^{-6} or 10^{-7}). Note that h can be negative. Positive and negative values correspond to each of the two sides of the unstable manifold. From one on, we will refer as the *positive* (resp. *negative*) side of the manifold as the side generated with a $p_x > 0$ for $p_0^u(0)$, and a positive (resp. negative) value of h. As reference, the positive side is in the direction towards the Moon from the invariant curve.

These two parameters characterize the fundamental cylinder $[0, 2\pi) \times [h_0, h_0\lambda_u]$ of the invariant manifold defined in Section 2.4. Once we have defined the fundamental cylinder, we create a grid of N×N equispaced points in $[0, 2\pi) \times [h_0, h_0\lambda_u]$. The value of h_0 has been selected such that

$$\max_i \left(\|P_T(\mathbf{x}(\theta_i)) - \mathbf{x}(\theta_i + \rho) - h_0\lambda_u\psi_u(\theta_i + \rho)\|\right) < \delta, \quad \theta_i = \frac{2\pi \cdot i}{N}, i = 0, ..., N-1$$

where $P_{T_s}(\mathbf{x}(\theta))$ is the stroboscopic map at time T_s, T_s is the period of the Sun in the normalized frame, and ρ is the rotation number of the associated invariant curve. For this analysis we used $N = 2000$ and $\delta = 10^{-6}$.

Then, we integrate forward in time along the unstable manifold, and check whether or not the unstable manifold intersects with the LEO sphere. Also, we check collisions with the Moon, and for trajectories that leave the sphere of influence of the Earth/Moon system. For the latter, we stop the integration if the distance to the Earth/Moon barycenter exceed as any point during the integration 6 units of distance in the normalized frame. This is equivalent to approximately 2.3 millions of kilometers. Of course, we also need to set a maximum integration time. For this analysis, the maximum integration time was set to $6T_s$. This corresponds to approximately 191.5 days of physical time. We acknowledge that this number is somehow arbitrary, but it is justified in the sense that are looking for reasonable transfer times.

As summary, we chose a point close to the invariant curve that lives on the unstable manifold, integrate forward in time and look for the following four events:

1. The unstable manifold intersects the LEO sphere
2. The unstable manifold collides with the Moon
3. The unstable manifold leaves the sphere of influence of the Earth/Moon system; this is, the distance of the computed state to the Earth/Moon barycenter, exceeds 6 times the distance of the Earth to the Moon.
4. After 6 units of time in the normalized frame, none of the above occur (these will be referred as wandering trajectories)

For this analysis we have chosen three Type I and three Type II quasi-periodic Halo orbits around L_2 in the BCP and run the process described in the above paragraphs. The projections of the invariant curves of the three Type I orbits are shown in Figure 5.1. These are referred as IC11 (green), IC12 (blue), and IC13 (red). The three corresponding of the Type II are in Figure 5.2. These are labeled as IC21 (green), IC22 (blue), and IC23 (red) Note that the invariant curves IC21 and IC23 in Figure 5.2 are very close to each other. These were intentionally chosen to assess the sensitivity in the transfers with respect to the distance of target orbits. The Table 5.1 and Table 5.2 contain the rotation number associated to each of the trajectories selected and the unstable eigenvalues.

Table 5.1: Type I invariant curves characteristics

Invariant Curve	rotation number	λ_u
IC11	3.239814740891185	1407.242345974658
IC12	1.658983813333736	19619.97458514797
IC13	0.645906459334160	179352.0342756758

The results of the analysis are shown in Figure 5.3 and Figure 5.4. The color code is the following: red corresponds to those trajectories on the unstable manifold that intersect with the LEO sphere; green captures the collisions with the Moon; yellow the trajectories that scape the Earth/Moon sphere of influence; and black the trajectories that do not meet any of the previous criteria. The horizontal axis corresponds to the angle associated to a point on the invariant curve. The vertical axis corresponds to the signed height of the

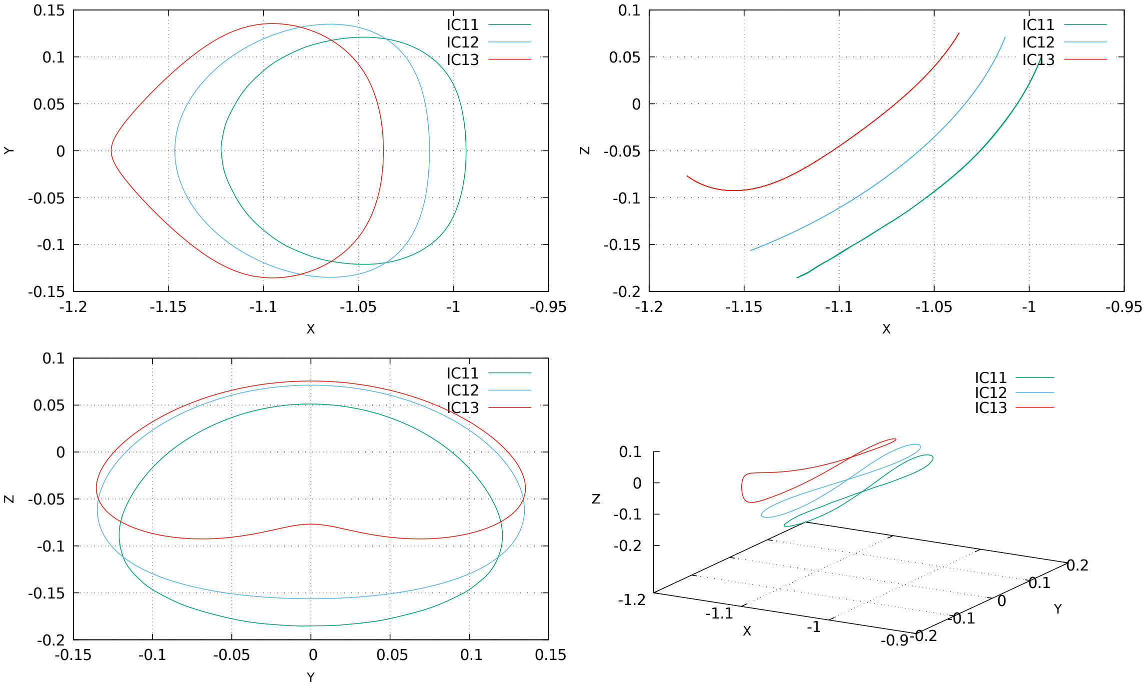

Figure 5.1: Invariant curves for Type I orbits

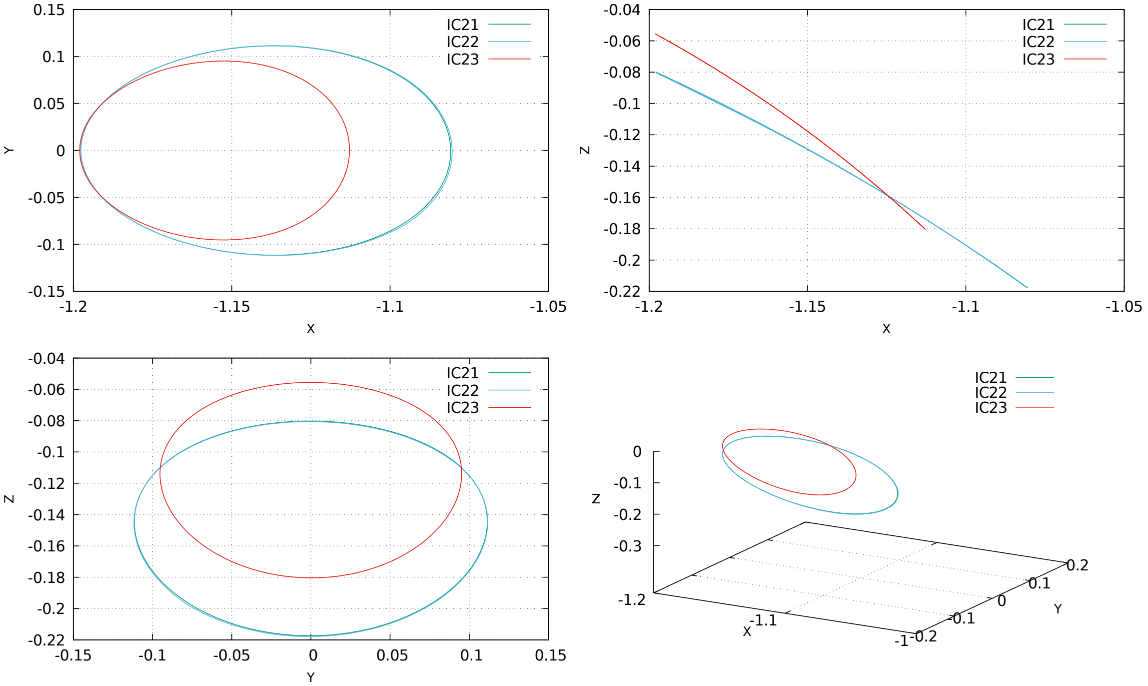

Figure 5.2: Invariant curves for Type II orbits

Table 5.2: Type II invariant curves characteristics

Invariant Curve	rotation number	λ_u
IC21	3.097097182626015	24082.25237481578
IC22	3.128958892611009	23104.95771489475
IC23	2.085220044971505	93487.30771525634

fundamental cylinder, where the sign denotes the side of the manifold. As a general comment that applies to both Figure 5.3 and Figure 5.4, notice that all figures are periodic with respect to the horizontal axis (this is, the left side of the plot coincides with the right side). About the vertical axis note that, by construction, the bottom and top rows are related by the stroboscopic map at time equal to the period of the Sun, T_s. For the sake of clarity, let's consider the positive side of the manifold. The bottom row corresponds to the trajectories obtained fixing $h = \min([h_0, \lambda_u h_0]) = h_0$, and changing the angle $\theta \in [0, 2\pi)$. The top row corresponds to the trajectories associate to $h = \max([h_0, \lambda_u h_0]) = \lambda_u h_0$, where λ_u is the eigenvalue corresponding to the unstable component of the hyperbolic part. By construction, the top row is the image of the bottom row by the stroboscopic map. With that, it would be expected the top row to be equal to the bottom one plus a shift equal to the rotation number of the invariant torus under consideration (see, for example, [Jorba and Nicolás, 2020]). Looking at Figure 5.3 and Figure 5.4 this is clearly not the case. The reason is that we are using a total integration time equal to $6T_s$, and this is relatively short. Using a short integration time has the following effect: when we integrate an initial condition on the unstable manifold at distance h_0 from the invariant curve, we check for events that happen in that period of time (intersection with the LEO sphere, collision with the Moon, escape, or none of the previous). When we repeat this process for the initial conditions of the top row, we know that these are the image of the initial conditions of the bottom row. In other words, is as if we have already integrated a total of T_s units of time. Hence, the results of the top row are the same as if we integrated $7T_s$ units of time the initial conditions of the bottom row. This may cause that the events we observe are different for the bottom and top rows. If we were to integrate an infinite (or a large enough) amount of time, we would observe that shift.

The first row in Figure 5.3 contains the results for the invariant curve IC11, the second row for the invariant curve IC12, and the third one for the invariant curve IC13. The first column is the negative side of the unstable manifold, and the second one the positive side. For both the positive and negative sides of the manifold, the distance from the invariant curves as defined in at the beginning of this section (this is, the value $h_o\lambda_u$) is equal to 3×10^{-7} units of distance in the normalized coordinates (or approximately 115m in physical units) for IC11 and IC12, and equal to 4×10^{-7} units of distance in the normalized frame (or approximately 150m in physical units) for IC13.

It is observed that in all cases except of the IC11, positive side case, there are small regions (colored in red) where the unstable manifold intersects the LEO sphere. For the IC11, positive side case, there are also connections via the unstable manifold, but there are not clearly perceived in the image. In all cases the dominant outcomes are either when the particle leaves the Earth/Moon sphere of influence (colored in yellow) or it follows a wandering trajectory for the timespan integrated (colored in black). In all cases there are also collisions with the Moon (regions colored in green), although in some cases is barely noticeable. It is in the cases IC12 and IC13, positive side in both cases, where there are large regions where the unstable manifold collides with the Moon. (Recall that the positive side of the manifold is the one oriented towards the Moon.) It also noted that the closest the target orbit is to the Moon, the more collisions exist (in this order, for farthest to closest: IC11, IC12, and IC13).

The scenario for the Type II trajectories is captured in Figure 5.4. The first row contains the results for the invariant curve IC21, the second row for the invariant curve IC22, and the third one for the invariant curve IC23. As for the Type I case, the first column is the negative side of the unstable manifold, and the second one the positive side. The distances from the invariant curves in this case are 10^{-6} units of distance in the normalized frame (or approximately 3.8km in physical units) for IC21, 5×10^{-7} units of distance in the normalized frame (or approximately 190m in physical units) for IC22, and 7×10^{-7} units of distance in the normalized frame (or approximately 270m in physical units) for IC23. In all cases these values are for both the positive and negative sides of the manifold.

In this case, there are very few transfers that intersect with the LEO sphere, and these are barely noticeable in the figures. For the case of the invariant curves IC21, IC22, and IC23, there are almost no trajectories of the unstable manifold that intersect the LEO sphere. In the negative side there are small regions where the trajectories collide with the Moon, while in the positive side there are quantitatively more (again, this is the side oriented towards the Moon). Most of the trajectories, either leave the Earth/Moon's sphere of influence, or wander around during the total time of the integration.

For each one of the cases analyzed, the transfers that minimize three different cost functions have been computed. These three cost functions are, as mentioned before:

- $J_1(\theta, h) = \Delta V(\theta, h)$
- $J_2(\theta, h) = \Delta t(\theta, h)$
- $J_3(\theta, h) = \sqrt{\Delta V(\theta, h)^2 + \Delta t(\theta, h)^2}$

When doing this analysis, it is important to define how the ΔV was computed, and what is meant by “transfer time” and it was calculated. The total ΔV was computed the same way as in [Alessi, 2010]. This is, if $\hat{\mathbf{v}}$ is velocity of the spacecraft when it intersects with the LEO sphere, the first step is to convert this vector from conjugated momentum to synodic velocity. Let us call this velocity $\mathbf{v}$. Note that in theory we should also convert this velocity from the rotating frame to the inertial frame. However, because this transformation does no change the module of the vector, we can skip it. With that, the ΔV is computed as follows:

$$\Delta V = \sqrt{\|\mathbf{v}\|^2 + v_s^2 - 2\|\mathbf{v}\| \cos(\frac{\pi}{2} - \beta)} \tag{5.2}$$

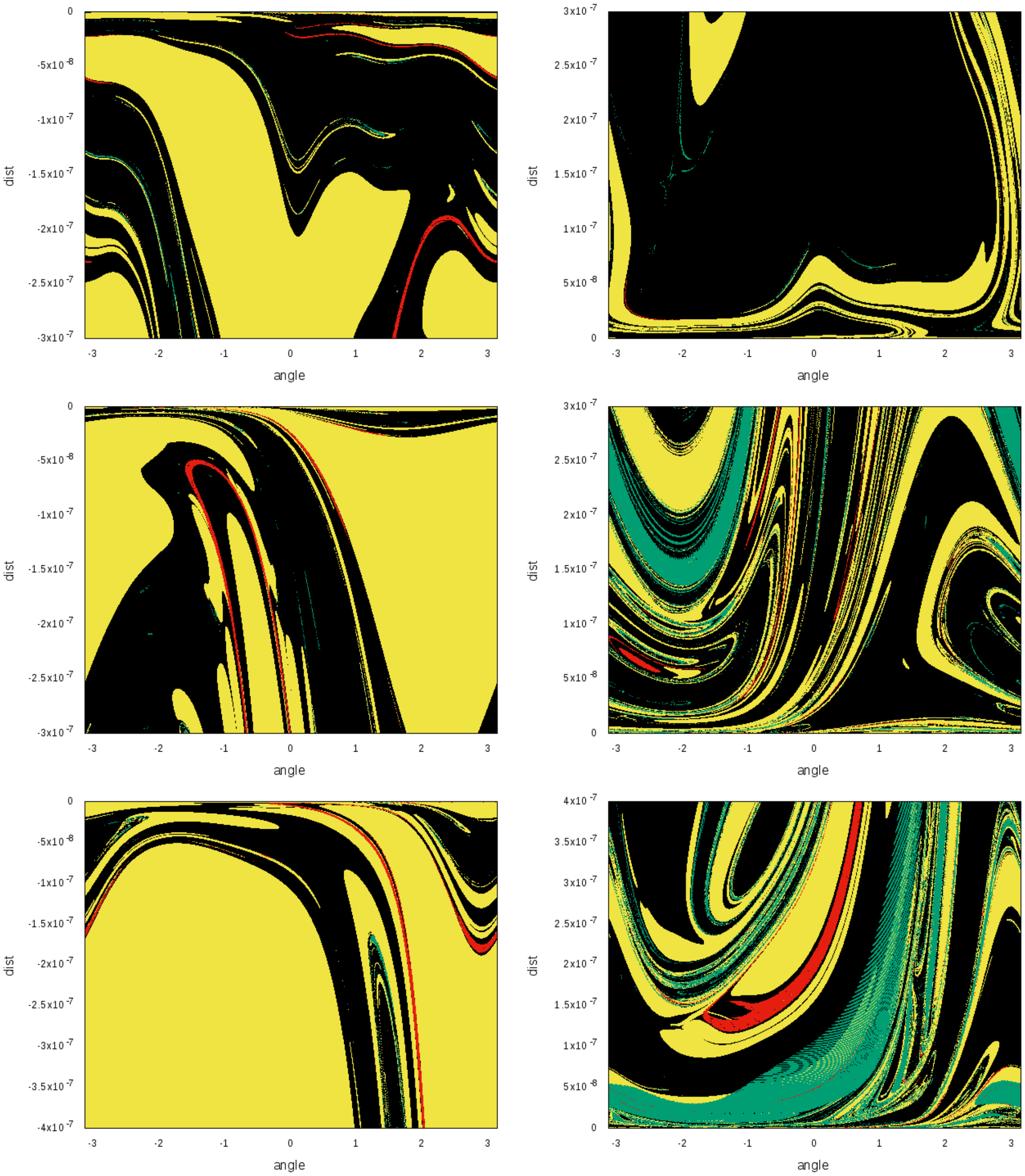

Figure 5.3: Fundamental cylinders for Type I orbits. Valid transfers are colored in red, trajectories where a particle leaves the Earth/Moon system are colored in yellow, collisions with the Moon are green, and none of the previous cases in black. See text for details.

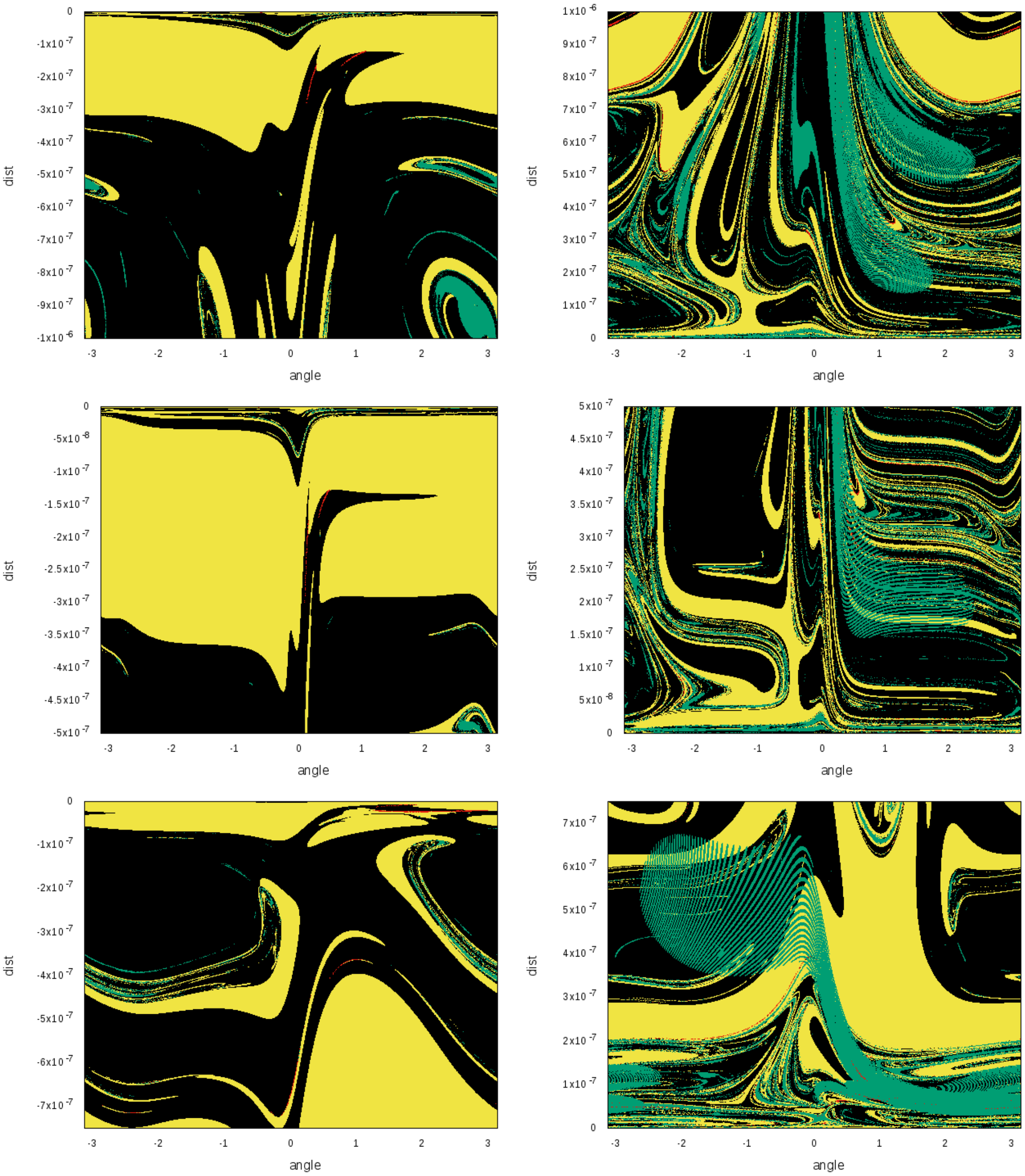

Figure 5.4: Fundamental cylinders for Type II orbits. Valid transfers are colored in red, trajectories where a particle leaves the Earth/Moon system are colored in yellow, collisions with the Moon are green, and none of the previous cases in black. See text for details.

where β is the angle between the velocity vector $\mathbf{v}$ and the normal to the LEO sphere. The value v_s is the module of the velocity of a circular orbit on the LEO sphere, and it is computed using the *vis-viva* equation:

$$v_s = \sqrt{\frac{1-\mu}{R}}$$

Note that close to the biggest primary (the Earth), we assume 2-Body Problem dynamics.

The computation of the total transfer time is a matter of convention. Note that, in theory, if we follow stable manifold, the total time to arrive to the invariant curve is infinite. This is because the stable manifold tends asymptotically to the invariant curve. However, for practical purposes we define a threshold such that if we are below it, we consider the transfer completed. This threshold is (within reason) arbitrary, and it is typically based on the distance to some reference object. In our case the reference object is the invariant curve, and we have chosen a distance equal to $D = 100$km as a threshold. The next question is how to estimate time t_D at which the particle will be a distance D to the invariant curve. This is not as straightforward as, let's say, a point in space where computing the distance is not difficult. The approach we took is to estimate the time t_D is to use the linear flow in a vicinity of the invariant curve. Let

$$\bar{\lambda} = \frac{\log \lambda_u}{T}$$

This value $\bar{\lambda}$ is the eigenvalue associated to the flow around the invariant curve, and it a measure of the rate at which, locally, an initial condition close of the invariant curve departs (if $\bar{\lambda} > 0$), or approximates (if $\bar{\lambda} < 0$) it with respect to time. We model the distance to the invariant curve with the following linear differential equation:

$$\begin{cases} \dot{x} = \bar{\lambda} x \\ x(0) = h \end{cases} \tag{5.3}$$

where x is the approximate distance to the invariant curve, and h is the initial distance to the invariant curve as defined as in Equation (5.1). Fixing the distance D, and knowing the initial distance h, Equation (5.3) can be solved, and the time t_D computed. This is:

$$t_D = \frac{1}{\bar{\lambda}} \log\left(\frac{D}{h}\right)$$

Hence, if T is the total time of integration from the distance h to the invariant curve, and t_D the time to reach a distance equal to D, the total transfer time Δt is defined as follows:

$$\Delta t = T - t_D$$

This is the time reported in the rest of the section with, again, a value of $D = 100$km.

The results for each case, for a parking orbit traveling 200km above the Earth's surface, are summarized in the Table 5.3 for Type I orbits, and in Table 5.4 for Type II orbits. The first column of Table 5.3 and Table 5.4 states the invariant curve associated to the target orbit, the second column is the manifold side (positive/negative), the third the cost function minimized, the fourth and fifth columns the ΔV and the total transfer time Δt associated to the cost function, and the last column the latitude of the intersection point in the LEO sphere.

Table 5.3: Transfer cost to Type I Halo orbits

Invariant Curve	Manifold Side	Cost Function	ΔV (km/s)	Δt (days)	Latitude (deg)
IC11	+	J_1	3.2669	142.0661	13.439409
IC11	−	J_1	3.1641	138.3457	12.037744
IC11	+	J_2	4.0805	141.6628	-5.295561
IC11	−	J_2	3.2158	118.6235	1.816246
IC11	+	J_3	3.5347	141.9145	1.483374
IC11	−	J_3	3.2158	118.6235	1.816246
IC12	+	J_1	3.1970	124.5192	-7.529808
IC12	−	J_1	3.2180	122.3772	8.693360
IC12	+	J_2	6.4304	113.8526	11.245034
IC12	−	J_2	4.3185	112.5306	-28.175822
IC12	+	J_3	6.4304	113.8526	11.245034
IC12	−	J_3	4.3185	112.5306	-28.175822
IC13	+	J_1	3.1734	110.3284	-3.869638
IC13	−	J_1	3.1617	141.6146	-5.502472
IC13	+	J_2	3.2671	110.3107	-7.639184
IC13	−	J_2	3.3344	100.2958	7.040290
IC13	+	J_3	3.1734	110.3284	-3.869638
IC13	−	J_3	3.3344	100.2958	7.040290

Looking at the results in Table 5.3 it is observed that the cheapest transfer in terms of ΔV corresponds to the case {IC13, –, J_1} (meaning: IC13 invariant curve, negative side of the invariant manifold, and J_1 cost function) with a total of 3.1617km/s. This transfer, however, takes almost 142 days to reach the target orbit. In terms of total transfer time, the cheapest corresponds to the cases {IC13, –, J_2} and {IC13, –, J_3} with slightly over 100 days. For this option, the total cost terms of ΔV is 3.3344km/s, making this transfer very reasonable. It is a good idea to look at other options that are a trade-off between a cheap maneuver and a reasonable transfer time. In these category, we have the cases {IC13, +, J_1}, and {IC13, +, J_3}, where the total ΔV cost is 3.1634km/s, and the total travel time is around 110 days. This provide a saving of around 161m/s at the expense of an increase in travel time of approximately 100 days. Another important aspect is the latitude at the LEO sphere. In all the cases, the latitude are below 7.1 degrees, which is a reasonable value.

The study of transfers for Type II Halos is captured in Table 5.4. In this scenario, the case {IC23, –, J_1} is the cheapest transfer in terms of ΔV with a total of 3.1231km/s, and a

Table 5.4: Transfer cost to Type II Halo orbits

Invariant Curve	Manifold Side	Cost Function	ΔV (km/s)	Δt (days)	Latitude (deg)
IC21	+	J_1	3.1841	161.5869	5.645610
IC21	−	J_1	3.2668	152.9112	-8.222948
IC21	+	J_2	5.1727	127.4293	-24.409394
IC21	−	J_2	3.3851	144.9792	-18.574485
IC21	+	J_3	4.3772	127.8258	-31.131620
IC21	−	J_3	3.3851	144.9792	-18.574485
IC22	+	J_1	3.4450	170.1543	-0.049602
IC22	−	J_1	3.2184	153.3855	5.282887
IC22	+	J_2	8.9775	132.5925	66.012057
IC22	−	J_2	3.5173	145.8660	-22.626341
IC22	+	J_3	5.3619	133.2474	13.593364
IC22	−	J_3	3.5173	145.8660	-22.626341
IC23	+	J_1	4.1184	122.0862	-17.195273
IC23	−	J_1	3.1231	132.0245	9.329800
IC23	+	J_2	6.0772	121.4934	27.102303
IC23	−	J_2	4.1081	104.1051	-11.507359
IC23	+	J_3	3.1744	124.6729	-7.456677
IC23	−	J_3	4.1081	104.1051	-11.507359

total transfer time of around 132 days to reach the target orbit. The shortest transfers in this case are {IC23, –, J_2} and {IC23, –, J_3}, with a total transfer time of approximately 104 days, but with a total ΔV cost of more than 4.1km/s. As the in the case for the Type I case, we can look for trade-offs. However, after looking at the data, it seems that the option that minimizes the total ΔV is the best, given the low latitude intersection with the LEO sphere, and how the total transfer time compares with the other options.

Overall, and as a main takeaway, it can be concluded that there are transfers in the BCP comparable in total ΔV and transfer time with other techniques such as the Indirect Transfer or WSB, but with the main advantage that only one maneuver is required.

Let us have a closer look at the IC13 case. Figure 5.5 shows the trajectory followed by the transfer {IC13, –, J_2}. This trajectory corresponds to the stable manifold of the target orbit IC13; this is, is the trajectory that a spacecraft would follow after departing from the Earth to the target orbit. It can be seen that the trajectory circles twice the Earth and the Moon before converging to the target orbit. This phenomena is similar to what is observed when the equilibrium point around L_2 in the RTBP is continued to the BCP, where the resulting periodic orbit circles twice (geometrically defined) L_2 point. This 'bending' of the invariant manifold is due to the direct gravitational effect of the Sun.

Figure 5.6 shows different zoomed projections of the transference to the target orbit.

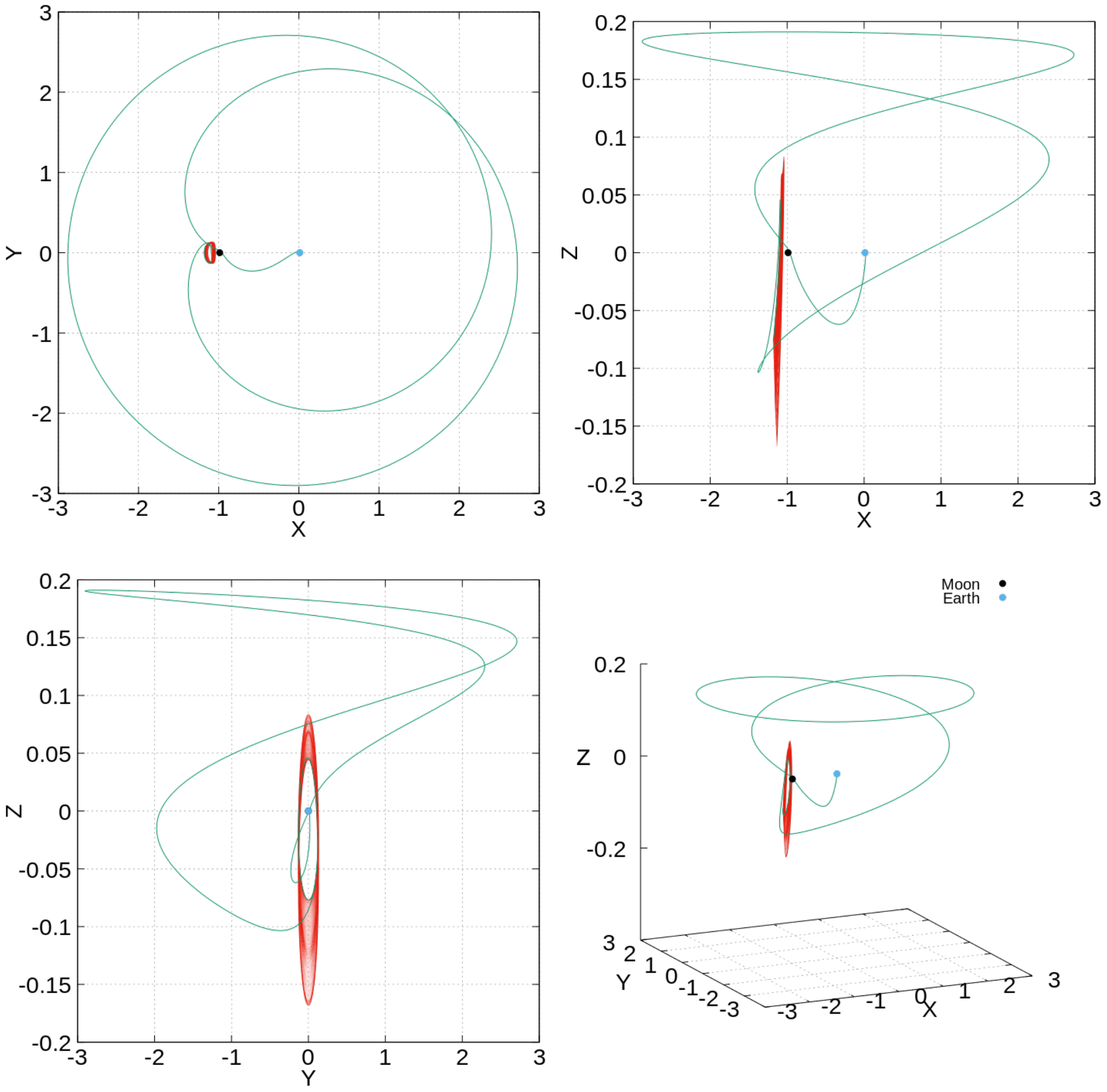

Figure 5.5: Trajectory followed by the transfer {IC13, –, J_2}

The black circle corresponds to the radius of the Moon, and blue circle to the LEO sphere (this is, the radius of the Earth plus 200km). It can be seen that for the IC13 orbit there is no Moon occultation. This is relevant because for communications purposes it is important that the Earth-Satellite line-of-sight is not blocked by the Moon.

Also, and for the sake of completeness, it is interesting to see how the different parameters computed during the analysis relate to each other. For example, from the data collected we can see how the ΔV changes as function of the total transfer time. This is captured in Figure 5.7a. It can it is observed that there is a concentration of transfers that take less than 125 days, and that there are relatively cheap transfers that take a long time. Also, it can be observed that the total maneuver cost is between 3.1617km/s (the minimum computed in this case) and slightly more than 13km/s. Another interesting plot is total ΔV as function of the latitude at which the transfer intersects with the LEO sphere. Figure 5.7b displays that information, and shows that the majority of the transfers less than 4km/s are concentrated between a latitude of -20deg and 40deg. It also shows that at low latitudes the range of ΔV is very high, as opposed to high latitudes.

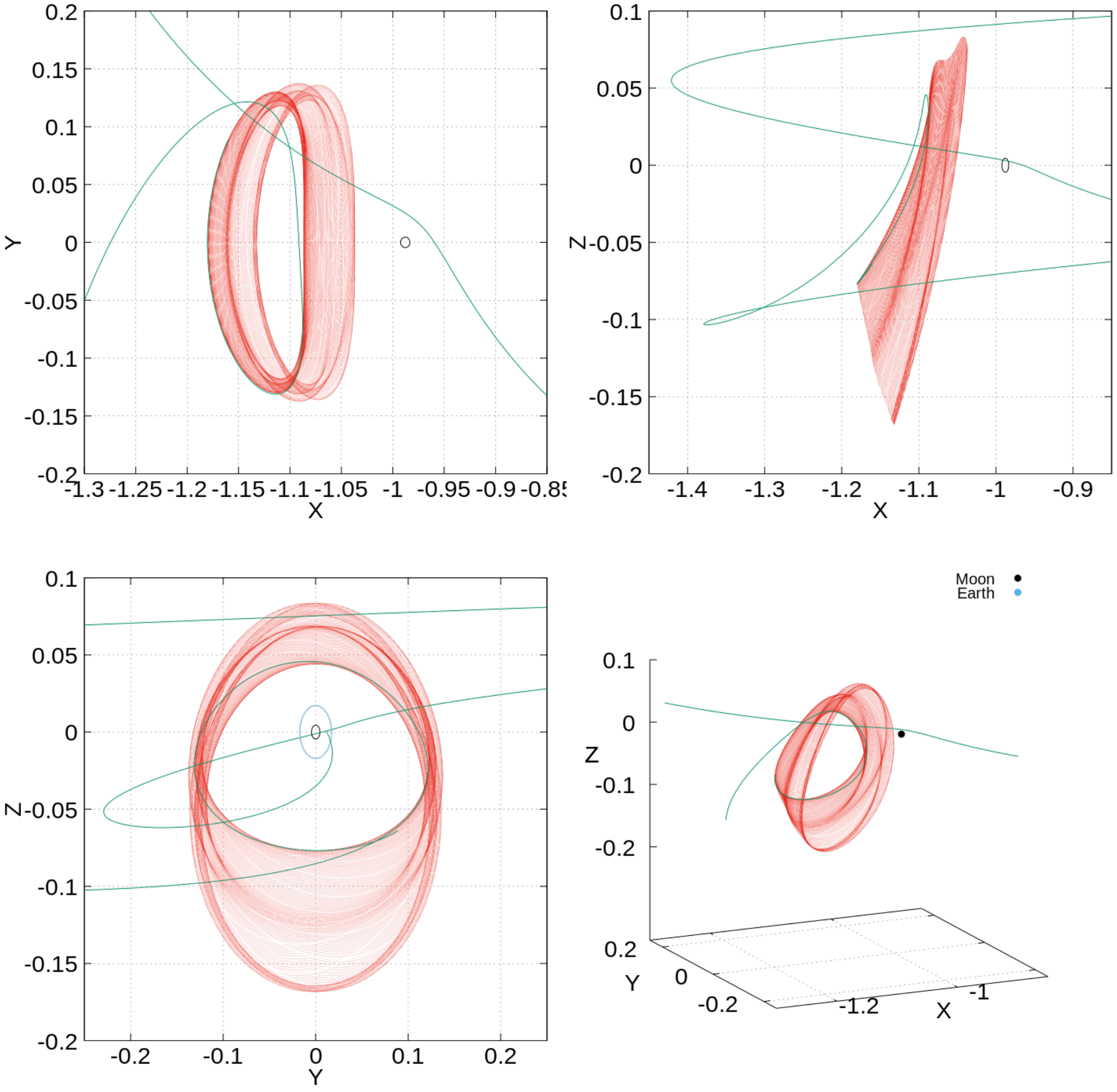

Figure 5.6: Zoom around the target orbit Trajectory followed by the transfer {IC13, −, J_2}

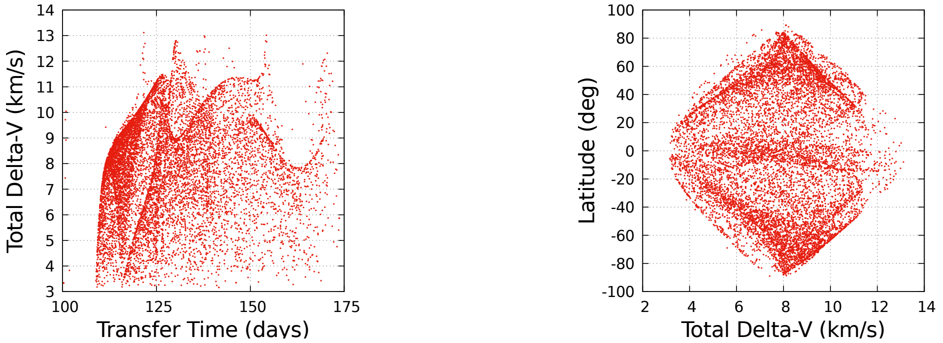

(a) (b)

Figure 5.7: Plots of transfer time against total ΔV (left) and ΔV against latitude in the LEO Sphere (right)

5.3 Case Study: transfers in the QBCP

In this section we repeat the exact same analysis described in Section 5.2 for three Halo orbits in the QBCP. Their characteristics are in Table 5.5. Note that the orbit with invariant curve ICQ1 has the same rotation number as the invariant curve IC11 used in the BCP. The unstable eigenvalues are also of the same order of magnitude. Different projections of the three invariant curves associated to the orbits used in this analysis are plotted in Figure 5.8.

Table 5.5: Characteristics QBCP Halo orbits invariant curves

Invariant Curve	rotation number	λ_u
ICQ1	`3.239814740891185`	`1269.060394604636`
ICQ2	`1.022417160604956`	`58362.76296971765`
ICQ3	`0.517157160604977`	`206452.6867125494`

The parking orbit, total integration time, conventions, and approach to compute potential transfers is exactly the same as for the BCP case described in Section 5.2. Hence, here we only present the results and the discussion.

Figure 5.9 shows the results of the analysis for the selected QBCP Halo orbits. The first row corresponds to the invariant curve ICQ1, the second to curve ICQ2, and the third one to ICQ3. The first column corresponds to the negative side of the unstable manifold, and the second one to the positive side. In the ICQ1 case the distance to the invariant curve has been chosen equal to 2.5×10^{-7} units of distance in the normalized frame (or approximately 100m in physical units), 7.5×10^{-7} (or approximately 290m in physical units) for the ICQ2 case, and 7×10^{-7} (or approximately 270m in physical units) in the ICQ3 case.

In all three cases we observe regions were direct transfers exists, although there are not prominent. It is also observed that the collisions with the Moon are mainly concentrated in

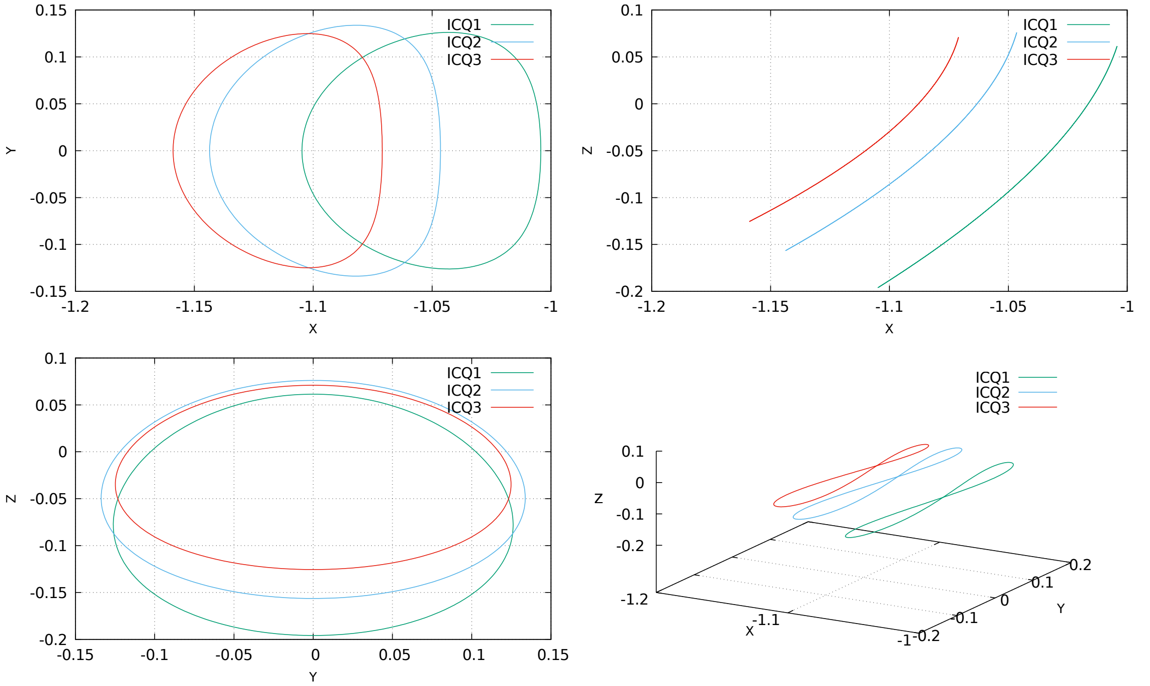

Figure 5.8: Invariant curves of the QBCP Halo orbits

the cases ICQ2 and ICQ3, positive sides (these are the sides between the Halo orbit and the Moon). On the other hand, and also for the cases ICQ2 and ICQ3, the negative sides show that a significant number of trajectories leave the influence of the Earth-Moon gravity.

Looking at specific transfers that minimize the cost functions $J_i, i = 1, 2, 3$ defined in Section 5.2, we see that the total costs in terms of ΔV and transfer time are consistent with the results described in the BCP case. These results are captured in Table 5.6. We see that the cheapest transfer in terms of total ΔV is the case $\{$ICQ2, –, $J_1\}$ with a cost of 3.1517km/s. This case, however, spends a total of approximately 125.4days to complete. In terms of total travel time, the shortest transfer is the case $\{$ICQ3, –, $J_2\}$, with a total of approximately 104 days. In this case, the ΔV is approximately 3.3km/s, which is comparable to the cheapest transfer. It is worth noting that there are other interesting trade-offs between total ΔV and travel time, like $\{$ICQ2, –, $J_3\}$.

Figure 5.10 shows the trajectory followed by the transfer $\{$ICQ3, –, $J_2\}$. Like Figure 5.5, this trajectory corresponds to the stable manifold of the target orbit ICQ3; this is, is the trajectory that a spacecraft would follow from the Earth to the target orbit. The trajectory is pretty different to the one plotted for the BCP use case. However, in terms of cost and travel time they are comparable. They have in common that the trajectory circles two times the Earth and the Moon before converging to the target orbit. Again, this 'bending' of the invariant manifold is due to the direct gravitational effect of the Sun. Finally, Figure 5.11 shows different projections of the transference around the target orbit. Again, the black

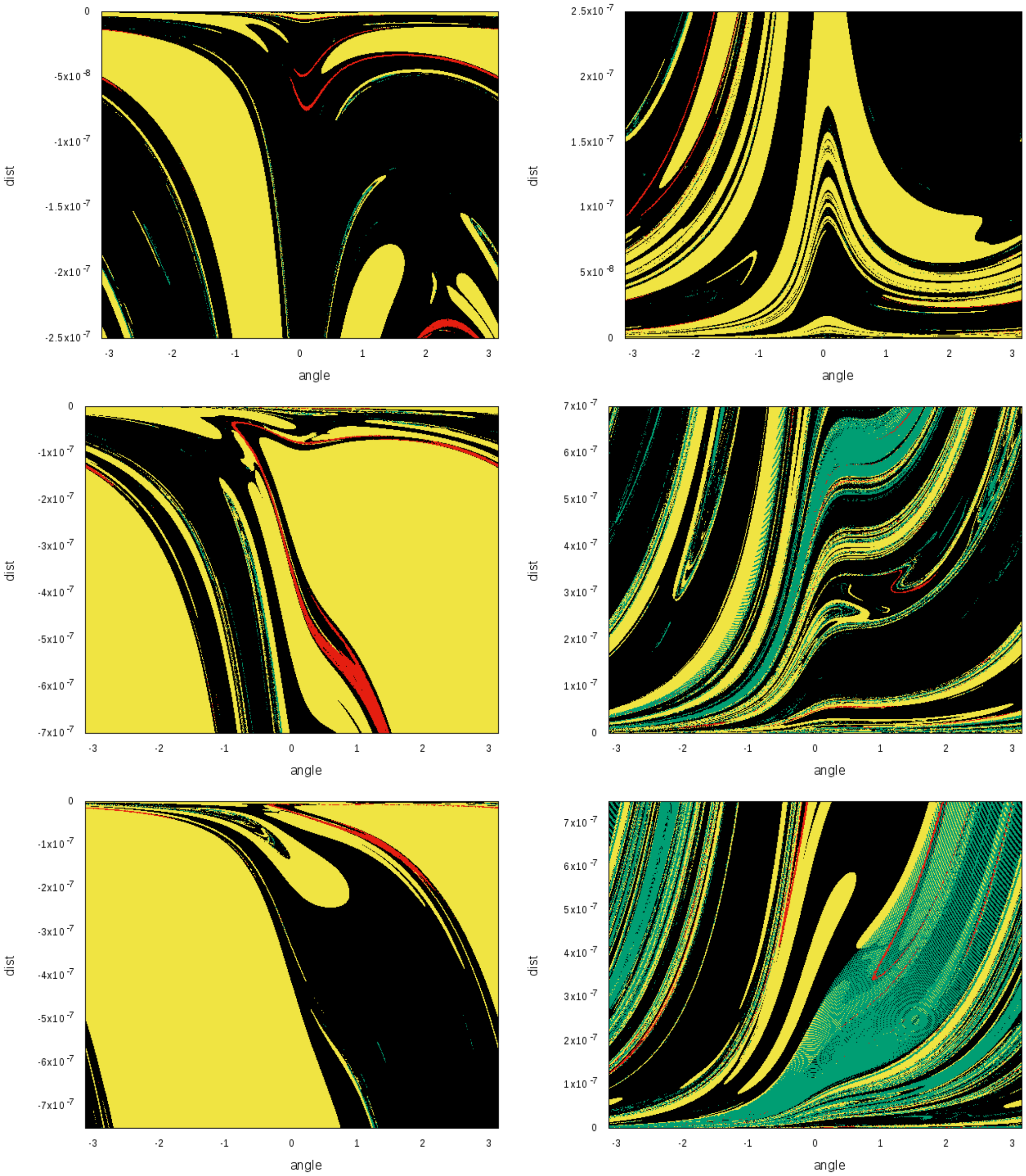

Figure 5.9: Fundamental cylinders for QBCP orbits. Valid transfers are colored in red, trajectories where a particle leaves the Earth/Moon system are colored in yellow, collisions with the Moon are green, and none of the previous cases in black. See text for details.

Table 5.6: Transfer cost to QBCP Halo orbits

Invariant Curve	Manifold Side	Cost Function	ΔV (km/s)	Δt (days)	Latitude (deg)
ICQ1	+	J_1	3.2386	134.2429	10.710279
ICQ1	−	J_1	3.2003	137.4482	6.415619
ICQ1	+	J_2	3.8470	131.3539	-18.440223
ICQ1	−	J_2	3.3394	118.9735	-2.317154
ICQ1	+	J_3	3.8470	131.3539	-18.440223
ICQ1	−	J_3	3.3394	118.9735	-2.317154
ICQ2	+	J_1	3.2271	159.5806	18.505784
ICQ2	−	J_1	3.1517	125.3764	-13.777695
ICQ2	+	J_2	6.3825	121.0911	-54.610093
ICQ2	−	J_2	3.2460	107.9764	-4.959981
ICQ2	+	J_3	3.7862	121.6507	-21.937209
ICQ2	−	J_3	3.2460	107.9764	-4.959981
ICQ3	+	J_1	3.1581	127.7909	-5.262186
ICQ3	−	J_1	3.1587	132.4915	5.678865
ICQ3	+	J_2	3.7272	115.9231	-19.960734
ICQ3	−	J_2	3.2713	104.0634	-6.622813
ICQ3	+	J_3	3.7272	115.9231	-19.960734
ICQ3	−	J_3	3.1586	132.4914	5.678865

circle corresponds to the radius of the Moon, and blue circle to the LEO sphere. It can be seen that for the ICQ3 orbit there is no Moon occultation.

Finally, it is worth looking at how the total transfer time changes with the ΔV, and how the ΔV changes as a function of the latitude of the intersection with the LEO sphere. These are shown in Figure 5.12a and Figure 5.12b respectively.

It can be observed in Figure 5.12a that the total maneuver cost is between 3.1517km/s (the minimum computed in this case) and slightly more than 13km/s. The total ΔV as function of the latitude LEO sphere latitude is in Figure 5.7b. The same qualitatively behavior as for the BCP case analyzed is seen here, where the majority of the transfers less than 4km/s are concentrated between a latitude of -20deg and 40deg. Overall, the behavior of the cases studied in the QBCP are pretty similar to their counterparts in the BCP (cases IC11, IC12, and IC13).

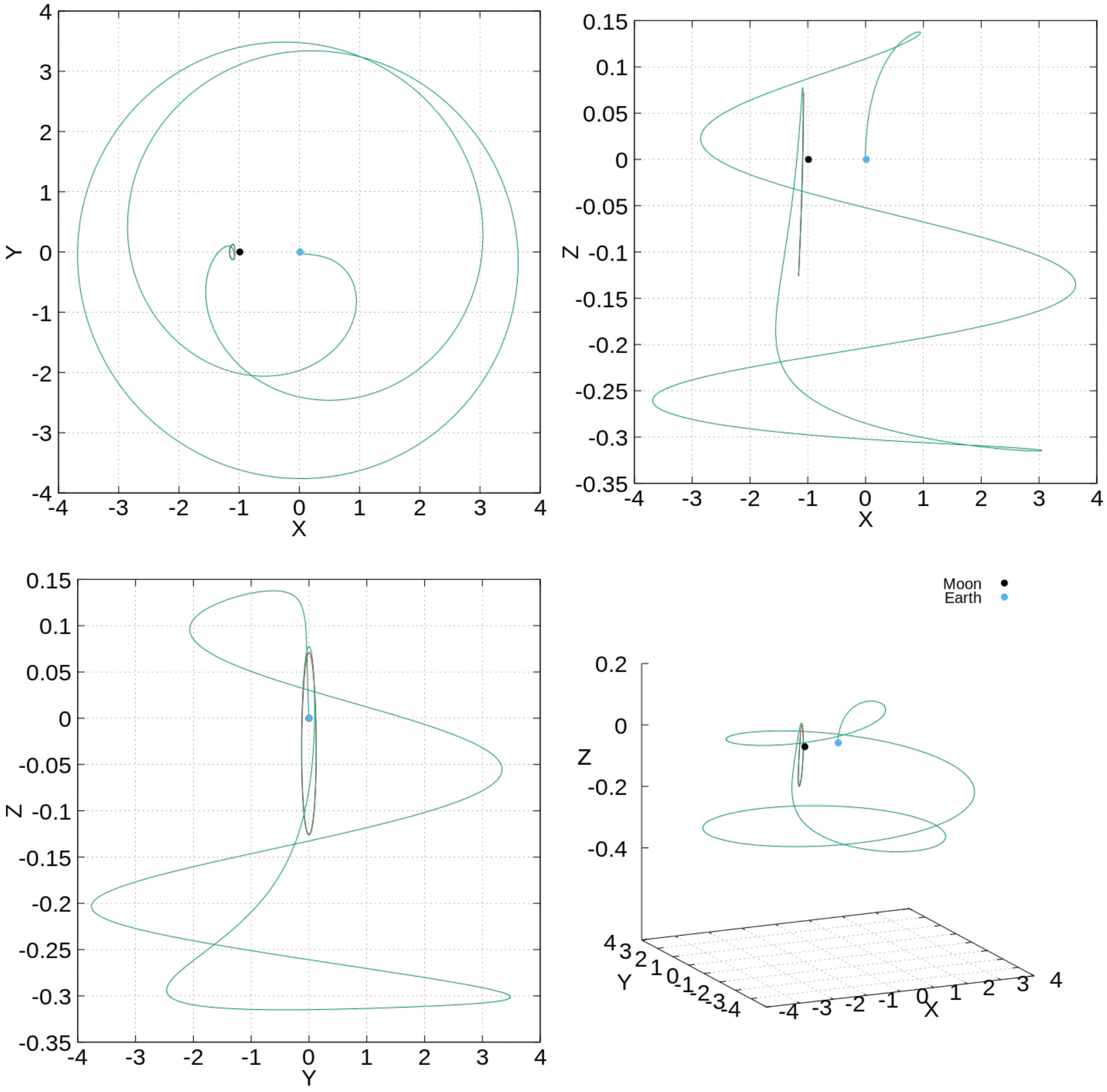

Figure 5.10: Trajectory followed by the transfer $\{\text{ICQ3}, -, J_2\}$

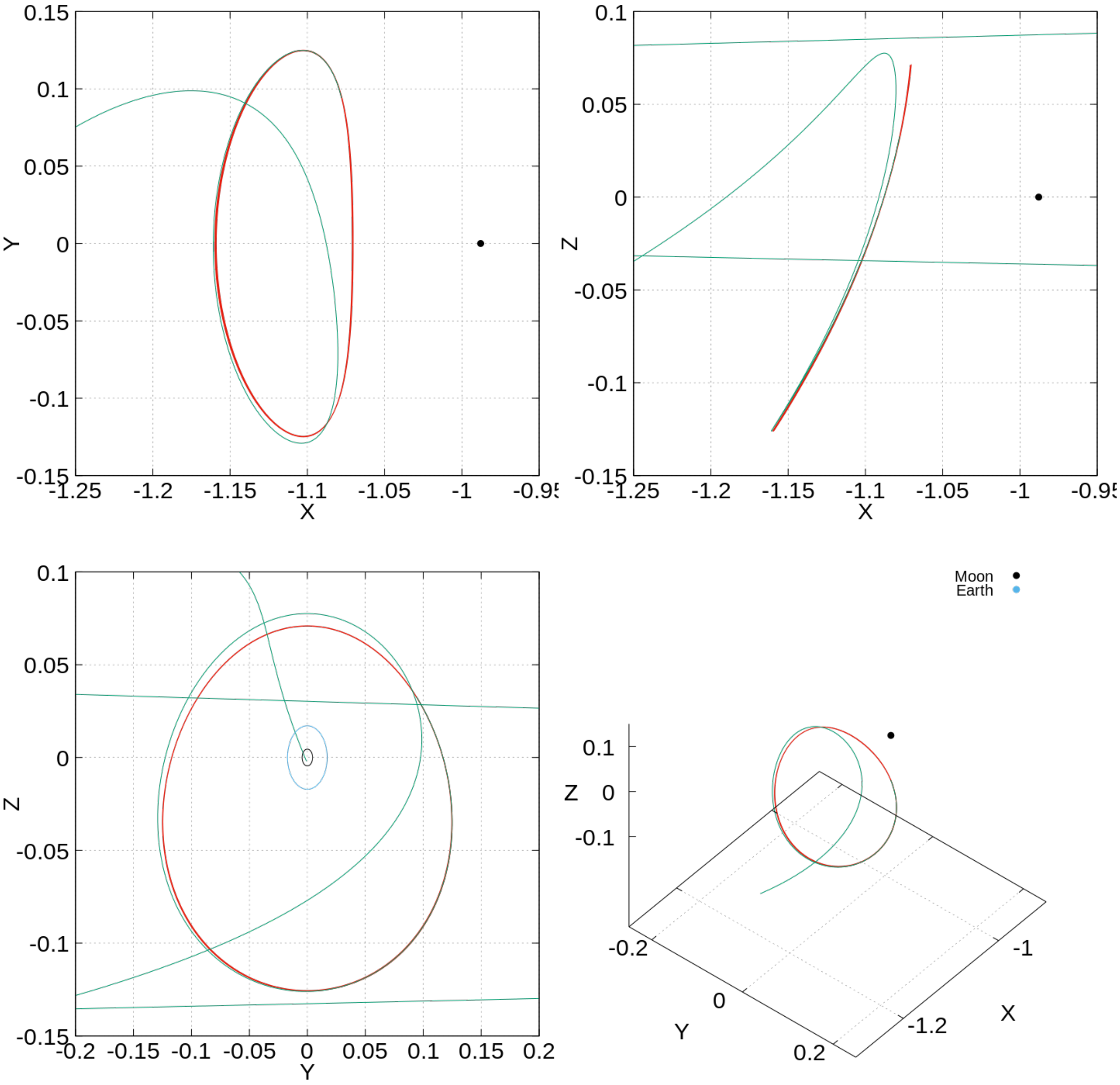

Figure 5.11: Zoom around the target orbit showing the trajectory followed by the transfer $\{\text{ICQ3}, -, J_2\}$

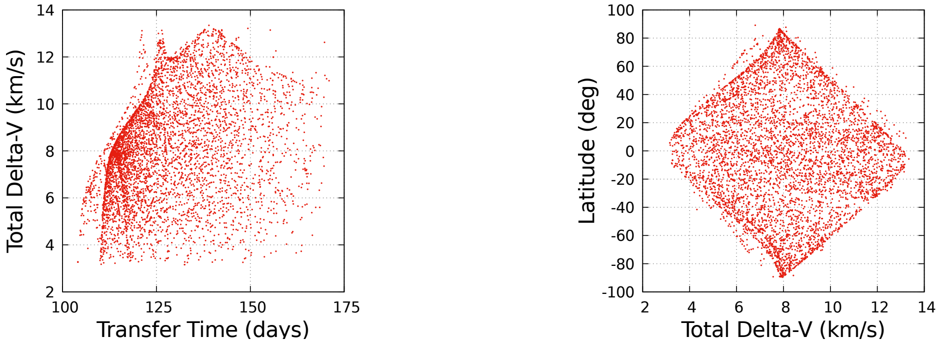

(a) (b)

Figure 5.12: Plots of transfer time against total ΔV (left) and ΔV against latitude in the LEO Sphere (right)

Chapter 6

Conclusions and further work

In this thesis we explored some aspects of the dynamics around the Earth-Moon L_1 and L_2 points in the context of two Restricted Four Body Problems: the BCP and the QBCP. Both the BCP and QBCP model the dynamics of a massless particle moving under the influence of the Sun, Earth, and Moon. Although these two models focus on the same system, it is relevant to study both because their behavior around the L_2 is qualitatively different.

These two models can be written in the Hamiltonian formalism as periodic time-dependent perturbations of the RTBP. To study these Hamiltonians, we used numerical tools tailored to these type of models to get an insight on the phase space. These two techniques are the reduction to the center manifold, and the computation and continuation of 2D tori.

For the BCP, the analysis focused around the L_2 point. The results obtained showed that the reduction to the center manifold, and the non-autonomous normal form computed in this thesis do not provide useful information about the neutral motion around L_2. The approach taken was to compute families of 2D tori, and explore any connections and their stability. As a summary of this effort we identified a total of six families of 2D tori: two Lyapunov-type planar quasi-periodic orbits, and four vertical. One of the vertical families was obtained by direct continuation of Halo orbits from the RTBP. This showed that the family of Halo orbits from the RTBP survive in the BCP, with the understanding that this new family is Cantorian. It was also shown that one of the other vertical families is Halo-like. Hence, members of this family may be potential candidates for future space missions. However, these tori are hyperbolic, as opposed the ones coming directly from the RTBP Halo obits, which are partially elliptic. It was also shown that this family of Halo-like tori comes from a family of quasi-periodic orbits in the RTBP that are resonant with the frequency of the Sun. Hence, these family of Halo-like orbits in the BCP have their counterparts in the RTBP.

For the QBCP, the focus of the analyses was there Earth-Moon L_1 and L_2 points. In this model, the reduction to the center manifold provided relevant qualitative information about the dynamics around L_1 and L_2. The main takeaway was that L_1 and L_2 had a similar qualitative behavior. In both cases there were two families of quasi-periodic Lyapunov orbits, one planar and one vertical. It was also shown that the quasi-periodic planar Lyapunov family underwent a (quasi-periodic) pitchfork bifurcation, giving rise to two families of quasi-periodic orbits with an out-of-plane component. Between them, there was a family of Lissajous quasi-periodic orbits, with three basic frequencies. Qualitatively, the phase space of the center manifold, as constructed in this thesis, resembled the phase space of the center manifold of the RTBP around L_1 and L_2.

In the QBCP we also continued families of invariant 2D tori, and for both L_1 and L_2. In these cases, the quasi-periodic planar and vertical families were continued. The bifurcations of the quasi-periodic planar Lyapunov were identified. A conclusion from this numerical experiment was that the family of out-of-plane orbits born from the bifurcation seemed not to be the RTBP Halo counterparts in the QBCP. The RTBP Halo orbits do survive in the QBCP, but do not seem to be connected to the quasi-periodic planar Lyapunov family. Another conclusion for the L_2 case is about a conjecture enunciated in [Andreu, 1998]. This conjecture stated that the family of Halo orbits in the QBCP obtained from direct continuation of the RTBP Halo orbits is connected to a to another family of 2D tori resonant with the frequency of the Sun is true. The numerical evidence seemed to indicate that this conjecture is true.

Finally, and also in the context of the BCP and the QBCP, numerical simulations to study transfers from a parking orbit around the Earth to a Halo orbit around the Earth-Moon L_2 point were studied. The main conclusion is that the invariant manifolds of the target orbits studied intersect with potential parking orbits around the Earth. The relevance of this result is that it shows that there are one-maneuver transfers from a vicinity of the Earth to Earth-Moon L_2 Halo orbits. This is not case when using the RTBP as reference model. Experiments were done for both the BCP and the QBCP, and in all cases is it was shown that the total cost in terms of ΔV and transfer time is comparable to other techniques requiring two or more maneuvers.

Although this work contributes to the understanding of the BCP and QBCP, there is a lot more to explore and learn about these models. For example, the transition from the RTBP to the BCP (resp. QBCP) is not fully understood. In this line, it would be interesting to determine if there are families objects that exist in the BCP (resp. QBCP) that don't exist in the RBTP. Also, for both the BCP and the QBCP, the connections between families of 2D tori could be explored in more detail. In this line, more families could be found to expand the existing catalog.

Focusing on applications, future research should focus on showing whether or not the objects computed in the context of the BCP and QBCP survive in a full ephemeris model. This is specially relevant in the case of invariant manifold used for transfers. If these transfers persist in a full ephemeris model, this could pave the way for efficient ways to reach Halo orbits around the Earth-Moon L_2 point.

Appendix A

Translation of a vector field

Let us assume that we have a non-autonomous differential equation defined as follows:

$$\dot{X} = F(X, t) \tag{A.1}$$

where $X = X(t), X \in \mathbb{R}^n$, $t \in \mathbb{R}$ such that F is T-periodic in t; this is, $F\big(X(t), t\big) = F\big(X(t), t+T\big)$ for certain $T > 0$. Let's also assume that there exists a solution $\phi(t)$ of the Equation (A.1) that is T-periodic; this is, $\dot{\phi}(t) = F(\phi(t), t)$ and $\phi(t) = \phi(t+T)$. The goal is to apply an explicit time-dependent change of coordinates to Equation (A.1) such that in the new variables the periodic orbit becomes an equilibrium point centered at the origin. Following this change of variables, we will derive a Hamiltonian that does not have linear terms.

Let us define the change $X = \lambda(x, t) = x + \phi(t)$, where $x = x(t)$ is the new variable. Note that this is a time-dependent change and periodic in t with period T; this is, $\lambda(x, t) = \lambda(x, t+T)$. Applying this change of variables to the Equation (A.1), we obtain that:

$$\begin{aligned}
\dot{X} = \dot{x} + \dot{\phi}(t) &= F(x + \phi(t), t); \\
\dot{x} + F(\phi(t), t) &= F(x + \phi(t), t); \\
\dot{x} &= F(x + \phi(t), t) - F(\phi(t), t); \\
\dot{x} &= F\big(\lambda(x, t), t\big) - F\big(\lambda(0, t), t\big)
\end{aligned}$$

We define $f(x, t) := F\big(\lambda(x, t), t\big) - F\big(\lambda(0, t), t\big)$. Note that for $x = 0$ we have:

$$f(0, t) = F\big(\lambda(0, t), t\big) - F\big(\lambda(0, t), t\big) = 0$$

Hence, after applying the change, the origin becomes an equilibrium point. Note that the resulting system is also non-autonomous and T-periodic in t; this is, $f(x, t) = f(x, t+T)$.

Appendix B

Expansion of the BCP Hamiltonian

This section details the expansion of the BCP Hamiltonian from its original form in Equation (1.4) to an expanded Hamiltonian of the form

$$H(\theta, x, y) = \sum_{k \geq 2} H_k(\theta, x, y) \tag{B.1}$$

where H_k are homogeneous polynomials of degree $k \geq 2$. The details in this section are for the BCP equations, but the same principles apply to the QBCP model.

The starting point is the vector field associated to the Hamiltonian (1.4) and explicitly written in Equation (1.3). Let $g_1(\theta)$, $g_2(\theta)$, $g_3(\theta)$, and $g_4(\theta)$, with $\theta = \omega_s t$, be a periodic orbit around $L_i, i \in \{1, ..., 5\}$ representing respectively the coordinates X, Y, $\dot{X}$ and $\dot{Y}$ (note that these orbits lie in the plane $Z = 0$.)

The following change of coordinates is applied to the Equation (1.3):

$$\begin{array}{rcl} X & = & -\gamma x + g_1(\theta) \\ Y & = & -\gamma y + g_2(\theta) \\ Z & = & \gamma z \end{array}$$

where $\gamma > 0$ is a scale factor.

Note that the change of coordinates defined above is not symplectic. This is, it cannot be applied directly to the Hamiltonian (1.4). Instead, the change is applied directly to the Equation (1.3) associated to the BCP, and then the new Hamiltonian is constructed by defining the generalized momenta $p_x = \dot{x} - y$, $p_y = \dot{y} + x$ and $p_z = \dot{z}$.

Let us define the following variables, where the subscript S stands for “Sun”, E for “Earth”, M for “Moon”, and P for “Particle”:

$$
\begin{aligned}
c_E(\theta) &= \frac{g_1(\theta)-\mu}{\gamma} \\
c_M(\theta) &= \frac{g_1(\theta)-\mu+1}{\gamma} \\
c_S(\theta) &= \frac{g_1(\theta)-a_s\cos(\theta)}{\gamma} \\
d_E(\theta) &= \frac{g_2(\theta)}{\gamma} \\
d_M(\theta) &= \frac{g_2(\theta)}{\gamma} \\
d_S(\theta) &= \frac{g_2(\theta)+a_s\sin(\theta)}{\gamma} \\
r_{PF}^2(\theta) &= \gamma^2\Big[\big(x-c_F(\theta)\big)^2+\big(y-d_F(\theta)\big)^2+z^2\Big],\ F=E,M,S \\
\rho^2 &= x^2+y^2+z^2 \\
k_F(\theta) &= \frac{1}{\sqrt{c_F^2(\theta)+d_F^2(\theta)}}, \quad F=E,M,S,
\end{aligned}
$$

By applying the abovementioned change of variables, the Equation (1.3) becomes:

$$
\begin{cases}
\ddot{x} = 2\dot{y}+x-\dfrac{1-\mu}{r_{PE}^3}\big(x-c_E(\theta)\big)-\dfrac{\mu}{r_{PM}^3}\big(x-c_M(\theta)\big)-\dfrac{m_S}{r_{PS}^3}\big(x-c_S(\theta)\big) \\
\qquad -\dfrac{1}{\gamma^3}\big((1-\mu)k_E^3(\theta)c_E(\theta)+\mu k_M^3(\theta)c_M(\theta)+m_S k_S^3(\theta)c_S(\theta)\big) \\
\ddot{y} = -2\dot{x}+y-\dfrac{1-\mu}{r_{PE}^3}\big(y-d_E(\theta)\big)-\dfrac{\mu}{r_{PM}^3}\big(y-d_M(\theta)\big)-\dfrac{m_S}{r_{PS}^3}\big(y-d_S(\theta)\big) \\
\qquad -\dfrac{1}{\gamma^3}\big((1-\mu)k_E^3(\theta)d_E(\theta)+\mu k_M^3(\theta)d_M(\theta)+m_S k_S^3(\theta)d_S(\theta)\big) \\
\ddot{z} = -\dfrac{1-\mu}{r_{PE}^3}z-\dfrac{\mu}{r_{PM}^3}z-\dfrac{m_S}{r_{PS}^3}z
\end{cases}
\tag{B.2}
$$

Note that as per the discussion in Appendix A, the origin is an equilibrium point.

Now, we will make use of the Legendre polynominals to express the potentials of the Sun, Earth, and Moon that appear in the Hamiltonians of the BCP as series of homogeneous polynomials (see Section 1.2.1). The following equality holds (see [Gómez et al., 1993a]):

$$\frac{\alpha_F}{\sqrt{(x-c_F(\theta))^2+(y-d_F(\theta))^2+z^2}}=\sum_{n=0}^{\infty}G_n^F,\ F=E,M,S$$

where

$$\begin{aligned}\alpha_E &= \mu-1,\\ \alpha_M &= -\mu,\\ \alpha_S &= -m_s,\end{aligned}$$

and G_n^F are homogeneous polynomials of degree n that can be obtained recursively using the following formula:

$$G_{n+1}^F(x,y,z,\theta)=k_F^2\left(\frac{2n+1}{n+1}\big(c_F(\theta)x+d_F(\theta)y\big)G_n^F-\frac{n}{n+1}\rho^2G_{n-1}^F\right)$$

with $G_0^F=\dfrac{\alpha_F}{\gamma^3}k_F$ and $G_1^F=\alpha_F\left(\dfrac{k_F}{\gamma}\right)^3\big(c_F(\theta)x+d_F(\theta)y\big)$.

With the expressions above, and noting that:

$$\frac{\partial}{\partial x}\left(\frac{\alpha_F}{r_{PF}}\right)=\alpha_F\frac{\partial}{\partial x}r_{PF}^{-1}=-\alpha_F\big(x-c_F(\theta)\big)r_{PF}^{-3}=\frac{\partial}{\partial x}\sum_{n=0}^{\infty}G_n^F,\ F=E,M,S$$

(similar expressions hold for y and z) Equation (B.2) can be written as follows:

$$\left\{\begin{array}{lcl}\ddot{x} &=& 2\dot{y}+x-\dfrac{\partial}{\partial x}\left[\sum\limits_{n=0}^{\infty}(G_n^E+G_n^M+G_n^S)\right]-\dfrac{1}{\gamma^3}\sum\limits_{F=E,M,S}\alpha_F k_F^3(\theta)c_F(\theta)\\ \ddot{y} &=& -2\dot{x}+y-\dfrac{\partial}{\partial y}\left[\sum\limits_{n=0}^{\infty}(G_n^E+G_n^M+G_n^S)\right]-\dfrac{1}{\gamma^3}\sum\limits_{F=E,M,S}\alpha_F k_F^3(\theta)d_F(\theta)\\ \ddot{z} &=& -\dfrac{\partial}{\partial z}\left[\sum\limits_{n=0}^{\infty}(G_n^E+G_n^M+G_n^S)\right]\end{array}\right. \tag{B.3}$$

Note that values for $n=0$ can be ignored, as they are equal to zero when derived. Also, the terms resulting from deriving the terms for $n=1$ cancel all the terms that only depend on θ in the above equation (otherwise, the origin would not be an equilibrium point!). Hence, only terms for $n\geq 2$ are relevant in the equations. Hence, equation (B.3) can be written as follows:

$$\begin{cases} \ddot{x} & = & 2\dot{y} + x - \dfrac{\partial}{\partial x}\left[\sum\limits_{n=2}^{\infty}(G_n^E + G_n^M + G_n^S)\right] \\ \ddot{y} & = & -2\dot{x} + y - \dfrac{\partial}{\partial y}\left[\sum\limits_{n=2}^{\infty}(G_n^E + G_n^M + G_n^S)\right] \\ \ddot{z} & = & -\dfrac{\partial}{\partial z}\left[\sum\limits_{n=2}^{\infty}(G_n^E + G_n^M + G_n^S)\right] \end{cases} \tag{B.4}$$

The system of equations in Equation (B.4) can be expressed in Hamiltonian form by defining the momenta $p_x = \dot{x} - y$, $p_y = \dot{y} + x$ and $p_z = \dot{z}$. The corresponding Hamiltonian is given by:

$$H = \frac{1}{2}\left(p_x^2 + p_y^2 + p_z^2\right) + yp_x - xp_y + \sum_{n\geq 2}(G_n^E + G_n^M + G_n^S) \tag{B.5}$$

With this, we have a Hamiltonian of the form of Equation B.1.

Appendix C

Floquet transformation input file sample

The following is a sample of the input file to compute the floquet transformation for the BCP around L_1. This file is very simple, and contains details on the BCP model, the number of sections, and initials condition of the periodic orbit that substitutes the L_1 point in the BCP. In this case, we have used four sections. The numbers indented more to the left are the epochs, and the other six the positions and the conjugated momentums.

```
// d_mu  : Mass parameter for the Earth/Moon system
// d_as  : Sun semi-major axis
// d_ms  : Mass of the Sun
// d_ns  : Mean motion of the Sun
// d_ws  : Mean angular velocity of the Sun
// d_eps : Scale factor applied to the Mass of the Sun
//         (d_eps = 0 is the CRTBP; d_eps = 1 is the BCP).
//         Internally, the SW will do d_ms = d_eps*d_ms

d_mu    =       0.0121505816234336
d_as    =     388.8111430233511214
d_ms    =  328900.5499999991152436
d_ns    =       0.0748040144817104
d_ws    =       0.9251959855182896
d_eps   =       1.0000000000000000

periodic_orbit:
4
0.0000000000000000
    -0.8376063136660812
     0.0000000000000000
```

```
     0.0000000000000000
    -0.0000000000000002
    -0.8276221024215736
     0.0000000000000000
1.6977984679807545
    -0.8358524267563349
    -0.0000141702846437
     0.0000000000000000
     0.0000015989133886
    -0.8457722920148192
     0.0000000000000000
3.3955969359615090
    -0.8375954084856564
     0.0000000000000002
     0.0000000000000000
    -0.0000000000000004
    -0.8276783893939365
     0.0000000000000000
5.0933954039422638
    -0.8358524267563350
     0.0000141702846436
     0.0000000000000000
    -0.0000015989133886
    -0.8457722920148195
     0.0000000000000000
6.7911938719230180
```

Appendix D

Reduction to the center manifold input file sample

The following is a sample of the input file read by the software that computes the reduction to the center manifold around L_1 in the BCP. It contains information about the model, the degree on the expansion and the scale factor, the normal frequencies used, the periodic orbit around which the center manifold is computed used to translate the vector so the origin is an equilibrium point, and the Floquet transformation. This example used 12 Fourier nodes, but this particular case 32 were used to generate good results. Also, note that values of the periodic orbit and the FLoquet transformation were removed and substituted by "`[...]`" to make the file fit in the page.

```
// Local execution time: Sun Apr 12 08:27:58 2020
// INFO: The error in the periodic orbit is approx. 3.7388e-14.

// Parameters that characterize the reduction to the center manifold
//  i_n     : Order of the expansion
//  d_gamma : Scale factor of the variable change
i_n     = 6
d_gamma = 0.1509342729900642

// d_mu  : Mass parameter for the Earth/Moon system
// d_as  : Sun semi-major axis
// d_ms  : Mass of the Sun
// d_ns  : Mean motion of the Sun
// d_ws  : Mean angular velocity of the Sun
// d_eps : Scale factor applied to the Mass of the Sun (d_eps = 0
//         is the CRTBP; d_eps = 1 is the BCP). Internally, the SW
//         will do d_ms = d_eps*d_ms
```

```
d_mu      =      0.0121505816234336
d_as      =    388.8111430233511214
d_ms      = 328900.5499999991152436
d_ns      =      0.0748040144817104
d_ws      =      0.9251959855182896
d_eps     =      1.0000000000000000

// Number of orbit points
number_of_points = 12


// Jordan form of the logarithm of the monodromy matrix:
//
//   |  w1* |  w2* |
//   | ----------- | [1]
//   | -w2* | -w1* |
//
//
// where:
//
//       | d_wi1   0     0   |
// wi* = |   0   d_wi2   0   |
//       |   0     0   d_wi3 |
// i = 1, 2
//
// This is to make it generic. If d_w1j<>0 ==> d_w2j = 0 (and vice versa)
// for j = 1, 2, 3.
// Where these values fall in matrix [1] determine whether they are real
// or imaginary.
// If a value is in the diagonal blocks of [1] (this is, w1*), then it is
// real. If it is in the off-diagonal blocks (this is, w2*), then it is imaginary.

d_w11 =    2.9267841518284921
d_w12 =    0.0000000000000000
d_w13 =    0.0000000000000000

d_w21 =    0.0000000000000000
d_w22 =    2.3298196360328820
d_w23 =    2.2669514915847815

// The next rows are the periodic orbit. Each row has to the interpreted as follows:
//  - The first number is an integer used for numbering purposes.
```

```
//  - The second number is the time associated to the periodic orbit. (Note that
//     the entry corresponding to the period t = 2*pi/d_ws is not printed.)
//  - The rest are the state vector as follows: x, y, px, py. (Note that z, and
//     pz are not stored because the perturbation is planar; hence, z = pz = 0.)
periodic_orbit:
0    0.0000000000000000  -0.8376063136660812   0.0000000000000000  [...]
1    0.5659328226602515  -0.8371908948072349   0.0046646879885251  [...]
2    1.1318656453205029  -0.8363113736831645   0.0046442877612088  [...]
3    1.6977984679807545  -0.8358524267563349  -0.0000141702846437  [...]
4    2.2637312906410059  -0.8363199983120418  -0.0046471059536492  [...]
5    2.8296641133012574  -0.8371893358118813  -0.0046410815644076  [...]
6    3.3955969359615090  -0.8375954084856564   0.0000000000000002  [...]
7    3.9615297586217602  -0.8371893358118817   0.0046410815644073  [...]
8    4.5274625812820117  -0.8363199983120423   0.0046471059536493  [...]
9    5.0933954039422638  -0.8358524267563350   0.0000141702846436  [...]
10   5.6593282266025149  -0.8363113736831623  -0.0046442877612078  [...]
11   6.2252610492627660  -0.8371908948072356  -0.0046646879885245  [...]

// The next rows are the Floquet_transformation. Each row has to the interpreted as
// follows:
//  - The first number is an integer used for numbering purposes.
//  - The second number is the time associated to the Floquet transformation.
//    (Note that the entry corresponding to the period t = 2*pi/d_ws is not
//    printed.)
//  - The rest is the 6x6 matrix transformation stored by rows (i.e., each group of
//    6 is a row of the Floquet transformation matrix.
Floquet_transformation:
0    0.0000000000000000  -0.3927384610198936  -0.2051367824594226  [...]
1    0.5659328226602515  -0.3956959312339151  -0.2023669961707468  [...]
2    1.1318656453205029  -0.3962820434898379  -0.1970365751487209  [...]
3    1.6977984679807545  -0.3944159776689416  -0.1944746023449725  [...]
4    2.2637312906410059  -0.3918613172535262  -0.1970550900655813  [...]
5    2.8296641133012574  -0.3907851593241050  -0.2023877766361938  [...]
6    3.3955969359615090  -0.3927454700728688  -0.2050932247984402  [...]
7    3.9615297586217602  -0.3956761198123422  -0.2023877766360033  [...]
8    4.5274625812820117  -0.3962717888781767  -0.1970550900657005  [...]
9    5.0933954039422638  -0.3944239538060244  -0.1944746023450021  [...]
10   5.6593282266025149  -0.3918612063879846  -0.1970365751487207  [...]
11   6.2252610492627660  -0.3907646355613166  -0.2023669961707460  [...]
```

Bibliography

[Alessi, 2010] Alessi, E. M. (2010). *The Role and Usage of Libration Point Orbits in the Earth-Moon System.* PhD thesis, Univ. de Barcelona.

[Andreu, 1998] Andreu, M. A. (1998). *The Quasi-Bicircular Problem.* PhD thesis, Univ. Barcelona.

[Andreu, 2002] Andreu, M. A. (2002). Dynamics in the center manifold around L_2 in the Quasi-Bicircular Problem. *Celestial Mech.*, 84(2):105–133.

[Arrowsmith and Place, 1990] Arrowsmith, R. and Place, C. (1990). *An Introduction to Dynamical Systems.* Cambridge University Place, New York, first edition.

[Belbruno and Miller, 1993] Belbruno, E. A. and Miller, J. K. (1993). Sun-perturbed Earth-to-moon transfers with ballistic capture. *Journal of Guidance, Control, and Dynamics*, 16(4):770–775.

[Bernelli Zazzera et al., 2004] Bernelli Zazzera, F., Topputo, F., and Massari, M. (2004). Assessment of mission design including utilisation of libration points and weak stability boundaries (03-4103b). Technical report, European Space Agency.

[Carr, 1981] Carr, J. (1981). *Applications of centre manifold theory.* Applied mathematical sciences. Springer-Verlag, New York. Based on a series of lectures given in the Lefschetz Center for Dynamical Systems in the Division of Applied Mathematics at Brown University during the academic year 1978-79–Pref.

[Castellà, 2003] Castellà, E. (2003). *Sobre la dinàmica prop dels punts de Lagrange del sistema Terra-Lluna.* PhD thesis, Univ. Barcelona.

[Castellà and Jorba, 2000] Castellà, E. and Jorba, À. (2000). On the vertical families of two-dimensional tori near the triangular points of the bicircular problem. *Celestial Mech.*, 76(1):35–54.

[Cronin et al., 1964] Cronin, J., Richards, P., and Russell, L. (1964). Some periodic solutions of a four-body problem. *Icarus*, 3:423–428.

[Duarte, 2020] Duarte, G. (2020). *On the dynamics around the collinear points in the Sun-Jupiter system.* PhD thesis, Univ. Barcelona.

[Farrés and Jorba, 2010] Farrés, A. and Jorba, À. (2010). On the high order approximation of the centre manifold for ODEs. *Discrete and Continuous Dynamical Systems - Series B*, 14(3):977–1000.

[Gabern, 2003] Gabern, F. (2003). *On the dynamics of the Trojan asteroids.* PhD thesis, Univ. de Barcelona.

[García and Gómez, 2007] García, F. and Gómez, G. (2007). A note on weak stability boundaries. *Celestial Mechanics and Dynamical Astronomy*, 97:87–100.

[Giorgilli et al., 1989] Giorgilli, A., Delshams, A., Fontich, E., Galgani, L., and Simó, C. (1989). Effective stability for a Hamiltonian system near an elliptic equilibrium point, with an application to the restricted three body problem. *J. Differential Equations*, 77:167–198.

[Gómez et al., 1993a] Gómez, G., Jorba, À., Masdemont, J., and Simó, C. (1993a). Study of Poincaré maps for orbits near Lagrangian points. ESOC contract 9711/91/D/IM(SC), final report, European Space Agency. Reprinted as *Dynamics and mission design near libration points. Vol. IV, Advanced methods for triangular points*, volume 5 of World Scientific Monograph Series in Mathematics, 2001.

[Gómez et al., 1993b] Gómez, G., Jorba, À., Masdemont, J., and Simó, C. (1993b). Study of Poincaré maps for orbits near Lagrangian points. ESOC contract 9711/91/D/IM(SC), final report, European Space Agency.

[Gómez et al., 1985] Gómez, G., Llibre, J., Martínez, R., and Simó, C. (1985). Station keeping of libration point orbits. ESOC contract 5648/83/D/JS(SC), final report, European Space Agency. Reprinted as *Dynamics and mission design near libration points. Vol. I, Fundamentals: the case of collinear libration points*, volume 2 of World Scientific Monograph Series in Mathematics, 2001.

[Gómez et al., 1987] Gómez, G., Llibre, J., Martínez, R., and Simó, C. (1987). Study on orbits near the triangular libration points in the perturbed Restricted Three–Body Problem. ESOC contract 6139/84/D/JS(SC), final report, European Space Agency. Reprinted as *Dynamics and mission design near libration points. Vol. II, Fundamentals: the case of triangular libration points*, volume 3 of World Scientific Monograph Series in Mathematics, 2001.

[Gómez et al., 2003] Gómez, G., Masdemont, J. J., and Mondelo, J. M. (2003). Libration point orbits: A survey from the dynamical point of view. In *Libration Point Orbits and Applications: Proceedings of the Conference, Aiguablava, Spain, 10-14 June 2002.* World Scientific.

[Gómez and Mondelo, 2001] Gómez, G. and Mondelo, J. (2001). The dynamics around the collinear equilibrium points of the RTBP. *Phys. D*, 157(4):283–321.

[Gonzalez and Mireles James, 2016] Gonzalez, J. and Mireles James, J. (2016). High-order parameterization of stable/unstable manifolds for long periodic orbits of maps. *SIAM Journal on Applied Dynamical Systems*, 16.

[Huang, 1960] Huang, S. (1960). Very restricted four-body problem. Technical note TN D-501, Goddard Space Flight Center, NASA.

[Jorba, 1999] Jorba, À. (1999). A methodology for the numerical computation of normal forms, centre manifolds and first integrals of Hamiltonian systems. *Exp. Math.*, 8(2):155–195.

[Jorba, 2001] Jorba, À. (2001). Numerical computation of the normal behaviour of invariant curves of n-dimensional maps. *Nonlinearity*, 14(5):943–976.

[Jorba et al., 2020] Jorba, À., Jorba-Cuscó, M., and Rosales, J. J. (2020). The vicinity of the Earth-Moon L_1 point in the Bicircular Problem. *Celestial Mech.*, 132(2):11.

[Jorba and Masdemont, 1999] Jorba, À. and Masdemont, J. (1999). Dynamics in the center manifold of the collinear points of the restricted three body problem. *Physica D Nonlinear Phenomena*, 132:189–213.

[Jorba and Nicolás, 2020] Jorba, À. and Nicolás, B. (2020). Transport and invariant manifolds near L_3 in the Earth-Moon Bicircular model. *Communications in Nonlinear Science and Numerical Simulation*, 89:105327.

[Jorba and Olmedo, 2009] Jorba, À. and Olmedo, E. (2009). On the computation of reducible invariant tori on a parallel computer. *SIAM J. Appl. Dyn. Syst.*, 8(4):1382–1404.

[Jorba and Villanueva, 1997] Jorba, À. and Villanueva, J. (1997). On the persistence of lower dimensional invariant tori under quasi-periodic perturbations. *Journal of Nonlinear Science*, 7(5):427–473.

[Jorba-Cuscó, 2018] Jorba-Cuscó, M. (2018). *Periodic time dependent Hamiltonian systems and applications*. PhD thesis, Univ. Barcelona.

[Jorba-Cuscó et al., 2018] Jorba-Cuscó, M., Farrés, A., and Jorba, À. (2018). Two periodic models for the Earth-Moon system. *Frontiers in Applied Mathematics and Statistics*, 4:32.

[Jorba-Cuscó et al., 2020] Jorba-Cuscó, M., Farrés, A., and Jorba, À. (2020). On the stabilizing effect of solar radiation pressure in the Earth-Moon system. *Advances in Space Research*.

[Koon et al., 2001] Koon, W., Lo, M., Marsden, J., and Ross, S. (2001). Low energy transfer to the Moon. *Celestial Mechanics and Dynamical Astronomy*, 81.

[Le Bihan et al., 2014] Le Bihan, B., Kokou, P., Receveur, J.-B., and Lizy-Destrez, S. (2014). Computing an optimized trajectory between Earth and an EML2 halo orbit. In *AIAA Guidance, Navigation, and Control Conference*, National Harbor, MD, USA.

[Le Bihan et al., 2017a] Le Bihan, B., Masdemont, J., Gómez, G., and Lizy-Destrez, S. (2017a). Invariant manifolds of a non-autonomous quasi-bicircular problem computed via the parameterization method. *Nonlinearity*, 30:3040–3075.

[Le Bihan et al., 2017b] Le Bihan, B., Masdemont, J., Gómez, G., and Lizy-Destrez, S. (2017b). Systematic study of the dynamics about and between the libration points of the Sun-Earth-Moon system. In *International Symposium on Space Flight Dynamics (ISSFD)*, pages 1–10, Matsuyama, JP.

[Meyer et al., 2008] Meyer, K., Hall, G., and Offin, D. (2008). *Introduction to Hamiltonian dynamical systems and the N-body problem*, volume 90. Springer Science & Business Media, second edition.

[Mingtao and Zheng, 2010] Mingtao, L. and Zheng, J. (2010). Indirect transfer to the Earth-Moon L_1 libration point. *Celestial Mechanics and Dynamical Astronomy*, 108:203–213.

[Rausch, 2005] Rausch, R. R. (2005). Earth to Halo Orbit Transfer Trajectories. Master's thesis, Purdue University, Indiana.

[Scheeres, 1998] Scheeres, D. J. (1998). The restricted Hill four-body problem with applications to the Earth-Moon-Sun system. *Celestial Mech.*, 70(2):75–98.

[Seydel, 2009] Seydel, R. (2009). *Practical bifurcation and stability analysis*. Interdisciplinary Applied Mathematics (Vol 5). Springer-Verlag, New York, third edition.

[Sijbrand, 1985] Sijbrand, J. (1985). Properties of center manifolds. *Trans. Amer. Math. Soc.*, 289(2):431–469.

[Simó, 1990] Simó, C. (1990). On the analytical and numerical approximation of invariant manifolds. In Benest, D. and Froeschlé, C., editors, *Modern methods in celestial mechanics*, pages 285–330. Ed. Frontières.

[Simó et al., 1995] Simó, C., Gómez, G., Jorba, À., and Masdemont, J. (1995). The Bicircular model near the triangular libration points of the RTBP. In Roy, A. and Steves, B., editors, *From Newton to Chaos*, pages 343–370, New York. Plenum Press.

[Stoer and Bulirsch, 2002] Stoer, J. and Bulirsch, R. (2002). *Introduction to numerical analysis*, volume 12 of *Texts in Applied Mathematics*. Springer-Verlag, New York, third edition.

[Szebehely, 1967] Szebehely, V. (1967). *Theory of Orbits*. Academic Press.

[Vanderbauwhede, 1989] Vanderbauwhede, A. (1989). Centre manifolds, normal forms and elementary bifurcations. In *Dynamics reported, Vol. 2*, volume 2 of *Dynam. Report. Ser. Dynam. Systems Appl.*, pages 89–169. Wiley, Chichester.

[Zimovan et al., 2017] Zimovan, E., Howell, K., and Davis, D. (2017). Near rectilinear halo orbits and their application in cis-lunar space. In *Conference on Dynamics and Control of Space Systems*, Moscow, Russia.